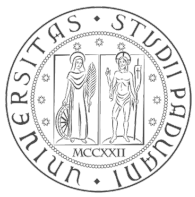

Università degli Studi di Padova

Dipartimento di Fisica e Astronomia "Galileo Galilei"

Master degree in Astronomy

Toward a population study of BL Lac objects observed with the MAGIC gamma-ray telescopes

Candidate

Giacomo Moras

Supervisor

Prof. Michele Doro

Co-supervisors

Prof. Alberto Franceschini

Dr. Andrea Tramacere

Academic Year 2017/2018

Step after step
We try controlling our fate,
When we finally start living
It has become too late
Octavarium - Dream Theater

Contents

Abstract

The main theme of this master thesis work is the high energy astrophysics, and in particular the study of the BL Lacertae objects, a type of AGNs. This study has been made with the help of the data taken from the MAGIC telescope observations made since 2006, with the scripts written by me for the analysis of this kind of sources and the `JetSet` framework. This master thesis work is mainly subdivided in two parts. In the first part we have checked all the FITS files that the MAGIC collaboration has made accessible in a publicly available online site. This work has been done with a `Python` script I have written, and our aim was to open them and to see what they contained; then we have compared their content with their corresponding paper published by MAGIC. After this work, since the most numerous extragalactic sources we had were the BL Lacertae objects, we decided to make a population study of these sources. So in the second part of the thesis we tried to make a population study of our 17 BL Lacs sources, using the spectra obtained from the MAGIC telescopes and then using also the SED models taken from the papers of our sources. In the end we used the program `JetSet` to obtain the fits of the data of the sources and to compute the position of the peak of synchrotron and of inverse Compton. With these data we have been able to make our kind of population study and to verify the physics behind these objects.

Outline

In the first chapter the main concepts needed to understand the physics of this master thesis are expressed, from the high energy astrophysics to a general overview about the MAGIC telescope.
In the second chapter our work about the check and comparison of the FITS files and their corresponding paper is described.
In the third chapter our study of the population of the BL Lacs begins, using only the data taken from the MAGIC FITS files and more information about this type of sources are given.
In the fourth chapter it is described the analysis of the SEDs of the sources with the `JetSet` program. This is the most experimental part of this thesis and it has been made with the collaboration of Dr. Andrea Tramacere from the University of Geneva.
In the last chapter there are the conclusions of my thesis work and the future outlooks.

Sommario

Il tema principale di questa tesi magistrale é l'astrofisica delle alte energie, ed in particolare lo studio degli oggetti BL Lacertae, un tipo di AGN. Questo studio é stato fatto con l'aiuto dei dati presi dalle osservazioni fatte dal telescopio MAGIC dal 2006 ad oggi, con i programmi creati per l'analisi di questo tipo di sorgenti e con il programma `JetSet`.
Questo lavoro di tesi magistrale é principalmente diviso in due parti. Nella prima é stato fatto il controllo di tutti i file FITS che la collaborazione MAGIC ha reso accessibili in un pubblico sito online. Questo lavoro é stato fatto con un codice `Python` che ho scritto, e il nostro scopo era quello di aprirli e vedere che cosa contenessero. Abbiamo poi comparato il loro contenuto con il loro articolo corrispondente pubblicato da MAGIC. Dopo questo lavoro, poiché il numero maggiore di sorgenti extragalattiche che avevamo erano sorgenti BL Lacertae, abbiamo decido di cominciare uno studio di popolazione di queste sorgenti. Cosí nella seconda parte della tesi abbiamo cominciato lo studio delle nostre 17 BL Lac, usando gli spettri ottenuti dal telescopio MAGIC, e poi usando anche i modelli di SED presi dagli articoli delle sorgenti. Infine abbiamo usato il programma `JetSet` per ottenere dei fit dei dati delle sorgenti e per calcolare la posizione dei picchi di sincrotrone e di Compton inverso. Con l'ausilio di tutti questi dati, siamo stati capaci di ottenere il nostro inizio di studio di popolazione e di verificare la fisica che sta dietro questi oggetti.

Traccia

Nel primo capitolo sono espressi i concetti fondamentali necessari per capire la fisica di questa tesi, partendo da una panoramica dell'astrofisica delle alte energie, fino ad arrivare ad una panoramica generale sul telescopio MAGIC.
Nel secondo capitolo é descritto il nostro lavoro di controllo e comparazione dei file FITS ed il loro articolo corrispondente.
Nel terzo capitolo comincia il nostro studio di popolazione delle BL Lac, usando solamente i dati presi dai file FITS, e sono approfondite maggiormente le proprietá di queste sorgenti.
Nel quarto capitolo é descritta l'analisi delle SED delle sorgenti con il programma `JetSet`. Questa é la parte piú sperimentale della tesi, ed é stata fatta in collaborazione con il dottor Andrea Tramacere dell'Universitá di Ginevra.
Nell'ultimo capitolo ci sono le conclusioni del mio lavoro di tesi e i futuri sviluppi che potranno essere raggiunti.

Chapter 1

High Energy γ-ray Astronomy

This introduction is based on [3, 15, 4, 5, 6].

1.1 Cosmic rays

Cosmic rays were first discovered by Victor Hess around 1912 during a balloon flight whose aim was understanding why a sealed electroscope was naturally discharging, and if the radiation that was causing the discharge was coming from the ground or from somewhere else. Checking the radiation level at different heights would have answered to this question. It was the first time that a particle was observed by a man-made instrument.
The discovery of cosmic rays highlighted the existence of astrophysics processes made with a non-thermal acceleration, which have both a galactic or extragalactic origin.
Cosmic rays are mainly composed of electrically charged particles and radiation, in particular:

- Protons, 90% ;
- Helium nuclei, $< 10\%$;
- Heavier nuclei, $< 1\%$;
- Electrons, $< 1\%$;
- γ-rays, $0.1 - 1\%$.

They are classified according to their energy:

1. Low energy, LE, for a range 0.1-1 MeV
2. Medium energy, ME, for a range 10-20 MeV
3. High energy, HE, for a range 20 MeV - 30 GeV
4. Very high energy, VHE, for a range 30 GeV - 30 TeV

5. Ultra high energy, UHE, for a range 30 TeV - 30 PeV

6. Extremely high energy, EHE, for a range $>$ 30 PeV.

The domain of the cosmic rays is very wide and its range extends over 13 decades of energy, from 10^9 eV to 10^{21} eV; its flux instead extends for 32 orders of magnitudes, from 10^{-28} $(\mathrm{m}^2\ \mathrm{sr\ s\ GeV})^{-1}$ to 10^4 $(\mathrm{m}^2\ \mathrm{sr\ s\ GeV})^{-1}$. The flux is described as a function of energy using a broken power law:

$$\frac{d\mathrm{F}}{d\mathrm{E}} \propto \mathrm{E}^{-\alpha} \tag{1.1}$$

where α is the spectral index depending on the energy range:

- $\alpha \simeq 2.7$ for $E \leq 10^{15.5}$ eV,
- $\alpha \simeq 3.0$ for $10^{15.5} < E < 10^{18}$ eV,
- $\alpha \simeq 2.6$ for $E \geq 10^{18}$ eV.

The two limits, points were the slope changes, are called *knee* and *ankle* respectively, and are shown in Figure 1.1 [1]. Cosmic rays with energy below the knee are supposed to have a galactic origin, while those above the ankle an extragalactic origin, because the galactic magnetic field is too weak to confine them out of the galaxy.
Since cosmic rays of high energy are generated by non-thermal processes, as it will be explained in section 1.3, they are very important in astrophysics because their study allows us to investigate these most powerful non thermal processes of the Universe accurately, the location where they are accelerated, the power they emit and their spectra. Also, γ cosmic rays are not deflected by the magnetic fields of the Universe and of the Earth, and for this reason they maintain their arrival direction information, allowing us to know where they come from.

1.2 Air showers

For energies in the range between X- and γ-rays, the Earth's atmosphere results opaque, so this radiation cannot be detected directly from the ground. However, a phenomenon occurs when a cosmic ray enters our atmosphere: it interacts with its atoms through processes that depend on the energy of the emitted cosmic ray. These physical phenomenon can be:

- Compton effect and photoelectric effect;
- e^+- e^+ pair production, that occurs when the available energy for the center of mass is equal to the sum of the rest energy of the two electrons, which means $\simeq$ 1 MeV.

If, after the pair production mechanism, a Bremsstrahlung process occurs, generated by electrons and positrons that will produce other γ photons that consequently will produce other pairs, this phenomenon will be called *Air Showers*. These showers are divided in two

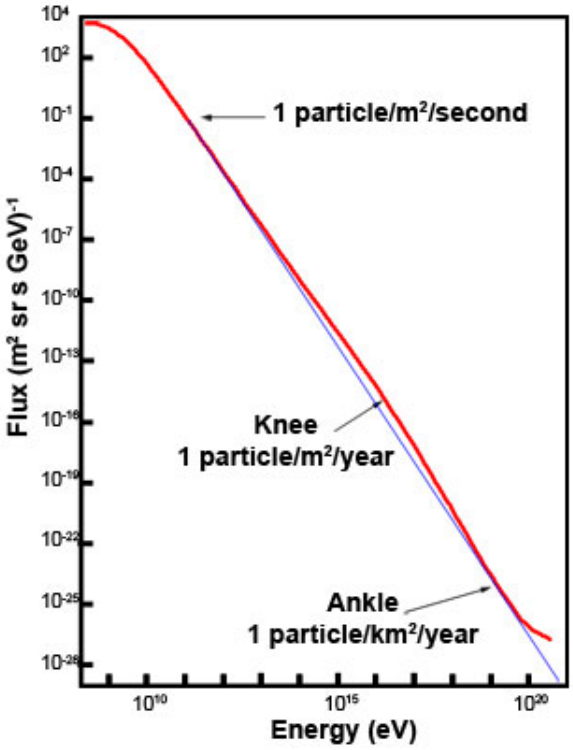

Figure 1.1: Energy spectrum of the cosmic rays, with the indication of knee and ankle.

categories, *electromagnetic* or *hadronic* showers, depending on the nature of the primary particle, that is the particle that generates them. The electromagnetic ones are generated by electrons, photons and positrons, while the hadronic ones by protons, neutrons and pions plus a secondary electromagnetic shower.
In Figure 1.2 wag a scheme is reported with the two kinds of showers and the resulting particles that are produced during the shower.

- **Electromagnetic Air Showers**: if we consider that the primary particle originating an electromagnetic air shower is a γ ray with energy E_0, when it enters the atmosphere, it interacts with the electromagnetic field of the atoms, and after travelling an length X_0, produces an e^+e^- pair or, more rarely, a $\mu^+\mu^-$ couple since muons have a smaller cross-section. After the pair production, the electron and positron will have an energy of $E_0/2$ each. They, in turn, will cover an length X_0 before producing a γ photon of energy $E_0/4$ by Bremsstrahlung. These secondary γ photon can produce further e^+e^- couples and the process keeps going on, doubling its particles at each X_0, until a threshold energy is reached. A γ-ray photon can produce a couple e^+e^- down to an energy of 83 MeV, below this energy the process ends.
  The shower reaches its maximum when the energy of the single particles e^+ande$^-$ assumes the critical value of $E_c = 83$ MeV. At this energy, the energy losses by ionization and Bremsstrahlung are balanced. The photons generated by these particles are approximately characterized by an energy of few MeV, and photoelectric absorption

and the Compton scattering become the dominant processes, and the shower stops developing.
The transverse development of the shower is due to the coulombian scattering and to the particle interactions with the Earth magnetic field. However, due to the relativistic velocity of the particles, the latter effect is quite negligible, making the electromagnetic shower compact and strongly collimated along the incident direction of the primary γ ray.

- **Hadronic Air Showers** These kind of showers are produced mainly by protons, since they form the most of cosmic rays. When they enter the atmosphere, they interact with their atoms to create secondary particles as pions, kaons, nucleons that, in turn, can generate other particles. The formation of secondary particles keeps going on until the pion production threshold is reached, corresponding to 1 GeV. When the energy of the particles reaches this critical value, the shower stops developing.
  The development of an hadronic shower is more complicate than that of an the electromagnetic one, because many more reaction channels are involved. In fact, protons interacting with the atmospheric atoms can produce kaons, pions and nucleons that in turn can split into other different reaction. In particular kaons can decay in muons, pions and neutrinos; charged pions can decay in muons and neutrinos; some muons can decay in electrons; and neutral pions can decay in γ photons. Due to all these different channels, the transverse development of hadronic showers is generally much larger than the electromagnetic ones.
  A typical hadronic shower is formed by three different components: a hadronic core, made by high energy nucleons and mesons that decay in muons and neutrinos; a muonic component, deriving by the kaon and pion decays. Due to the long lifetime, they can even reach the ground, carrying on a significant fraction of the energy of the primary particle. Nevertheless, a small fraction of muons decay into electrons; an electromagnetic component, due to the neutral pions decay. Neutral pions are about 30% of the total pions produced in the shower, and can generate two γ photons.

The γ-ray photons in the hadronic showers are indistinguishable from those of the electromagnetic ones, and they represent the main source of background in ground-based γ astronomy.

1.2.1 Cherenkov effect

When a charged particle crosses a medium with a velocity that exceed that of the light in that medium, a coherent electromagnetic radiation is emitted, that propagates with a conic wave front. The effect is called *Cherenkov effect*, and it occurs because the charged particles polarizes the atoms that lie along its path, transforming them into electric dipoles. Actually this effect makes the return of the dipoles to their rest state to be coherent: there is not a charge separation and the emitted radiation results to be coherent. In this way it can propagate freely instead of being absorbed locally. The emission of electromagnetic radiation is the result of the time variation of the charge.

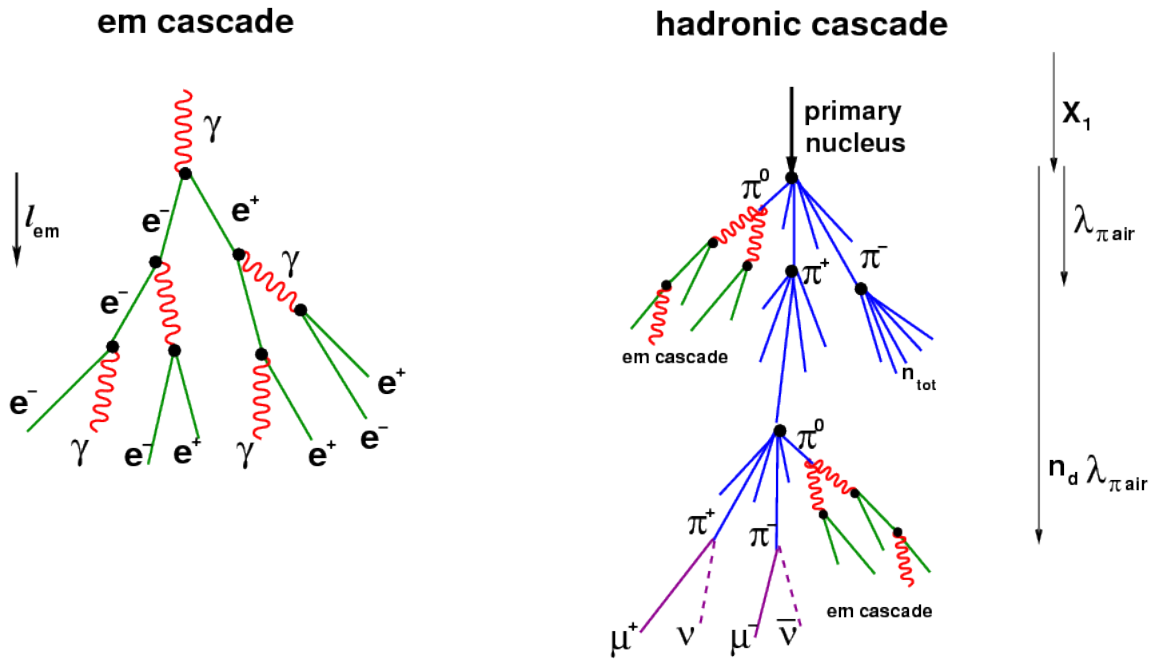

Figure 1.2: On the left an electromagnetic air shower and on the right a hadron air shower are represented.

If we call n the refraction index of a medium, we can say that if the particle has a velocity $v < c/n$, the polarization created by the particle has a spherical symmetry, with no emission of radiation. If the velocity is $v > c/n$ the polarization is asymmetric and the result is a radiative contribution, called *Cherenkov radiation*. It is emitted not by the particle itself, but by the atoms of the medium that surrounds the particle. The relativistic particle loses a bit of its energy, that returns as radiations, so the charges that constitute the dipole moment are accelerated to restore the equilibrium, emitting the radiation.
Since the radiation propagates with a conic wave front, the angle between the particle path and the emitted radiation, called θ, is given by:

$$\theta = \arccos \frac{1}{n\beta}, \tag{1.2}$$

with $\beta = v/c$, and obviously the Cherenkov light can be emitted only if $\beta > 1/n$, i.e. if the particle is relativistic with a velocity $v > c/n$. The velocity cannot be larger than that of the light, and so we can infer a maximum limit on the angle θ:

$$\theta_{max} = \arccos \frac{1}{n} \tag{1.3}$$

The Cherenkov photons produced in the Earth's atmosphere have to travel longer distances before reaching the ground, and because of this they will distribute on a larger surface, instead of the photons generated at lower altitudes. All this results in a spread of the signal

and in a decrease of surface energy density of the photons. The area where those photons can reach the ground is called Cherenkov pool; to give an example of its size, we can think about the MAGIC telescope: it is situated at $\simeq$ 2200m a.s.l. and for particle with 1 TeV of energy, the radius of the Cherenkov pool results to be $\simeq$ 120 m, as seen in Figure 1.3. Since the number of emitted photons is $\propto \lambda^{-2}$, most of the Cherenkov emission is in the UV-blue band. In addition, during the propagation of the light, they are absorbed or scattered in the atmosphere according to the Rayleigh or Mie scattering processes; the first one occurs with small scattering centers (atoms and molecules), while the second one occurs with larger scattering centers (dusts and aerosols).

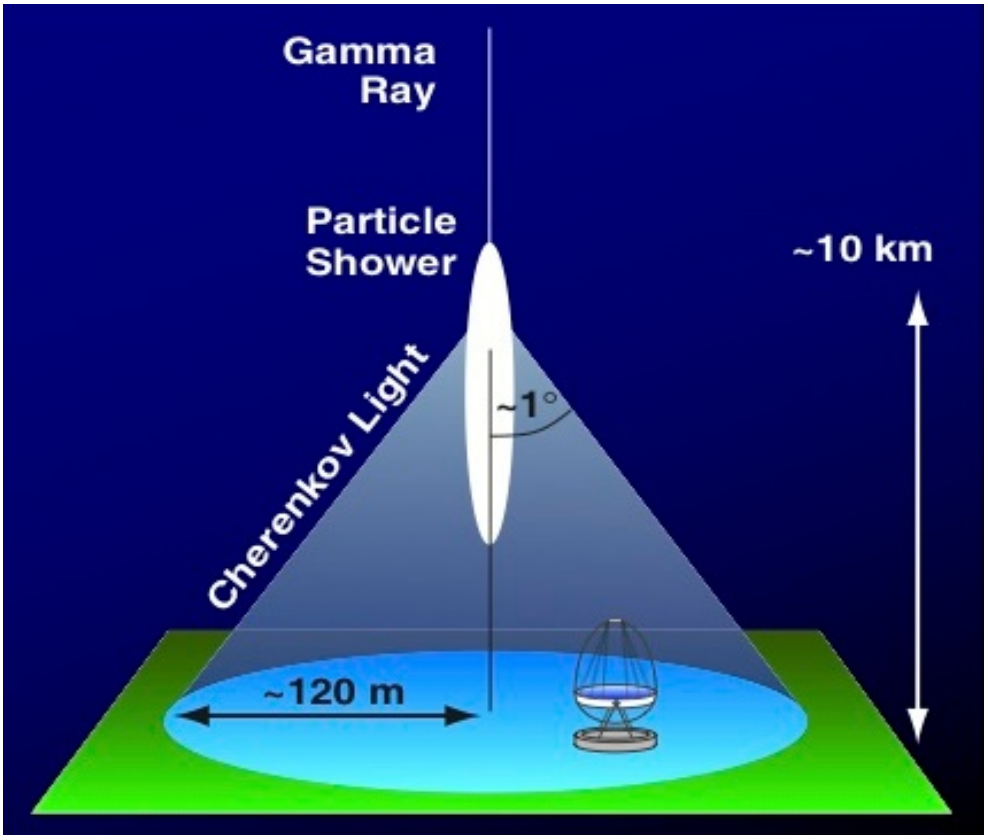

Figure 1.3: Graphic representation of Cherenkov light cone and Cherenkov pool for the case of the MAGIC telescope.

1.3 Non-thermal emission mechanisms of γ rays in the Universe

In the Universe, γ rays are produced in presence of high energy charged particles. The processes generating γ rays can be distinguished into two main classes:

- Leptonic processes, in which relativistic electrons generate radiation that can produce γ-ray photons through inverse Compton;
- Hadronic processes, where the γ-ray emission is generated by the interaction between ultra-relativistic protons and the photon field, that is the main one, or the matter surrounding the source, called *pion-decay*.

For this reason, it is necessary to understand which mechanisms are able to accelerate particles up to relativistic energies, and which are the radiative processes involving such charged particles.

1.3.1 The Synchrotron radiation

Relativistic electrons traveling through a magnetic field generated by a celestial object, follow helical paths around the magnetic field lines, and emit synchrotron radiation since they are subjected to a centripetal acceleration. The emission spectrum of a particle distribution can range from radio to γ-ray energies, and it is a function of the magnetic field intensity and the electron density.
A charged relativistic particle in a magnetic field is subjected to the Lorentz force, and its motion equation is:

$$\gamma m \frac{d\vec{v}}{dt} = \frac{q}{c}\vec{v} \wedge \vec{B} \tag{1.4}$$

where the solution of the motion equation in the perpendicular direction results in an uniform circular motion with a frequency called *non-relativistic gyrofrequency*:

$$\nu_g = \frac{qB}{\gamma mc}. \tag{1.5}$$

So the motion of the relativistic electrons is an helicoidal path with constant pass, along the lines of the magnetic field. It is important to introduce also the angle between the magnetic field B and the velocity vector $\vec{v}$, called *pitch angle* α and given by $\vec{v} \wedge B$. The Larmor frequency is then given by:

$$\nu_L = \frac{v \sin\alpha}{r_L}, \tag{1.6}$$

where r_L is the Larmor radius, defined as the radius of the circular motion of a charged particle in the presence of a uniform magnetic field.
The synchrotron radiation is strongly collimated in a cone characterized by an angle θ along the particle motion direction; remembering that from the theory of the special relativity a particle at rest has an energy $E = \gamma mc^2$, the angle θ is given by:

$$\theta \simeq m_q c^2 / E = 1/\gamma. \tag{1.7}$$

For this reason, an hypothetical observer is reached by the radiation only when such cone is pointing towards its direction. The observer will see the signal in an interval of time:

$$t_2 - t_1 \simeq \frac{2}{\gamma \nu_g \sin\alpha}, \tag{1.8}$$

while the arrival distance differences of the signals are then given by:

$$t_2^a - t_1^a \simeq \frac{2}{\gamma \nu_g \mathrm{sin}\alpha} \left(1 - \frac{v}{c}\right). \tag{1.9}$$

If we approximate the second member of the equation, we can find that the observer can see a series of pulses with a duration:

$$\Delta t^a \simeq (\gamma^3 \nu_g \mathrm{sin}\alpha)^{-1}, \tag{1.10}$$

with a frequency of $2\pi \mathrm{sin}\alpha/\nu_{\mathrm{g}}$. The higher the particle energy, the smaller the aperture θ of the emission cone. This has a direct implication on the frequency of the emitted radiation: the smaller is θ, the smaller is the emission time, and higher is the characteristic frequency ν_c:

$$\nu_c = \frac{3}{2}\gamma^2 \omega_{cycl} \tag{1.11}$$

where $\nu_{cycl} = (eB\mathrm{sin}\alpha)/(2\pi \mathrm{m})$ is the cyclotron frequency. The physics concept of the spectrum of the emission given by a single particle is quite simple: in the cyclotron case there is not beaming, and so the electric field $\mathcal{E}(t)$ has a sinusoidal form, seen from the observer, and its Fourier transform is a *Delta* function, i.e. a cyclotron line. When the particles become relativistic, the beaming effect makes the emission to be conic, and because of this, the electric field changes its shape and its Fourier transform becomes a function peaking at the critical frequency ν_c. Since its motion is periodic, the spectrum is composed by a series of spectral lines at the characteristic frequency and by all their harmonics.
However, the separation between the emission lines becomes smaller and smaller with increasing particle energy, thus forming a continuum spectrum. In Figure 1.4[3] the spectrum of emission of the first 20 harmonics of mildly relativistic cyclotron radiation is shown.

The spectrum is given by:

$$F(\nu) = \left(\frac{\nu}{\nu_c}\right)^{\frac{1}{3}} \text{ for } \nu/\nu_{\mathrm{c}} \ll 1 \tag{1.12}$$

and

$$F(\nu) = \left(\frac{\nu}{\nu_c}\right)^{\frac{1}{2}} e^{\frac{-2\nu}{\nu_{\mathrm{c}}}} \text{ for } \nu/\nu_{\mathrm{c}} \gg 1 \tag{1.13}$$

The observed radiation is given by all the contributions resulting from an ensemble of particles, characterized by a given energy distribution. The most common function for a distribution of high energy particle is given by:

$$N(\gamma) = k\gamma^{-s}. \tag{1.14}$$

To compute the radiated power, it is important to introduce the function F(x) as:

$$F(x) = x \int_x^\infty K_{5/3}(x' dx'), \tag{1.15}$$

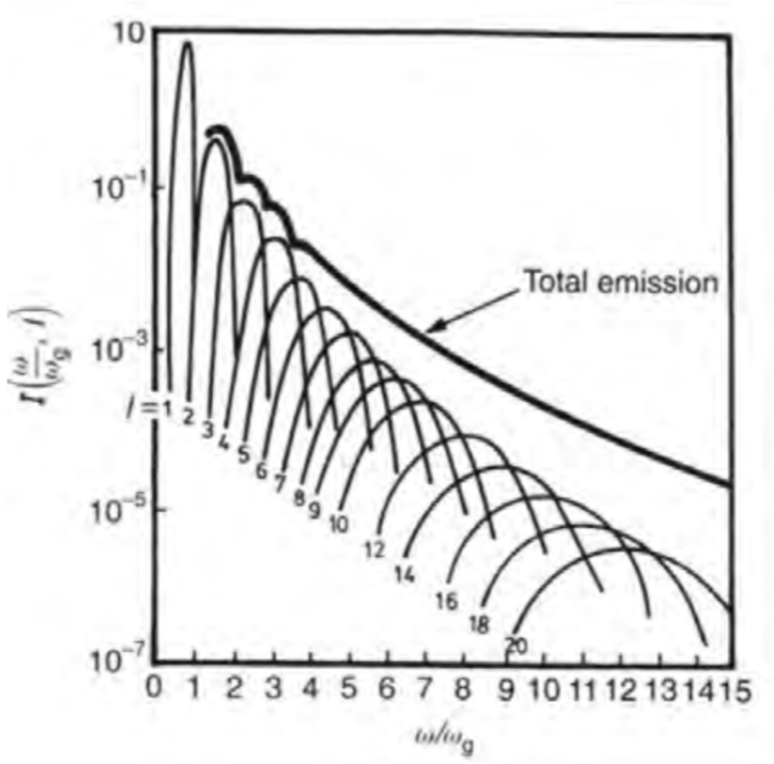

Figure 1.4: The spectrum of emission of the first 20 harmonics of mildly relativistic cyclotron radiation for an electrons with v = 0.4c.

where $K_{5/3}$ is a modified fractional Bessel function and $x = \nu/\nu_c$. The radiated power is then given by integrating the emission over all the particle distribution:

$$F(\nu)_{tot} = \frac{k}{2}\left(\frac{\nu}{\nu_{cycl}}\right)^{\frac{-(s-1)}{2}} \int_{x_1}^{x_2} F(x) x^{\frac{s-3}{2}} dx. \tag{1.16}$$

If the particle energy distribution follows a power-law function characterized by an index $-s$, the emission spectrum is still described by a power-law function, but with index $-(s-1)/2$. In Figure 1.5[3] a generic synchrotron emission spectrum is shown.

In the emitting source, absorption processes can occur, due to the interaction between the photons and the plasma, called *Self Absorption effect*: photons in certain quantum states can stimulate successive emissions of other photons in the same quantum state. To explain this self absorption process, we need to solve the Radiative Transport Equation:

$$\frac{dI_\nu}{d\tau_\nu} = -I_\nu + S_\nu, \tag{1.17}$$

where I_{nu} is the specific intensity, τ_ν is the optical depth and S_ν is the source function,

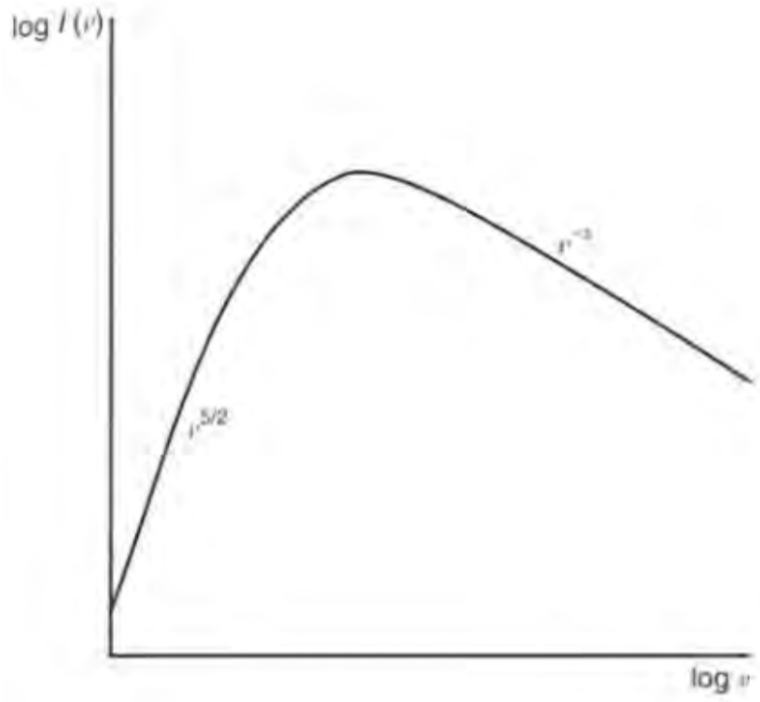

Figure 1.5: Spectrum of a synchrotron emission. The change of slope from $I(\nu) \propto \nu^{5/2}$ to $I(\nu)d\nu \propto \nu^{(1-s)/2}$ can be easily seen in the passage from low to high frequencies.

defined as:

$$S_\nu = \frac{j_\nu}{\alpha_\nu}, \tag{1.18}$$

with j_ν = emission coefficient and α_ν = absorption coefficient.
For an isotropic distribution of electrons in a homogeneous magnetic field, the absorption coefficient results to be [15]:

$$\alpha_\nu = -\frac{1}{8\pi m_e \nu^2} \int_{\gamma_{min}}^{\gamma_{max}} d\gamma \gamma^2 \frac{\partial}{\partial \gamma} \left[\frac{N_\gamma}{\gamma^2} \right] P_\nu(\nu, \gamma), \tag{1.19}$$

with γ_{min} and γ_{max} = interval of the electron energetic distribution and $P_\nu(\nu, \gamma)$ = emitted power. So for $\gamma_{min} = 0$ and $\gamma_{max} = \infty$, we obtain the following expression for a source function S_ν:

$$S_\nu = \frac{j_\nu}{\alpha_\nu} = \frac{P_\nu}{4\pi\alpha_\nu} \propto \nu^{5/2}, \tag{1.20}$$

where j_ν is the emission coefficient. So if the source is homogeneous, we obtain:

$$S_\nu = \frac{j_\nu}{\alpha_\nu}(1 - e^{-\alpha_\nu} R), \tag{1.21}$$

where R is the source dimension. For low values of the optical depth $\tau = \alpha_\nu R$ we obtain:

$$I_\nu \simeq j_{\nu R} \propto \nu^{-(s-1)/2}, \tag{1.22}$$

while for high values:

$$I_\nu \simeq \frac{j_\nu}{\alpha_\nu} \propto \nu^{5/2}. \tag{1.23}$$

Since the electrons are emitting radiation, they lose their energy, so the synchrotron process is a cooling process.

1.3.2 The Inverse Compton scattering

The Compton scattering is a process related to the collisions between an electron and a photon, with the ensuing energy transfer from the photon to the electron. However, when the energy of the electron is much greater than that of the photon, the collision can transfer energy from the electron to the photon. Such process is called inverse Compton scattering. In particular, when relativistic electrons interact with low energy photons, the energy of the latter can be increased up to the X- and γ-bands. In other words, the inverse Compton is a cooling process that transfers part of the energy of the electrons to the photon field. Given an energy-density electron distribution and a photon field distribution, it is possible to compute the inverse Compton contribution in two regimes: in the Thomson limit, and where it is no more valid, in the Klein-Nishina limit.
When the Thomson approximation becomes no more valid, we need to use the full Compton cross-section computed by Klein and Nishina with the help of the quantum electrodynamics.So the approximation in full Klein-Nishina is the limit of the standard Klein-Nishina for $E_\gamma >> m_e c^2$, where E_γ is the photon energy in the rest frame of the electron (ERF). All the calculations reported below are made in the so called *head-on approximation*, which means they are done for $\gamma >> 1$ and for a photon traveling in the ERF with an angle $\theta = -1$. This is a consequence of the fact that while in a laboratory the photon gas is isotropic, in the ERF it is beamed, and so we can assume that most of the photons are seen 'head-on' by the electron.

- In the Thomson regime, the photon energy, in the electron frame, satisfies the relation $E_\gamma << m_e c^2$. In this case the cross-section of the process, called Thomson cross-section, is independent from the energy of the photon and it is given by:

$$\sigma_T = \frac{8}{3}\pi r_e^2. \tag{1.24}$$

  The Thomson cross-section is used to compute the energy losses given by:

$$\frac{dE}{dt} = \frac{4}{3}\sigma_T c \gamma^2 \beta^2 U_{rad}, \tag{1.25}$$

  where U_{rad} is the energy density of the radiation.
  In Figure 1.6 [5] the inverse Compton spectrum given by a mono-energetic electron population can be seen, with its characteristic features. In Thomson regime, the calculation of the emission spectrum is made by starting from that of a single electron and then by integrating over all the energetic distribution of the electrons. As

Blumenthal e Gould [5] found, since we are in Thomson limit, the distribution of diffused photons, is expressed by:

$$\frac{dN_\gamma}{dtdE} = \frac{\pi r_0^2 cn(E_{in})dE_{in}}{2\gamma^4 E_{in}^2}\left[2E\ln\left(\frac{\mathrm{E}}{4\gamma^2\mathrm{E_{in}}}\right) + \mathrm{E} + 4\gamma^2\mathrm{E_{in}} - \frac{\mathrm{E}^2}{2\gamma^2\mathrm{E_{in}}}\right]. \tag{1.26}$$

To obtain the total spectrum we have to integrate over the whole energy distribution of the electrons. For a distribution $dN_e = N_e(\gamma)d\gamma$, this spectrum will result in:

$$\frac{N_{tot}}{dtdE} = \int_{\gamma_1}^{\gamma_2}\int N_e(\gamma)d\gamma\frac{dN_\gamma}{dtdE}dE_{in}, \tag{1.27}$$

where γ_1 and γ_2 are the kinematic constraints of the problem, given by:

$$\gamma_1 = \max\left[\frac{1}{2}\sqrt{\frac{\mathrm{E}}{\mathrm{E'}}}, \gamma_{\min}\right] \text{ and } \gamma_2 = \min\left[\frac{1}{2}\sqrt{\frac{\mathrm{E}}{\mathrm{E'}}}, \gamma_{\max}\right]. \tag{1.28}$$

Since we are in Thomson regime, and if we have a power law electron distribution given by:

$$N_e(\gamma) = K_e\gamma^{-p} \text{ if } \gamma_{\min} < \gamma < \gamma_{\max} \text{ and } \mathrm{N_e}(\gamma) = 0 \text{ elsewhere}, \tag{1.29}$$

the result is the following analytic expression, for a photon field generated by a black body:

$$\frac{N_{tot}}{dtdE} = \pi^{-1}(r_0^2/\hbar^3c^2)K_e(kT)^{(p+5)/2}F(p)E^{-(p+1)/2} \tag{1.30}$$

where the parameter $F(p)$ depends on the Riemann's functions and T is the temperature.

- When the Thomson regime is no more valid, when $E_\gamma \gg m_e c^2$ in the electrons rest frame, the Klein-Nishina regime occurs. In this case the cross-section is given by the full Compton cross-section:

$$\sigma_{KN} = \frac{3}{4}\sigma_T\left\{\frac{1+x}{x^3}\left[\frac{2x(x+1)}{1+2x} - \ln(1+2\mathrm{x})\right] + \frac{\ln(1+2\mathrm{x})}{2x} - \frac{1+3x}{(1+2x)^2}\right\}, \tag{1.31}$$

and it can be seen that when the energy of the photon increases, the real cross-section decreases compared to that of Thomson, as seen above. In the asymptotic KN approximation of the cross-section, the energy loss rate is [5]:

$$\frac{dE}{dt} = \frac{3\sigma_T}{8}m_e^2c^5\int\frac{n(E_{in})}{E_{in}}\Big(\ln\frac{4\gamma E}{m_e c^2} - \frac{11}{6}\Big)dE_{in}. \tag{1.32}$$

The integration of the equation above, for the case of radiation field distributed as a black body, gives:

$$\frac{dE}{dt} = \frac{\sigma_T\pi^3}{2h^3}\Theta m_e^4c^6\ln(4\gamma\Theta - \mathrm{C_E} - \mathrm{C_l}), \tag{1.33}$$

where $\Theta = k_B T/(m_e c)$ is the dimensionless temperature of the radiation field, $C_E \simeq 0.5772$ is the Euler constant, and $C_l \simeq 0.570$. It is interesting to note that in the case of strong KN regime the cooling rate increases logarithmically with γ and is essentially proportional to T^2, on the contrary, in the Thomson limit $dE/dt \propto T^4\gamma^2$. To obtain the spectrum of the diffuse photons, the method is the same made for the Thomson regime, with the difference that here we must use the Klein-Nishina cross-section. Following the approach used by Jones [16], the emitted spectrum for a single photon will be:

$$\frac{dN_\gamma}{dtdE_e} = \frac{2\pi r_0^2 m_e c^3 n(E_{in}) dE_{in}}{\gamma E_{in}} \mathcal{F}(E, E_{in}, \gamma), \tag{1.34}$$

where $n(E_{in})$ is the photon field density, E_e is the initial energy of the electrons and $\mathcal{F}(E, E_{in}, \gamma)$ is a function depending on E, E_{in} and γ used to make the above equation more compact. So if the electrons energetic distribution is given by Equation 1.28, the total Compton spectrum will result in:

$$\frac{N_{tot}}{dtdE} = \int\int dE_{in} d\gamma N_e(\gamma) \frac{dN_\gamma}{dtdE}, \tag{1.35}$$

and the final result can be found by substituting the spectrum for a single electron given in Equation 1.32 with $0 \leq \gamma < \infty$.

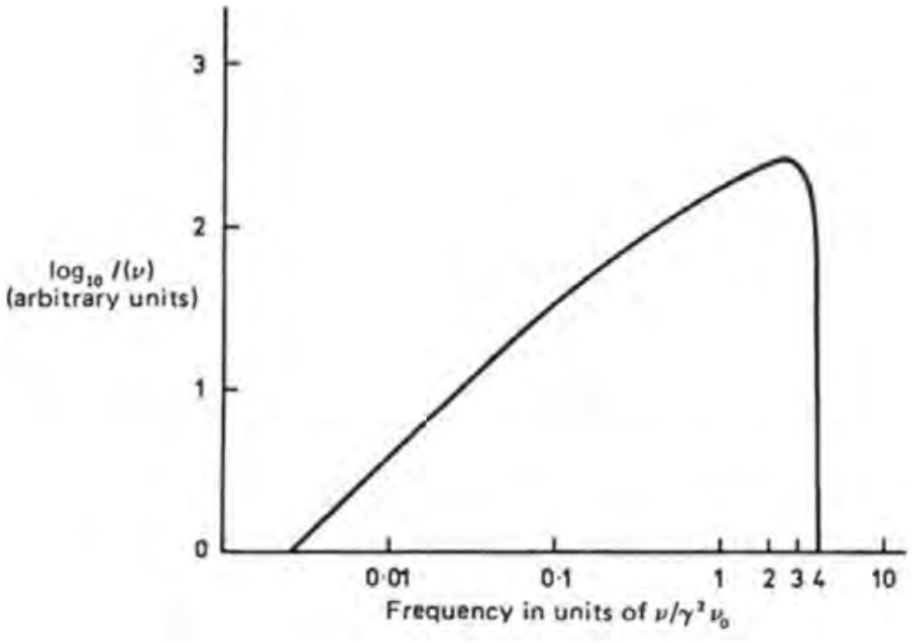

Figure 1.6: Spectrum due to inverse Compton scattering given by a mono-energetic electron population.

1.4 γ-ray propagation

When γ rays are emitted from a distant source, they have to travel enormous distances before reaching the observer and so during their path they can be absorbed or they can interact with other particles or photons that can cause a flux decrease. The cross-section of this process is given by the Bethe-Heitler formula [6]:

$$\sigma(E,\epsilon) = 1.25 \times 10^{25}(1-\beta^2)\left[2\beta(\beta^2-2) + (3-\beta^4)\ln\left(\frac{1+\beta}{1-\beta}\right)\right] \tag{1.36}$$

where $\beta = \sqrt{[1-(m_e c^2)^2/(E\epsilon)]}$, m_e the electron mass, E is the energy of the γ-photon and the ϵ is the energy of the background photon.

Pair production is a source of opacity for γ-rays when the mean free path is shorter than the distance of their generating source. The main free path is inversely proportional to the energy of the γ-ray, so photons with energies higher than 100 TeV coming from distant extragalactic sources are completely absorbed. The detectability of photons with lower energies depends basically to the source distance. For photons with energies < 10 GeV the Universe is, in practice, totally transparent.

The probability for a photon to survive in their path from the source to the observer is expressed by:

$$\frac{F_{ob}}{F_{em}} = e^{-\tau(E,z)}, \tag{1.37}$$

where F_{ob} is the observed flux, F_{em} the emitted one, and $\tau(E,z)$ the optical depth. The latter is a function of photon energy, and the redshift of the source since it is related to its distance. The optical depth is obtained by convolving the numerical density of the background photon field,n_e, with the cross-section expressed by the Equation 1.36, and afterward by integrating over the distance $l(z)$, the scattering angle θ, and the corrected energy of the background photons according to their redshift:

$$\tau(E,z) = \int_0^z dl(z)\int_{-1}^{1} d\cos\theta \int_{\frac{2(\mathrm{m_e c^2})^2}{\mathrm{E}(1-\cos\theta)}} \mathrm{d}\epsilon(\mathrm{z})\mathrm{n}_\epsilon(\epsilon(\mathrm{z}),\mathrm{z})\sigma(\mathrm{E}(\mathrm{z}),\epsilon(\mathrm{z}),\theta) \tag{1.38}$$

where the distance $l(z)$ is a function of the cosmological parameters and given by [7]:

$$\frac{d\Omega}{dz} = \frac{c}{H_0}\frac{1}{(1+z)[(1+z^2)^2(\Omega_M z+1) - \Omega_\Lambda z(z+2)]^{1/2}} \tag{1.39}$$

with Ω_M matter density, and Ω_Λ dark energy density. This absorption makes the observed source flux steeper at the high energies. So, the observed energy spectrum of distant source has to be corrected by extragalactic background light absorption.

1.4.1 The Extragalactic Background Light

The EBL is formed by the total contribution of the light emitted by the stars either directly or reprocessed by cosmic dust and gas. The spectral distribution of the EBL ranges from

the near UV up to the far IR and shows two distinct peaks, as shown in Figure 1.7 [8]. The first bump, located at 1 μm, is due to the contribution of the stars. The second is due to the star light reprocessed by dusts, and includes both the thermal continuum and the emission lines of the PHA (**P**oly **H**ydroxy **A**lkanoates) molecules. At low wavelengths the flux decreases rapidly because of the attenuation due to the molecular hydrogen in the stellar atmospheres, and in the interstellar and intergalactic medium, while at higher wavelengths there is another component of radiation background, called **C**osmic **M**icrowave **B**ackground: it is the residual electromagnetic radiation produced by the Big Bang that permeates the universe.

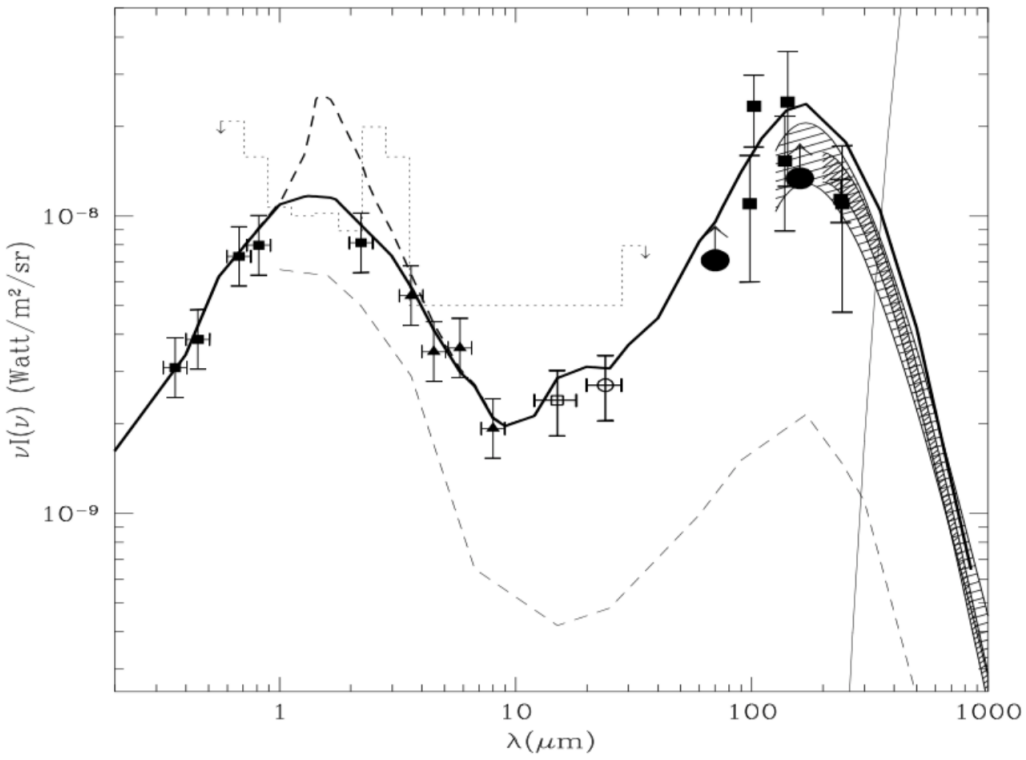

Figure 1.7: The Cosmic Extragalactic Background spectrum, with its two characteristic bumps at $\simeq 1\mu m$ due to the star contribution and at $\simeq 150\mu m$ due to the star light reprocessed by dusts.

1.5 γ-ray sources

γ-ray sources can be divided into galactic and extragalactic. In turn galactic sources can be divided into point-like and extended sources depending on their distance from us and on the Point Spread Function (PSF) of the instrument we use to observe them. Due to their

proximity, their γ emission is not affected by absorption from the cosmic background radiation. In the extended sources particle acceleration and the ensuing γ emission is supposed to originate from the interaction between the source and the surrounding environment, whereas in point like sources it originates inside the jets or in connection with relativistic fluxes.
The main sources are:

- Extragalactic sources:
  1. **Active Galactic Nuclei**: these objects will be treated in the next section.
  2. **Gamma ray bursts**: these are the most powerful events that occur in the Universe, and the γ-ray emission is thought to be originated by the conversion of gravitational energy in radiant energy, after the collapse of a massive star into a neutron star or a black hole.
  3. **Star forming galaxies**: starburst galaxies and ultra-luminous infrared galaxies are part of this category; they have a high rate of Supernova explosions and high gas densities, and for this reason the γ-ray emission can reach high levels.
- Galactic sources:
  1. **Binary systems**: in these systems a star orbiting around a compact object such as a neutron star or a black hole, loses matter due to gravitational interaction. Such matter forms a compact disk, heated by the strong viscosity forces, that emits X rays. Usually, also two collimated jets shot off the central region and perpendicular to the disk plane, are associated with these sources. The plasma ejected by the jet, by encountering the surrounding disk matter, generates shock waves that can accelerate particles. Both leptonic and hadronic mechanisms are supposed to be at the base of the γ emission, since electrons, protons, and heavier particles are all part of the emitting plasma.
  2. **P**ulsar **W**ind **N**ebulae (PWN): they are fast rotating neutron stars characterized by very strong magnetic fields, misaligned with respect to the rotation axis. The simultaneous presence of rotation and magnetic field produces a strong radiation at the poles, that a hypothetical observer see as pulsed emission. The rotating magnetic field generates a high electric field that is supposed to extract charged particles from the star surface, filling the magnetosphere. There is a zone, called *light cylinder*, out of which the open magnetic field lines allow particles to be ejected and accelerated. The γ emission is dominated by the pulsed emission coming from the star and by the stable emission of the nebula.
  3. **Supernova remnants**: they are the results of supernova explosions. A giant star, approaching the end of its life, starts to collapse very quickly. Part of the energy of the collapse is transformed in shock waves that bounce on the heavy nucleus and is transferred to the external layers. Such layers are wildly ejected far away from the central nucleus, causing the complete collapse of the star.

Such ejected envelope forms the supernova remnant. In its inner part cosmic rays are accelerated causing the production of γ rays.

1.6 Active Galactic Nuclei

Active Galactic Nuclei (AGNs) are galaxies whose nuclei show a non thermal emission that is variable and very strong. In their spectra strong emission lines are present in the optical, IR, UV and X band. These kind of cosmic sources represent $\simeq 3\%$ of the total fraction of galaxies, and differ from their luminosity and emission profile. For their description and classification I refer to [3], [9], [10] and [11].

1.6.1 Classification of AGN

AGNs are classified more on the way we observe them, than to their intrinsic properties, and in particular on how their geometry is aligned with our line of sight. There are some main parameters used to classify them: the intensity of radio emission, the morphological profile and the optical emission of emission lines.
According to the above observables, AGNs can be schematically classified as:

- **Quasars**: These sources are AGNs and their nucleus is very luminous especially in the optical band, and they are generally located at high redshifts. They can be radio quiet ($\simeq 90\%$) or radio loud ($\simeq 10\%$), depending on their radio emission, but only radio-loud Quasars have the characteristic jets of AGNs. Their characteristics are the luminosity that exceeds that of a standard galaxy by a factor 10^5, a very strong and variable γ-ray emission and a presence of large emission lines emitted with high velocities. They appear as blue sources because they are very bright in the UV.

- **Blazars**: these are associated in the most of cases with elliptical galaxies, and they are the most luminous AGNs in the γ-ray band. They also show a consistent radio emission. They are very fast variable sources, over the day or shorter timescales. Their luminosity can vary by up to 20% in a day timescale and even by up to a factor 100 over longer timescales. Spectra of Blazars are characterized by a double bump structure, one in lower energies, interpreted as synchrotron radiation produced by relativistic electrons interacting with magnetic fields, and one at higher energies, interpreted as inverse Compton emission produced by the interaction of relativistic electrons with a low energy photon field locally available.
  Blazars are divided in two sub-classes: the **F**lat **S**pectrum **R**adio **Q**uasars (FSRQs), characterized by a flat spectrum in the optical band with spectral indexes $\alpha \simeq -0.5$, and **BL L**acertae (BL Lacs) objects, with the optical spectrum dominated by the continuum. In particular, BL Lac are subdivided in other sub-classes depending on the position of the peak of the synchrotron bump: LBL stands for low energy peaked, IBL stands for intermediate energy peaked and HBL stands for high energy peaked. Anyway nowadays this classification is pretty overcome; in fact to classify this kind

of sources, today the frequency of the synchrotron peak is checked, introducing a different classification:

  - a BL Lac with a frequency of synchrotron peak that is $\nu_{peak}^{syn} < 10^{14}$Hz is called **L**ow **S**ynchrotron **P**eaked, (LSP);
  - a BL Lac with a frequency of synchrotron peak that is $10^{14} < \nu_{peak}^{syn} < 10^{15}$Hz is called **I**ntermediate **S**ynchrotron **P**eaked, (ISP);
  - a BL Lac with a frequency of synchrotron peak that is $\nu_{peak}^{syn} > 10^{15}$Hz is called **H**igh **S**ynchrotron **P**eaked, (HSP).

- **Radio Galaxies**: they are characterized by a very strong radio emission. Their morphology shows two radio lobes that emerge from the galaxy center. The radio emission is not of thermal origin, but due to the synchrotron radiation generated by relativistic charged particles. The radio emission can be originated in the lobes, but also in compact cores within the nucleus. Often, relativistic jets are associated to the radio lobes. As explained in the next section 1.6.2, their classification depends only on which line of sight we see them.

- **Seyfert Galaxies**: they are AGNs with the lowest luminosity whose host galaxy is visible. They are generally spiral galaxies with a very bright nucleus. They are characterized by an optical emission, while the radio emission is absent. They can be distinguished into: *Seyfert I* type, characterized by optical emission lines, both large permitted lines and narrow forbidden lines; the lines widening is of kinematic origin and they have a brighter continuum and emit more in the X band than the *Seyfert II* that are instead characterized only by narrow lines and sometimes they do not show the X emission.

1.6.2 Unified model of AGN

The Unified Model of AGN allows to interpret all the characteristics of these sources according to the angle of sight under which we see them, and according to the presence of the relativistic jets. Actually all these sources listed above are AGNs.
We can describe the structure of an AGN as follows:

- a supermassive black hole that lies in the center; it is the main source of energy of the AGNs; here the gravitational energy is converted in luminous energy, according to the relation:

$$L_{acc} = c^2 \epsilon \frac{dm}{dt}, \tag{1.40}$$

  where L_{acc} is the luminosity due to the mass accretion rate into the black hole, ϵ is the efficiency of the process which can be $\simeq 0.1$ at the maximum, and $\frac{dm}{dt}$ is the mass accretion rate into the black hole;

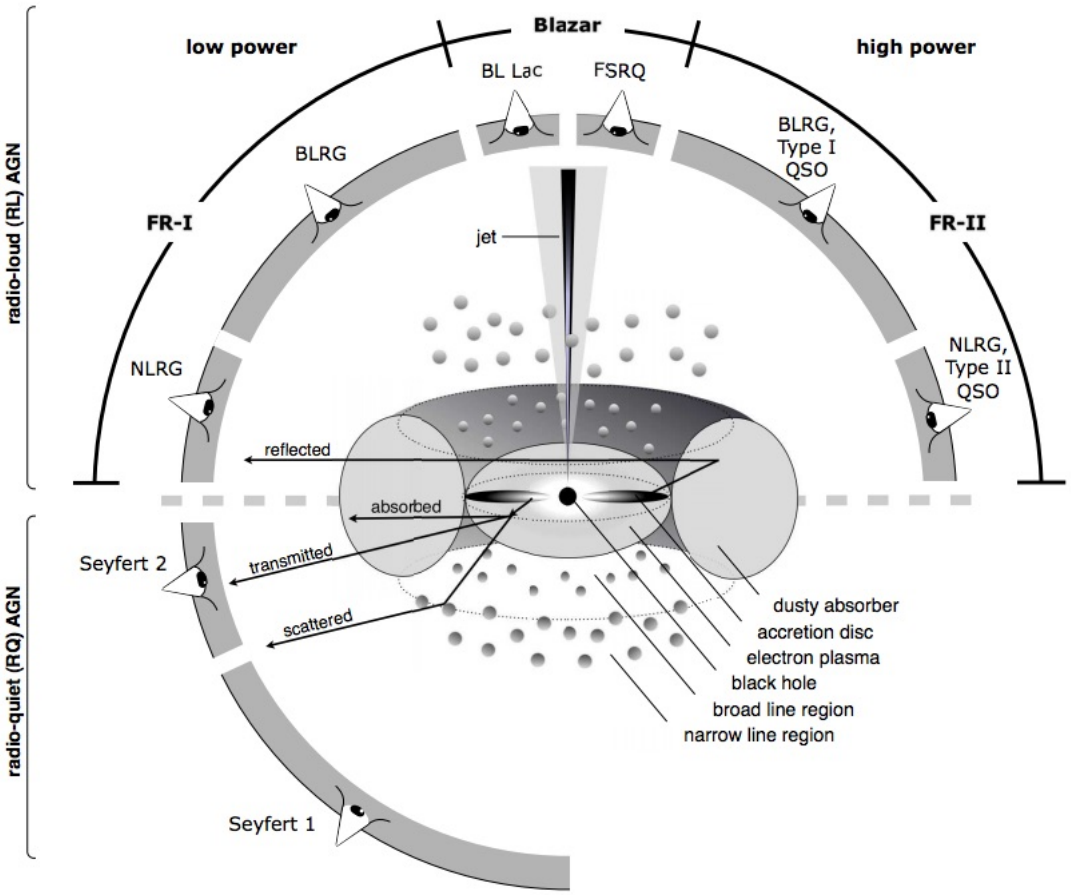

Figure 1.8: Unified model of AGN. In the inner part the AGNs composition with all its parts is represented, while in the outer part the classification of the AGNs can be seen.

- an accretion disk, generated by the matter that falls onto the black hole in a spiral trajectory around it, because of the conservation of the angular momentum. It emits X-ray radiation and it has dimensions from 10^{-3} pc to 10^{-2} pc;
- a broad line region, located beyond the accretion disk with dimensions similar to it and a spherical shape. It is formed by gas clouds with high density and low temperature. The large emission lines of AGNs are produced in this region;
- a dust torus, beyond the broad line region with $\simeq$ 1 pc of thickness and formed essentially by dust. It emits in the IR band;
- a narrow line region, surrounding the dust torus, made of gas clouds in relativistic motions around the black hole. The narrow emission lines of AGNs are produced in this region;
- two relativistic jets, excepts for radio-quiet Quasars, produced by relativistic plasma

that is shot out in the space from the central region with an angle of 90° with respect to the plane of the disk. These jets are supposed to be produced by strong magnetic fields generated by the rotation of the central supermassive black hole.

Summarizing, the model of AGNs allow them to look different depending on their orientation with regard to the line of sight of the observer. AGNs whose jets are perpendicular to the line of sight belong to Seyfert II or Radio Galaxies. In this case the central region is obscured by the torus and only narrow lines can be found in their spectra. AGNs whose jets form an angle ranging from 30 to 60 degrees belong to Seyfert I galaxies or radio-loud Quasars. Due to their orientation, the torus does not obscure completely the central region, so spectra present both broad and narrow lines, coming respectively from the broad and the narrow line region. Radio-quiet Quasars are simply AGNs without relativistic jets and finally, Blazars are AGNs whose jets point directly to the observer.
A graphic representation of this model can be seen in Figure 1.8 [11].

1.6.3 The Spectral Energy Distribution (SED) of the Blazars

Now we will focus our attention on Blazars, because these sources will be the main objects we are going to study in my thesis.
Blazars are characterized by a strong variable non-thermal emission and their SED can be identified by two peaks, as seen in Figure 1.9 [17]. The first one is located at low energies between IR and X range, and it is understood as synchrotron radiation emitted by relativistic electrons; the second peak is instead located at high energies, in the γ range, and the mechanism of emission is understood as an inverse Compton of photons on relativistic electrons.

The γ ray emission of Blazars originates in the relativistic jets along the rotation axis of these objects, which is made of ionized material in relativistic motion, and is highly collimated and permeated by various magnetic fields. The emission must come from these jets because it cannot come from the central region of Blazars: here the density is so high that γ photons cannot escape. Because of this density and optical depth that are very high, γ-rays are immediately reabsorbed, to generate a pair of $e^+ - e^-$, but this regenerate with an Inverse Compton process other γ-ray photons, and so on until the energy of the γ photons decreases below the energy threshold for the pair productions.
One of the most important consequences of jet concerns the so-called *Beaming Effect*. This causes a distortion of the observed parameters for an observer whose line of sight is almost aligned with the jet axis (blazars). If we have a source emitting isotropically in its reference system. In the observer's reference system, where the source is seen as moving close to the light speed, with $\beta = v/c \simeq 1$, we can define the *Beaming Factor* as:

$$\delta = \frac{1}{\Gamma(1 - \beta\cos\theta)}, \tag{1.41}$$

where $\Gamma = 1/(\sqrt{1-\beta^2})$ is the Lorentz factor of the emitting region and θ is the angle

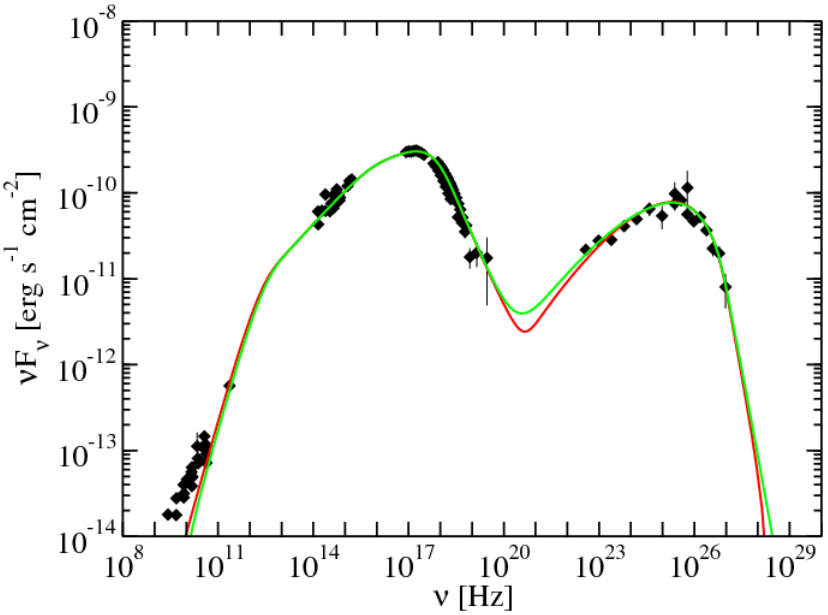

Figure 1.9: Typical Blazar SED, with the two peaks at low and high energies.

between our line of sight and the direction of the jet. The beaming factor is responsible for three main effects:

1. **superluminal motions**: the time intervals for the photon emission are different from their arriving time intervals. This leads to observe particles that move apparently with velocity higher than the light speed. Such apparently velocity v_{app} is given by:

$$v_{app} = \frac{v \sin\theta}{1 - \beta \cos\theta} \tag{1.42}$$

   For small $\theta \simeq 0$ and $\beta \simeq 1$, the observed velocity exceeds the speed of light in the vacuum;

2. **Doppler boosting**: due to relativistic effects, in the reference system of the observer, the photons are emitted inside an angle expressed by $sin\theta = 1/\Gamma$. This means that the photons emitted in the whole solid angle are seen as emitted inside a small angle in the observer's reference system. This leads to an amplification of the observed flux, $F_{obs}(E)$, given by:

$$F_{obs}(E) = \delta^p F_{em}(E), \tag{1.43}$$

   where p is an index depending on the geometry of the system and on the spectral index α, and in the case of a spherical blob it we have $p = 3 + \alpha$. Also the observed luminosity exceeds the emitted one by a factor δ^p;

3. **Blueshift in frequencies**: the observed frequencies, ν_{obs}, are higher than the emitted ones, ν_{em}, with the ensuing blue-shift of the observed spectrum. The relation

between the frequencies is $\nu_{obs} = \delta\nu_{em}$.

For what concerns the emission models of the γ emission, there are two mainly important ones: the leptonic and the hadronic one. The presence of ultra relativistic particles is required for these models, and the mechanism of acceleration is thought to be the Fermi I, with an energy distribution described by a power law function. In the leptonic model the particles involved are relativistic electrons, while in the hadronic one are protons, and because of the low mass, the most accredited model is the leptonic one; in this way, they can quickly be accelerated and cool down, explaining the AGN variability very well.

1.6.4 Emission models

The γ-rays in AGN are supposed to be originated inside the jets. There are two kind of processes to explain the γ emission: the leptonic and the hadronic ones. Both require the presence of ultra-relativistic particles whose energy distribution is described by a power law function. In the leptonic models the relativistic particles involved are electrons, while in the hadrons ones are mainly protons. However, the validity of a model versus others is still under debate, and in most of cases it depends on the specific source. Nevertheless, leptonic models are favoured because of the low mass: in fact, they can quickly accelerated and cool down, providing a valid explanation for the AGNs fast variability. However, their fast cooling does not explain how the particles can reach very high energies.

- **Leptonic models**: when leptonic processes are involved, the mechanism leading to γ-rays production is the inverse Compton scattering (see Section 1.3.2). Because different Inverse Compton processes possibly contribute to the high energy peak, each model depends mainly on the source of seed photons scattering off the relativistic electrons in the jet. For these reasons, the leptonic models can be divided into two main categories: the **S**ynchrotron **S**elf **C**ompton (SSC) models, if the Compton photons are the synchrotron photons upscattered by the same parent electrons, and the **E**xternal **C**ompton (EC) models if the scattered photons come from regions outside the jet, such as the disk or the broad line region. Differences among leptonic emission models are visualized in Figure 1.10 [3].

  Among the leptonic models, the most popular used to describe blazars emission is the one zone SSC (SSC1). It assumes that the SED is produced within a single, homogeneous, spherical blob of magnetized non-thermal plasma, in relativistic motion along the jet. The blob is filled with a homogeneous tangled magnetic field and by a population of relativistic electrons, whose spectrum can be described by different power law functions of energy. The particle and photon distributions are isotropic in the blob frame. The Self Synchrotron model is not suitable for all the sources, especially if the contribution due to the external photon fields is not negligible. For this reason this model is suitable for sources, such as BL Lac objects, where the lack

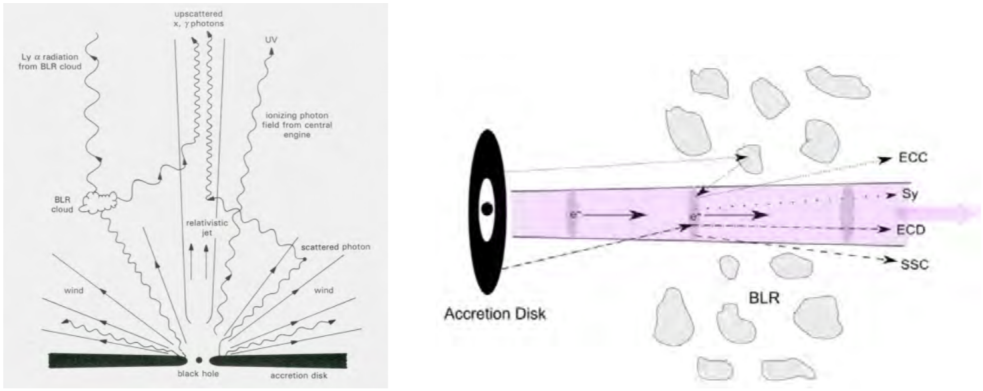

Figure 1.10: Differences between the leptonic emission mechanisms, generating Blazars' SEDs.

of emission lines in their spectra indicates a weak thermal component. The model is also applied to sources whose variability is dominated by one characteristic timescale, because this indicates only one characteristic size of the emitting region. Finally, it is also suitable for sources that show a strict correlation between the X-ray and VHE γ-ray variability; in fact this suggests that the emission in the two band (corresponding to the two bumps in the SED) is generated by the same electron population.
The one-zone SSC model (SSC1) is often described by four parameters: the beaming factor, the magnetic field, the radius of the blob and the distribution of electrons.
A slightly different version of the SSC1 is the two zone SSC model (SSC2). The main idea, supported by the observation of two different timescales in the source variability, is that the emission is generated by two different electron populations. The emission mechanism is exactly the same, but in this case two blobs of plasma are involved. This implies a doubling of the free parameters. In the EC models, the inverse Compton scattering occurs through photons generated in regions outside the jets. These photons are generally UV or soft X-photons irradiated directly from the accretion disk, deviated through scattering from the broad line region clouds, or reprocessed from the dust of the narrow line region. These photons reach the jet, interact with the relativistic electrons and increase their energy up to the γ range by inverse Compton scattering. Both the SSC and the EC models are consistent with the spectral shape of the AGNs and with the γ-ray emission of Blazars.

- **Hadronic models**: According to these models, the jet is mainly formed by relativistic protons and carries out a large part of the energy emitted by the central region. Such protonic component in the jet would be subjected to less synchrotron losses as compared with the electrons and could be accelerated more efficiently, up to 10^{20} eV. These protons that are interacting with matter, ambient photons and magnetic field, induce electromagnetic cascades that contribute to form the Compton peak.

1.7 The MAGIC telescopes

The MAGIC experiment is located at 28.75° N and 17.89° W at an altitude of 2230 m above sea level. These coordinates correspond to a site on the Roque de los Muchachos on La Palma, called "la isla bonita" of the Canary Islands, situated in the Pacific Ocean roughly 400 km away from the African coast. There the sky conditions are perfect for observations, even if occasionally there are strong winds, snowfalls, and high humidity that impede the data taking. The MAGIC telescopes can be seen in Figure 1.11.

Figure 1.11: The MAGIC I and MAGIC II telescopes, located in La Palma.

MAGIC is composed of two Imaging Atmospheric Cherenkov Telescopes (IACT), 85 m away from each other, named MAGIC I [19] and MAGIC II [18] (M1 and M2). The telescope structure is made of a set of carbon fiber tubes mounted on a circular rail of 19 m diameter. Due to the large dimensions of the mirror dish, the telescopes are not protected by any dome. Therefore, a high resistance of the individual components against the environmental conditions is required. The mount is alt-azimuthal, two motors move the structure on the rail for a range of 450° in azimuth.
Another motor allows movements of the reflective dish and the camera between $-80°$ and 105° in zenith. The telescopes can be oriented in less than 40 s to point to any sky direction although each one weighs around 60 tons. The movements of the entire structure and the properties of the reflector and the camera are controlled by a set of computers situated in the so-called counting house (CH), a building placed close to the telescopes. This is also the site where all the electronic devices are stored and where the digital signal from the cameras is sent via fiber optics.
The reflective surface of the mirrors has an octagonal parabolic shape that is tessellated

with spherical mirrors with a radius of curvature between $\simeq 33.9$ and $\simeq 36.4$ m, depending on their position on the paraboloid. The M1 reflector is composed by 956 aluminum mirrors of roughly 0.5×0.5 m^2 surface grouped in panels of four facets, while the M2 reflector is composed by 143 aluminum mirrors of $\simeq 1$m^2 surface in the center and 104 glass mirrors of $\simeq 1$m^2 surface in the outer region. The external face of each mirror has to be coated with a thin layer of quartz (with some admixture of carbon) around 100 nm thick. This is needed to protect the mirrors against corrosion and acid rain. The diameter of each reflector is $D = 17$ m, corresponding to a total reflecting surface of roughly 236m^2. To minimize the aberrations related to a parabolic dish, the focal distance of the MAGIC telescopes is $f = 17$ m, which leads to a focal-to-diameter ratio of $f/D = 1$ [12]. The parabolic shape guarantees the preservation of the temporal structure of the atmospheric showers.
The aim in the construction of IACT cameras is to contain as much Cherenkov light of a shower as possible and to obtain images with high resolution. It is necessary to reach a good compromise between these two properties, due to technical and economic problems in constructing wide cameras with very high resolution. This is achieved by a design of the cameras with an angular field of view (FoV) of 3.5° and 1039 pixels of 0.1° FoV. The camera of M2 weights approximately 750 kg and the new camera of M1 (installed in 2012) roughly 780 kg. Both cameras are held in the focal plane of the mirror dish by a metallic arch supported by thin steel cables. Each camera is protected from daylight by two metallic lids that are opened during the data taking.
In addition, there are water and air systems for cooling and heating which regulate the temperature in the camera, preventing it from freezing or getting too hot and reaching the dew point. Each pixel collects the incoming light by a photomultiplier tube (PMT) of high quantum efficiency, which provides a fast response of the order of 1 ns [13]. The voltage at which the PMTs are operated is individually adjustable between 0 and 1500 V, such that if there is a star in the FoV the illuminated pixels can be switched off. The PMTs have six dynodes and a gain of around 3×10^4, which is rather low and allows observations with moderate moonlight.

1.7.1 The Hillas parameters

The image recorded by the camera is parameterized with a set of parameters first defined by Hillas [14]. They represent the basis on which the shower reconstruction is performed. The principal Hillas parameters that can be seen in Figure 1.12, are:

- **size**: the sum of the number of photons in the image. At fixed zenith angle of observation this parameter is in first approximation proportional to the primary particle energy;

- **alpha**: the angle between the major ellipse axis and a line from the center of the ellipse to the center of the camera. Shower images induced by primary gammas feature an alpha close to zero due to their preferential direction, while hadron-induced shower images exhibit a random distribution of this parameter since their direction is

nearly isotropic. In the case of point like sources, alpha represents the most powerful discriminator of γ-like events;

- **dist**: the distance from the center of the ellipse to the center of the camera. It provides information on the distance of the shower maximum and the impact parameter;
- **length**: the major semi-axis of the ellipse. It is related to the longitudinal development of the shower;
- **width**: the minor semi-axis of the ellipse. It is correlated with the transverse development of the shower and provides a good way to suppress the background because the hadronic showers are transversely larger.

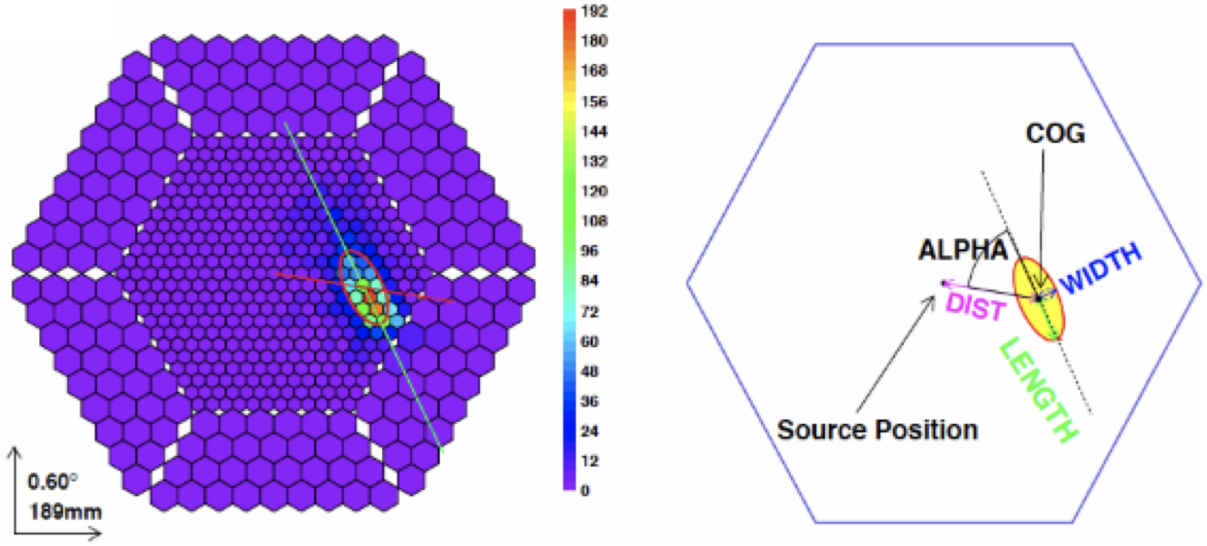

Figure 1.12: The Hillas parameters (right) of a real shower image (left), with the position of the γ-ray source and the center of gravity of the parameterized ellipse.

1.7.2 Typical measures taken with MAGIC telescopes

With the MAGIC telescopes important scientific data can be taken, because of its good position and sensitivity.
Two mainly important physics measures can be obtained, and they are the Lightcurve and the Spectrum. The first one can be obtained with Time values and with the Flux unit; dates are usually given in **M**odified **J**ulian **D**ate (MJD), while the Flux unit, which is the astrophysical γ-ray Flux normally provided in scientific publications, is usually given in TeV cm^{-2} s^{-1}.
The Spectrum instead can be obtained with Energy values, usually given in **G**iga **e**lettron**V**olt (GeV), which means 10^9 eV, and the Flux unit, usually given as said in TeV cm^{-2} s^{-1}.

Chapter 2

Analysis of MAGIC catalog FITS files

2.1 Check of the FITS files content

Considering that the main goal of this thesis was to investigate a class of objects observed with the MAGIC telescope, I started by reviewing the source catalog files that the MAGIC collaboration has made accessible in a publicly available online site. These are released in FITS [21] format, which is the **F**lexible **I**mage **T**ransport **S**ystem. It was originally developed in the late 1970s to create a common format to facilitate the image interchange between observatories, hence overcoming incompatibilities between the numerous operating systems. It was standardized in 1980 and recommended as a standard format by the International Astronomical Union (IAU) in 1982 and formally endorsed since 1988. In the mid-1990s the NASA high energy astrophysics science archive research center (*HEASARC*) FITS Working Group, promoted multi-mission standards for the format of FITS data files in high-energy astrophysics and produced a number of documents and recommendations that were subsequently incorporated into the FITS standard format definition.
Since its conception, the FITS format has been been updated regularly to address new types of *metadata* conventions, the diversity of research projects and data product types. Today the FITS format is in widespread use among astronomers of all observing bands, from radio frequencies to γ rays [20], [22].
Although the FITS is a standard astronomic format, the MAGIC collaboration adopted it only in recent times, and only to release data to the general scientific public. These release data cannot be properly considered a *catalog* of sources in the sense that the analysis is not homogeneous among sources but tailored source by source. In this sense, the MAGIC one is more properly a list of observed sources. As an example: there is no homogeneous definition of 'centroid' of the source, and the position of the specific object is often likely taken from the literature. The production of a proper catalog is under discussion within the collaboration.

From the FITS catalog, freely available in a public repository[1] I have generated a reader

[1] http://vobs.magic.pic.es/fits/

script using the Python code (reported in App. A), and extracted the relevant parameters for further use in this work.

- **Target name**: name of the source/sources analyzed in the file.
- **Reference**: name of the corresponding published paper.
- **Publication Year**: year of the publication of the paper.
- **Lightcurve**: Number of lightcurves that can be found in the file.
- **Spectrum**: Number of spectra that can be found in the file.

In addition to these fields, the FITS contains further data such as the so-called θ^2 or α plots that are standard plots to show the significance of the detection, as well as skymaps. All these are not used in this thesis, however, they are extracted through the custom script I made. Considering the FITS format was only recently used by the MAGIC collaboration, as already mentioned, I run a careful cross-check between the information reported in the FITS file and the corresponding published paper, in order to provide a well-tested sample of data. We cross-checked all parameters: source name, location, spectral points and uncertainties, lightcurve points and uncertainties, and so on. As a main result of this step, I generated a report together with my supervisor that will be sent to the FITS manager in the MAGIC collaboration to correct the mistakes found.

In a second step, I performed some basic classification of the FITS file at hand that overall comprised 36 valid files.

- **Classification of the object**: we have defined classes of objects, like BL Lacs, FSRQs, radio-galaxies, supernova remnants, and others, and we classified every source with a specific class.
- **Location**: where the source is located, if it is Galactic or Extragalactic.
- **Type of observations**: if the observation has been made in mono or stereo mode. Since the MAGIC telescope is composed by two different telescopes, a Stereo observation refers to an observation made with all of them, while a Mono one, to an observation made with only one of them.
- **Presence in further renowned catalogs**: the catalogs checked are TeVCat and TeGeV.

In the available MAGIC FITS catalog there are: 49 extragalactic sources out of which 23 are BL Lacs objects (further classified as 17 HBLs, 2 IBL/HBLs, 3 LBL/IBLs and 1 LBL), 10 are Flat Spectrum Radio Quasars (FSRQ), 9 are Radio Galaxies, 2 are clusters of galaxies and 2 are Gamma Ray Bursts. Galactic sources are instead 26, out of which 9 are X-ray binaries, 7 are Supernova remnants, 5 are Pulsars, while the other publications

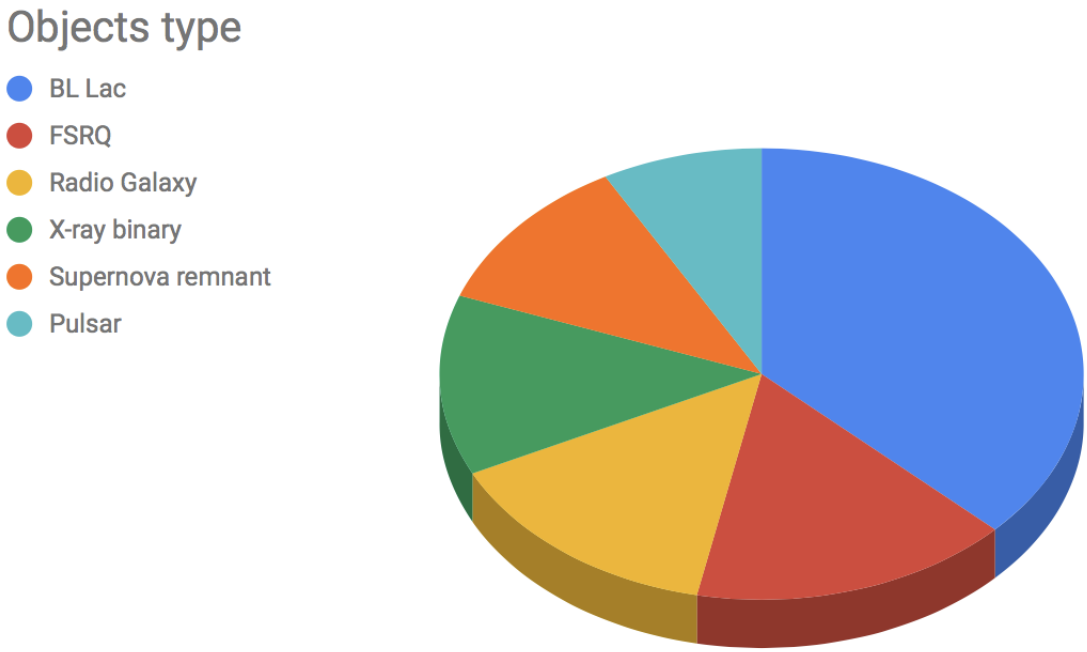

Figure 2.1: Pie chart showing the types of sources we had, after checking the FITS files.

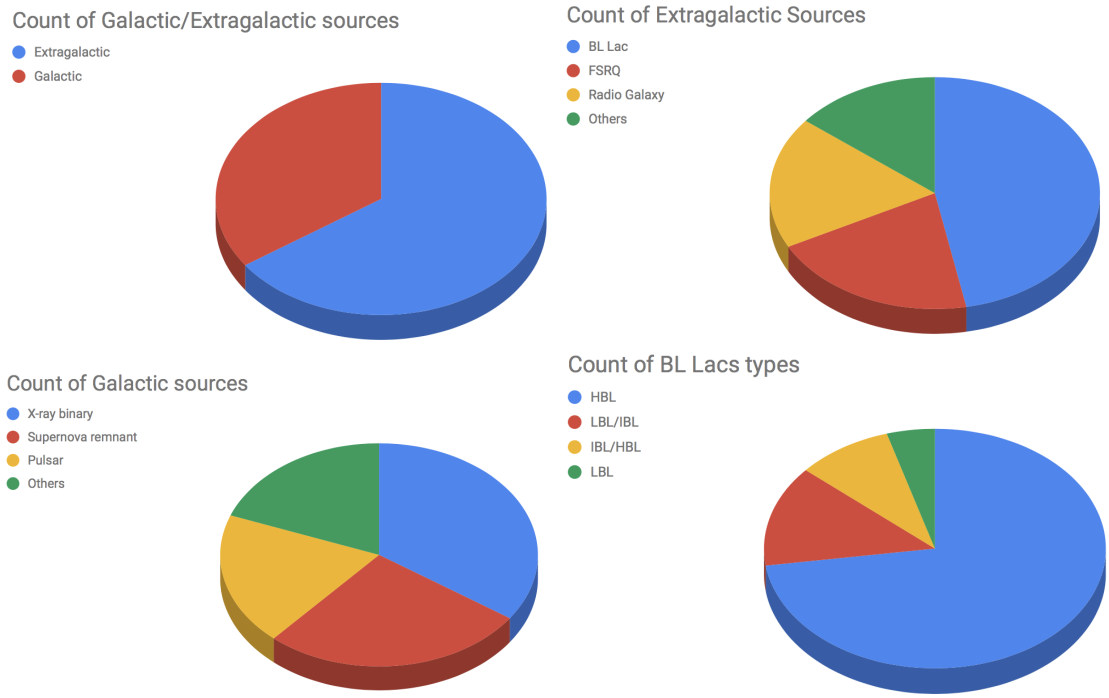

Figure 2.2: Distribution of sources and source classes within the MAGIC FITS catalog investigated in this work.

dealt with globular clusters, novae and supernovae and the galactic center. Additional 3 are dark matter targets. The pie chart in Figure 2.1 shows the resulting distribution of the observed sources, those in Figure 2.2 show the further subdivisions.

We focused our attention on the BL Lac object, because they are the wider class of MAGIC targets. Accordingly, other information have been added in the catalog for this type of sources:

- **Subclass type**: subclass of BL Lac source: HBL, IBL, LBL and the medium cases, like HBL/IBL and IBL/LBL.
- **Coordinates**: right ascension and declination of the source.
- **Distance**: redshift of the source.
- **Time of observation**: in MJD (modified julian date), and converted in MET (mission elapsed time) for the Fermi analysis we wanted to do.

In Table 2.1 our 17 BL Lacertae sources are listed, with their main information, including their corresponding paper, their Type and their redshift.

Source name	Journal reference	Type	Redshift
Markarian180	J. Albert et al., ApJ Lett. 648, L105	HBL	0.045
1ES1011+496	J. Albert et al., ApJ Lett. 667, L21	HBL	0.212
Markarian421	J. Albert et al., ApJ Lett. 663, L125	HBL	0.031
1ES1959+650	G. Tagliaferri et al., ApJ 679, 1029	HBL	0.047
Markarian421	V. A. Acciari et al., ApJ 703, 169	HBL	0.031
S50716+714	H. Anderhub et al., ApJ Lett. 704, L129	LBL/IBL	0.26
Markarian421	J. Aleksic et al., A&A 519, A32	HBL	0.031
PG1553+113	J. Aleksic et al., A&A 515, A76	HBL	0.3
1ES1215+303	J. Aleksic et al., A&A 544, 142	IBL/HBL	0.131
B32247+381	J. Aleksic et al., A&A 539, 118	HBL	0.1187
PKS2155-304	J. Aleksic et al., A&A 544, 75	HBL	0.116
1ES2344+514	J. Aleksic et al., A&A 556, A67	HBL	0.044
PKS1424+240	J. Aleksic et al., A&A 567, A135	HBL	0.6
1ES0806+524	J. Aleksic et al., MNRAS 451, 5258-5269	IBL/HBL	0.138
H1722+119	M. L. Ahnen et al., MNRAS 459, 3271-3281	HBL	0.4
S20109+22	S. Ansoldi et al., MNRAS 480, 879	LBL/IBL	0.35
S40954+65	2018arXiv180104138M	LBL	0.368

Table 2.1: Our 17 BL Lacs sources we studied. Columns indicate the name of the source, the corresponding paper, their BL Lac type and their redshift.

2.2 Analysis of the FITS files content

In order to investigate the content of the FITS file, I developed a custom `Python` script that accessed the file and extracted the information of interest:

- Getting information about what the file contains: these can be found in the `Primary Header` of a FITS file, and here I found that five main types of data can be seen in these FITS files: data about the lightcurves, about Spectra, about Skymaps, about θ^2 plots and about α plots. Different fits file may contain more or less of this main products: for example, multiple spectra can be reported in case the publication contained more of them. A lightcurve could be missing if it was missing in the corresponding paper, and so on. In Figure 2.3 an example of these information can be seen.

```
No.    Name         Ver    Type        Cards   Dimensions   Format
  0  PRIMARY        1 PrimaryHDU       19   ()
  1  LIGHTCURVE     1 BinTableHDU      22   8R x 3C   [1D, 1D, 1D]
  2  LIGHTCURVE_1     1 BinTableHDU      22   3R x 3C   [1D, 1D, 1D]
  3  ALPHAPLOT      1 BinTableHDU      24   45R x 4C   [1D, 1D, 1D, 1D]
  4  SPECTRUM       1 BinTableHDU      22   3R x 3C   [1D, 1D, 1D]
  5  SPECTRUM_1     1 BinTableHDU      22   3R x 3C   [1D, 1D, 1D]
```

Figure 2.3: An example of the contents of the `primary header` of a FITS file. In this example it can be seen that the file contains two lightcurves, two Spectra and an α plot.

  In addition to the contents of the files, the script gives general information about the FITS file, like the name of the source, the mono or stereo observation, the coordinates of the source, the date of the observation and other various information, like some comments made by the authors, as can be seen in Figure 2.4.

- Plotting the lightcurves contained in the file. Data that can be obtained from the file are the **M**odified **J**ulian **Date** (MJD) that is the time unit and the Flux unit given for the most of the cases in TeV $\mathrm{cm}^{-2}\,\mathrm{s}^{-1}$, with its uncertainties. Figure 2.5 (left part) shows an example of a plot generated by my python script to extract a lightcurve.

- Plotting the Spectra contained in the file. Data that can be obtained from the file are the Energy unit, given in GeV and the Flux unit, given in $\mathrm{TeV\,cm}^{-2}\mathrm{s}^{-1}$, together with experimental uncertainties. Figure 2.5 (right) shows an exemplary spectral energy distribution.

- Computing the photon index of the Spectrum assuming a simple power-law fit.

```
SIMPLE  =                    T / file does conform to FITS standard
BITPIX  =                  -32 / number of bits per data pixel
NAXIS   =                    0 / number of data axes
EXTEND  =                    T / FITS dataset may contain extensions
COMMENT   FITS (Flexible Image Transport System) format is defined in 'Astronomy
COMMENT   and Astrophysics', volume 376, page 359; bibcode: 2001A&A...376..359H
DATE    = '2011-03-03T11:24:51' / Date/time of file generation (UTC)
ORIGIN  = 'MAGIC    '           / Organization responsible
AUTHOR  = 'MAGIC Coll.'         / Author of the results
TELESCOP= 'MAGIC-I '            / Telescope used in the observations
VERSION = '0.2      '           / Current version of the fits file
OBJECT  = 'S5 0716+714'         / Observed source
SRCPOS1 =              110.472 / Position of the observed object along the x-axi
SRCPOS2 =              71.3434 / Position of the observed object along the y-axi
REFPAPER= 'H. Anderhub et al., ApJ Lett. 704 (2009), L129-L133 ' / Paper where r
COMMENT This is a prototype of MAGIC fits file containig the result of the obser
COMMENT vations of S5 0716+714. Please conside it as VERY PRELIMINAR
COMMENT The latest version of this data file and of the document explaining its
COMMENT content can be found at http://magic.pic.es/pub/fits.
```

Figure 2.4: General information about the FITS file and the sources observed. Comments of authors can also be seen.

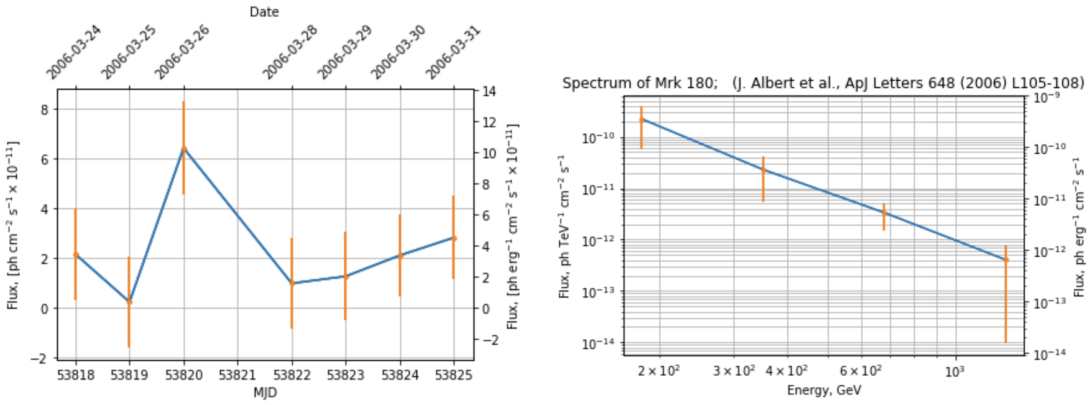

Figure 2.5: (left)Example of the final plot of the lightcurve obtained from the data contained in the FITS file. (right) Example of the final plot of the Spectrum obtained from the data contained in the FITS file

2.3 List of BL Lac objects analyzed in this work

In order to try a population study, we focused on the most numerous class of similar objects, that of Bl Lacs. For these targets, we got additional information to characterize them in a better way. Here is a list of the sources we analyzed with their principal properties.

2.3.1 Markarian 421

For this source we had three files, because it has been observed by MAGIC multiple times. The first observation is taken from the paper 'MAGIC TeV Gamma-Ray Observations of

Markarian 421 during Multiwavelength Campaigns in 2006', by J. Aleksic et al published in 2010 [26]. The source is a HBL type, it has coordinates 166.113920 in RA and 38.209000 in DEC, and has a redshift z=0.031. The file contained 2 lightcurves and 9 spectra, but there was a problem with the spectra; in fact there was a mismatch between the data in the FITS file and the spectra reported in the paper. The problem has been reported. In Figure 2.6 the lightcurve and the spectrum generated with the `Python` code can be seen. In the corresponding paper there was no SED of the source, so we referred to the paper of our collaborator Andrea Tramacere [25] to get it.

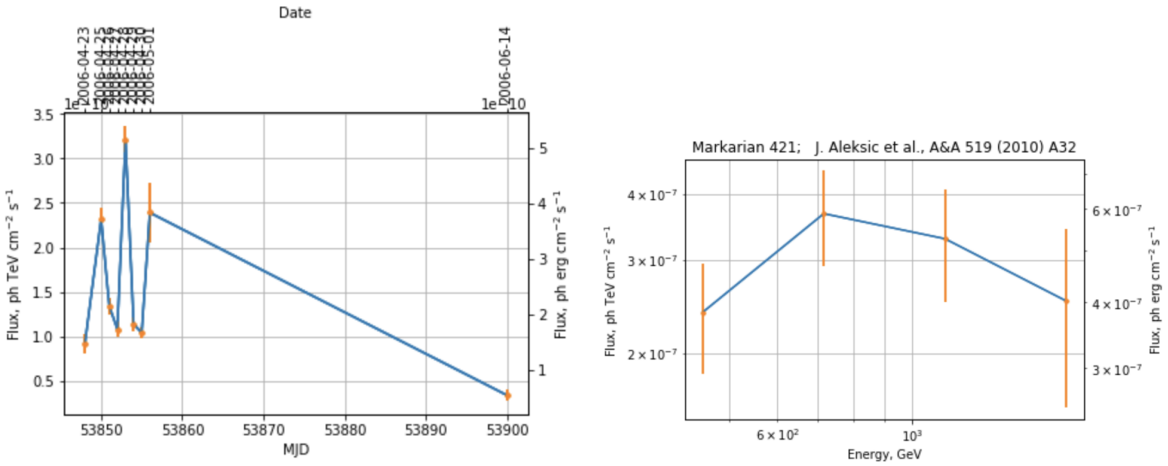

Figure 2.6: Lightcurve and spectrum generated with the `Python` of the source Mkn421.

The second observation is taken from the paper 'Observations of Mkn 421 with the MAGIC Telescope', by J. Albert et al published in 2007 [27]. The file contained 13 lightcurves, 2 spectra, 1 θ^2 plot and 1 α plot. In Figure 2.7 the lightcurve and the spectrum generated with the `Python` code can be seen.

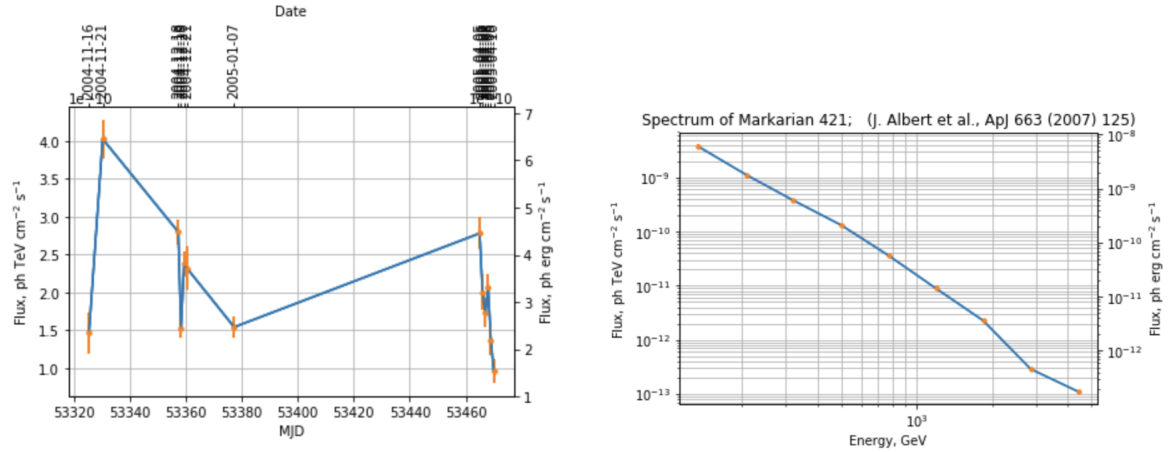

Figure 2.7: Lightcurve and spectrum generated with the `Python` of the source Mkn421.

The third observation is taken from the paper 'Simultaneous Multiwavelength Observations of Markarian 421 During Outburst', by V. A. Acciari et al published in 2009 [28]. The file contained 1 lightcurve and 1 spectrum. In Figure 2.8 the lightcurve and the spectrum generated with the `Python` code can be seen. It is important to remark that this observation has been made during a very bright outburst of the source, and because of this, data will be affected in an important way. As we will see, the difference in flux of this observation and other observations of the same source, will be very marked.

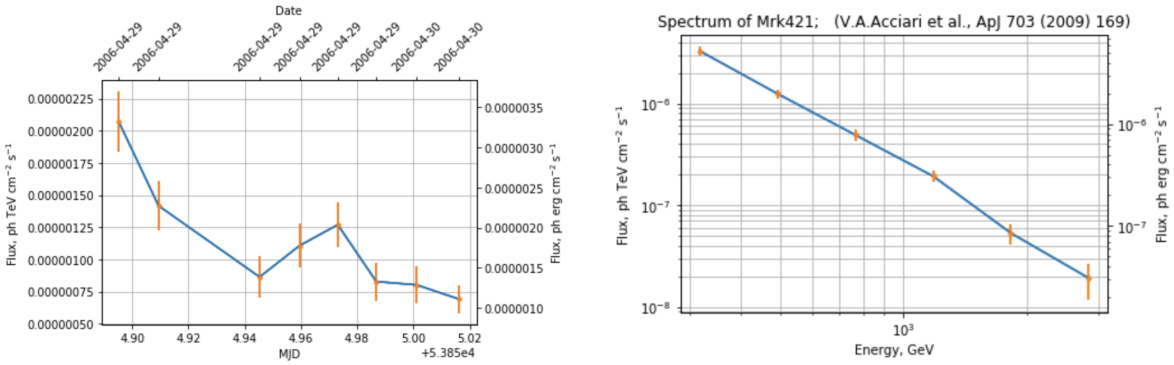

Figure 2.8: Lightcurve and spectrum generated with the `Python` of the source Mkn421.

2.3.2 Markarian 180

The observation is taken from the paper 'Discovery of Very High Energy Gamma-rays from Markarian 180 triggered by an optical outburst', by J. Albert et al published in 2006 [29]. The source is a HBL type, it has coordinates 174.110040 in RA and 70.157280 in DEC, and has a redshift z=0.045. The file contained 1 lightcurve, 2 spectra and 1 θ^2 plot. In Figure 2.9 the lightcurve and the spectrum generated with the `Python` code can be seen. Also this source has been taken during an outburst, affecting the data.

2.3.3 1ES1011+496

The observation is taken from the paper 'Discovery of Very high energy gamma-rays from 1ES1011+496 at z=0.212', by J. Albert et al published in 2007 [30]. The source is a HBL type, it has coordinates 153.767083 in RA and 49.433611 in DEC, and has a redshift z=0.212. The file contained 2 lightcurves, 2 spectra and 1 θ^2 plot. In Figure 2.10 the lightcurve and the spectrum generated with the `Python` code can be seen.

2.3.4 1ES1959+650

The observation is taken from the paper 'Simultaneous multiwavelength observations of the blazar 1ES1959+650 at a low TeV flux', by G. Tagliaferri et al published in 2008 [31]. The source is a HBL type, it has coordinates 299.999583 in RA and 65.148611 in DEC,

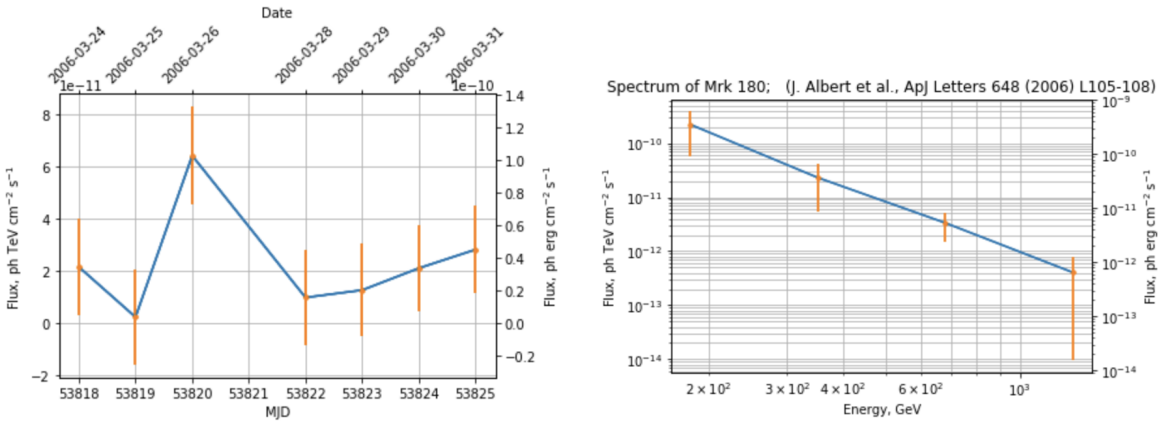

Figure 2.9: Lightcurve and spectrum generated with the `Python` of the source Mkn180.

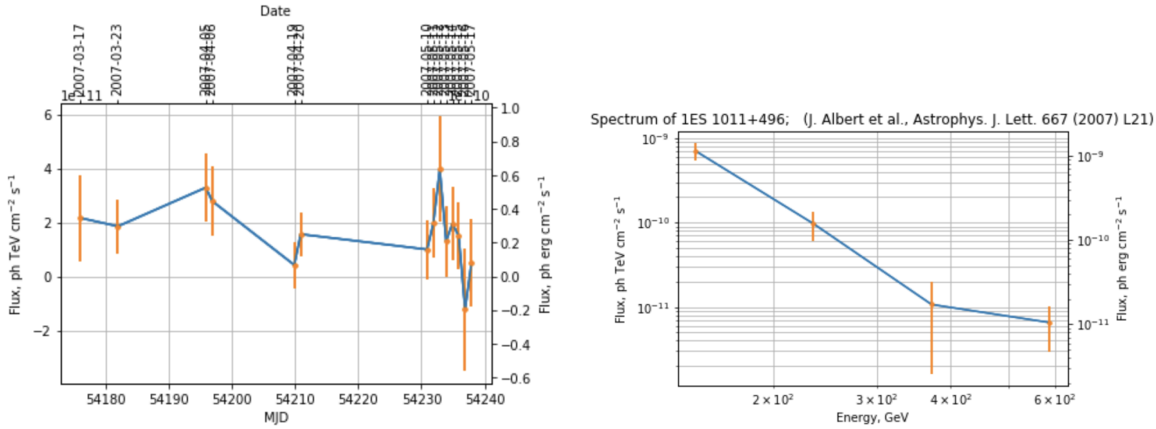

Figure 2.10: Lightcurve and spectrum generated with the `Python` of the source 1ES1011+496.

and has a redshift z=0.048. The file contained 1 lightcurve and 1 spectrum. In Figure 2.11 the lightcurve and the spectrum generated with the `Python` code can be seen.

2.3.5 S50716+714

The observation is taken from the paper 'Discovery of Very High Energy gamma-rays from the Blazar S50716+714', by H. Anderhub et al published in 2009 [32]. The source is a LBL/IBL type, it has coordinates 110.472500 in RA and 71.343333 in DEC, and has a redshift z=0.26. The file contained 2 lightcurves, 2 spectra and 1 α plot. In Figure 2.12 the lightcurve and the spectrum generated with the `Python` code can be seen. In the paper, authors suggest that this source could have an external Compton emission that would be responsible for the very high peak of high energy, as we will see in our final results.

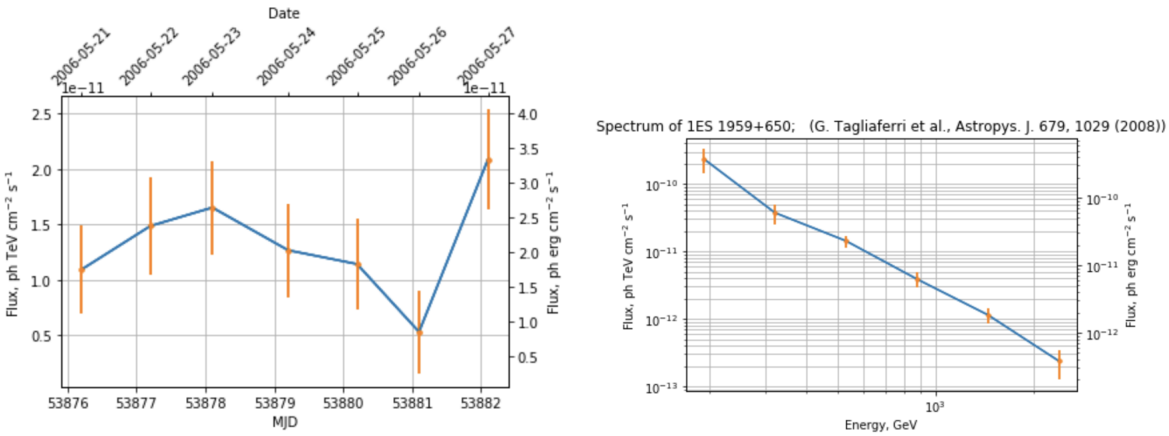

Figure 2.11: Lightcurve and spectrum generated with the `Python` of the source 1ES1959+650.

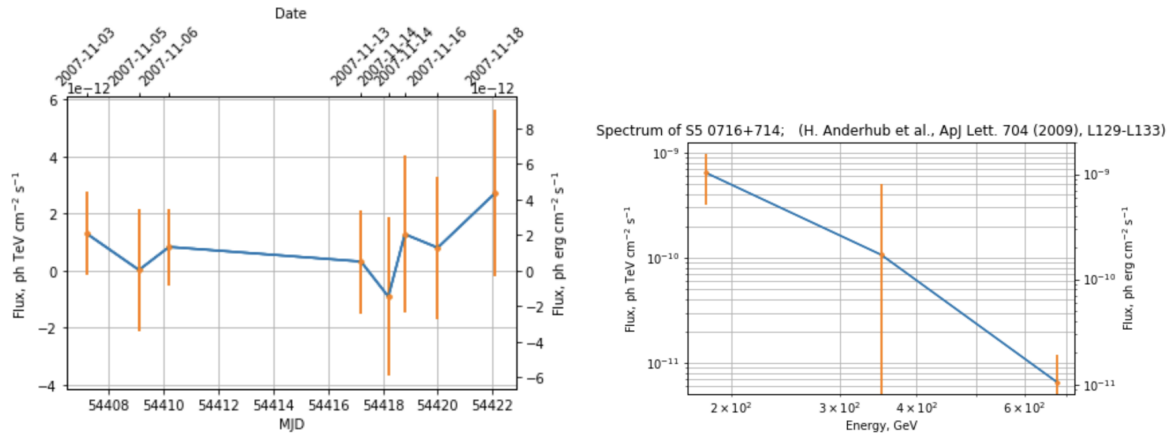

Figure 2.12: Lightcurve and spectrum generated with the `Python` of the source S50716+714.

2.3.6 PG1553+113

The observation is taken from the paper 'Simultaneous multi-frequency observation of the unknown redshift Blazar PG 1553+113 in March-April 2008', by J. Aleksic et al published in 2010 [33]. The source is a HBL type, it has coordinates 238.930000 in RA and 11.189167 in DEC, and has a redshift z=0.3. The file contained 1 spectrum. In Figure 2.13 the spectrum can be seen.

2.3.7 1ES1215+303

The observation is taken from the paper 'Discovery of VHE -rays from the Blazar 1ES 1215+303 with the MAGIC Telescopes and simultaneous multiwavelength observations', by J. Aleksic et al published in 2012 [34]. The source is a IBL/HBL type, it has coordinates

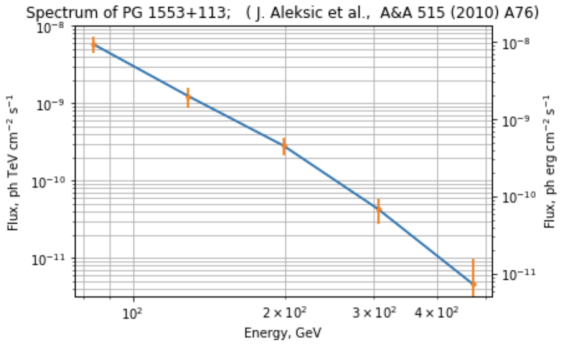

Figure 2.13: Spectrum generated with the `Python` of the source PG1553+113.

184.467083 in RA and 30.116944 in DEC, and has a redshift z=0.131. The file contained 1 lightcurve, 2 spectra and 3 θ^2 plot. In Figure 2.14 the lightcurve and the spectrum generated with the `Python` code can be seen.

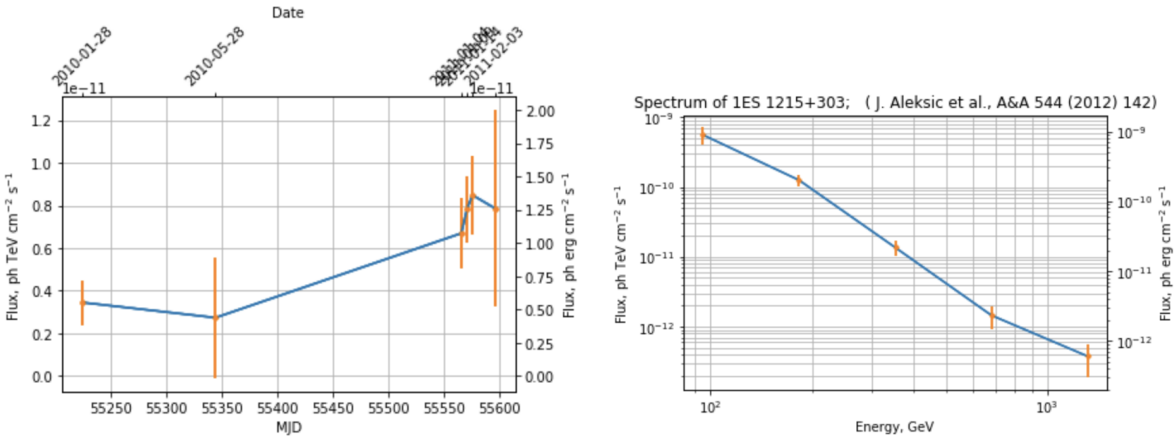

Figure 2.14: Lightcurve and spectrum generated with the `Python` of the source 1ES1215+303.

2.3.8 B32247+381

The observation is taken from the paper 'Discovery of VHE gamma-ray emission from the BL Lac object B3 2247+381 with the MAGIC telescopes', by J. Aleksic et al published in 2012 [35]. The source is a HBL type, it has coordinates 342.523333 in RA and 38.410556 in DEC, and has a redshift z=0.1187. The file contained 1 lightcurve, 2 spectra and 1 θ^2 plot. In Figure 2.15 the lightcurve and the spectrum generated with the `Python` code can be seen.

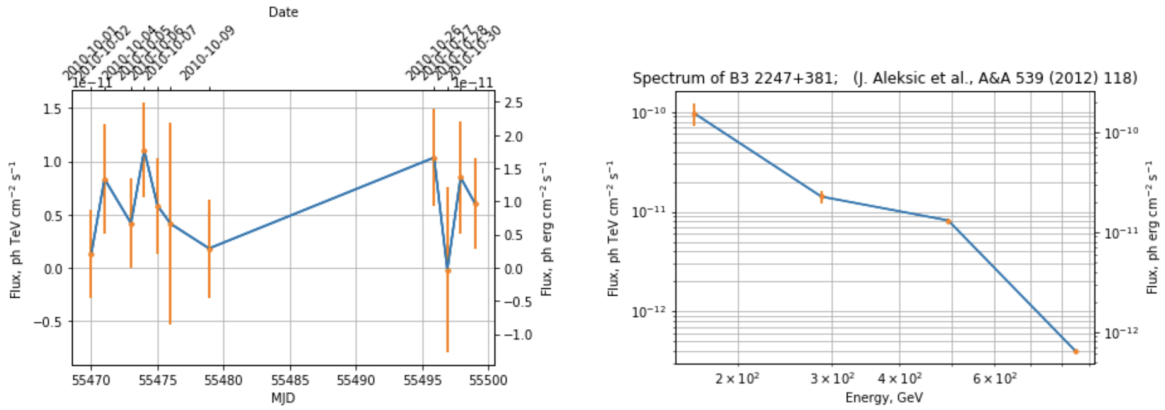

Figure 2.15: Lightcurve and spectrum generated with the `Python` of the source B32247+381.

2.3.9 PKS2155-304

The observation is taken from the paper 'High zenith angle observations of PKS 2155-304 with the MAGIC-I Telescope', by J. Aleksic et al published in 2012 [36]. The source is a HBL type, it has coordinates 329.716095 in RA and -30.224923 in DEC, and has a redshift z=0.116. The file contained 2 spectra and 2 θ^2 plots. In Figure 2.16 the spectrum generated with the `Python` code can be seen. The observation has been made during an outburst, and because of this the resulting flux is higher than normal, as seen in the next section.

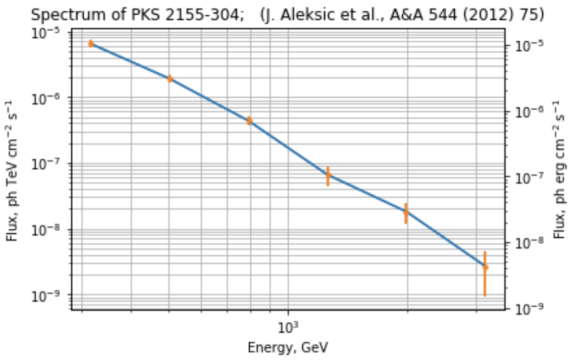

Figure 2.16: Spectrum generated with the `Python` of the source PKS2155-304.

2.3.10 1ES2344+514

The observation is taken from the paper 'The simultaneous low state spectral energy distribution of 1ES 2344+514 from radio to very high energies', by J. Aleksic et al published in 2013 [37]. The source is a HBL type, it has coordinates 356.770000 in RA and 51.705000

in DEC, and has a redshift z=0.044. The file contained 2 lightcurves and 4 spectra. In Figure 2.17 the lightcurve and the spectrum generated with the `Python` code can be seen.

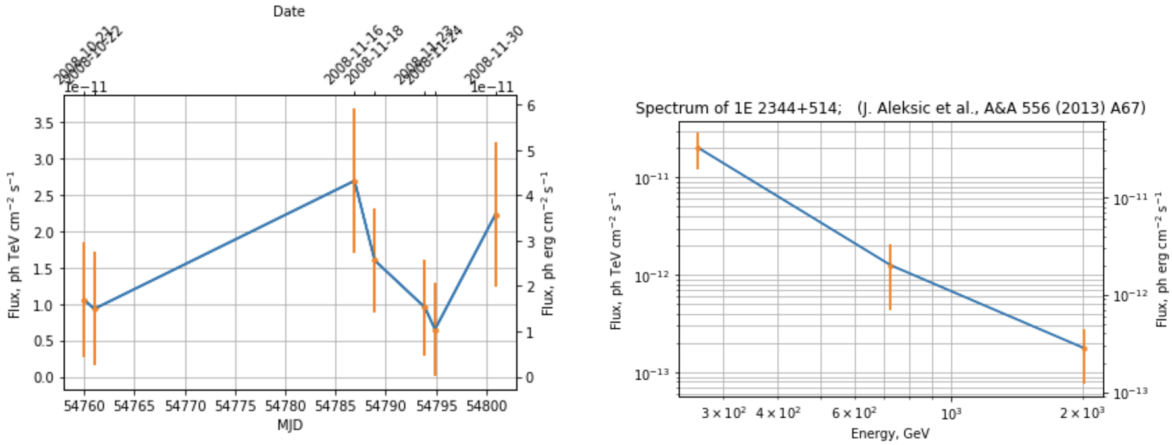

Figure 2.17: Lightcurve and spectrum generated with the `Python` of the source 1ES2344+514.

2.3.11 PKS1424+240

The observation is taken from the paper 'MAGIC long-term study of the distant TeV Blazar PKS 1424+240 in a multiwavelength context', by J. Aleksic et al published in 2014 [38]. The source is a HBL type, it has coordinates 216.752083 in RA and 23.800000 in DEC, and has a redshift z=0.6. The file contained 3 lightcurves and 4 spectra. In Figure 2.18 the lightcurve and the spectrum generated with the `Python` code can be seen.

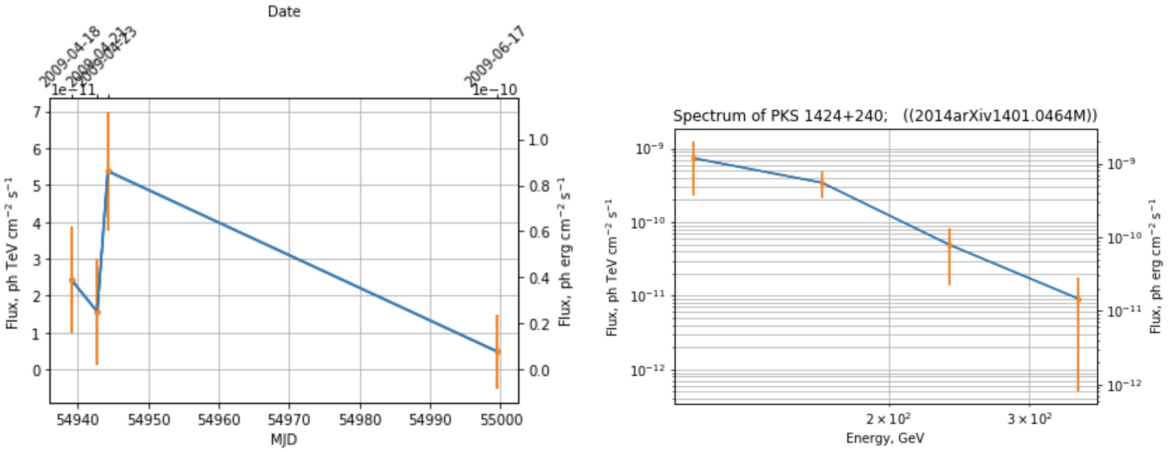

Figure 2.18: Lightcurve and spectrum generated with the `Python` of the source PKS1424+240.

2.3.12 1ES0806+524

The observation is taken from the paper 'MAGIC detection of short-term variability of the high-peaked BL Lac object 1ES 0806+524', by J. Aleksic et al published in 2015 [39]. The source is a IBL/HBL type, it has coordinates 122.455000 in RA and 52.316111 in DEC, and has a redshift z=0.138. The file contained 2 lightcurves, 4 spectra and 1 θ^2 plot. In Figure 2.19 the lightcurve and the spectrum generated with the `Python` code can be seen. The corresponding paper contains two SEDs of the source, one in high state, and one in low state, and so we decided to treat them as separated SEDs.

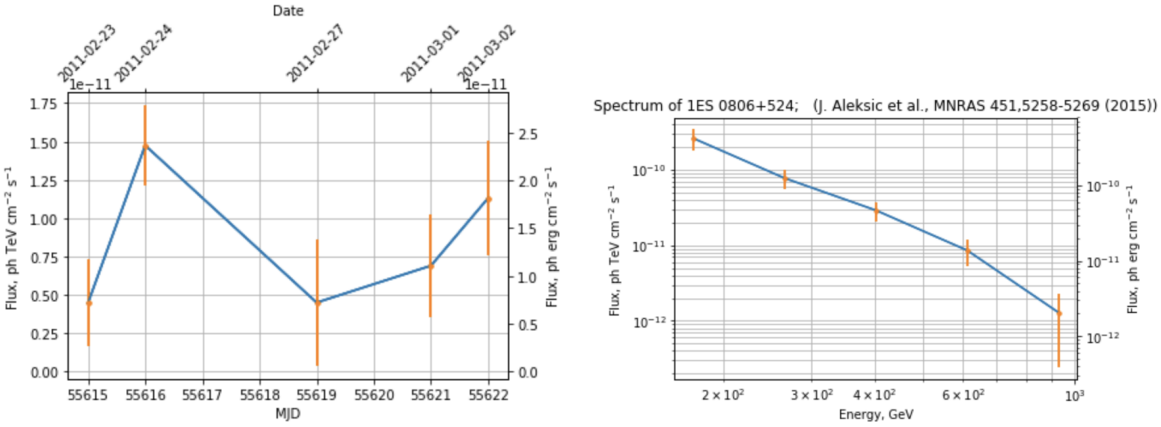

Figure 2.19: Lightcurve and spectrum generated with the `Python` of the source 1ES0806+524.

2.3.13 H1722+119

The observation is taken from the paper 'Investigating the peculiar emission from the new VHE gamma-ray source H1722+119', by M. L. Ahnen et al published in 2016 [40]. The source is a HBL type, it has coordinates 261.268333 in RA and 11.871111 in DEC, and has a redshift z=0.4. The file contained 2 lightcurves, 2 spectra and 1 θ^2 plot. In Figure 2.20 the lightcurve and the spectrum generated with the `Python` code can be seen. In the corresponding paper the authors say that the source had a host galaxy, and because of this our analysis of the later sections will be affected.

2.3.14 S20109+22

The observation is taken from the paper 'The broad-band properties of the intermediate synchrotron peaked BL Lac S2 0109+22 from radio to VHE gamma rays', by S. Ansoldi et al published in 2018 [41]. The source is a LBL/IBL type, it has coordinates 18.024167 in RA and 22.744167 in DEC, and has a redshift z=0.35. The file contained 2 lightcurves and 2 spectra. In Figure 2.21 the lightcurve and the spectrum generated with the `Python` code can be seen.

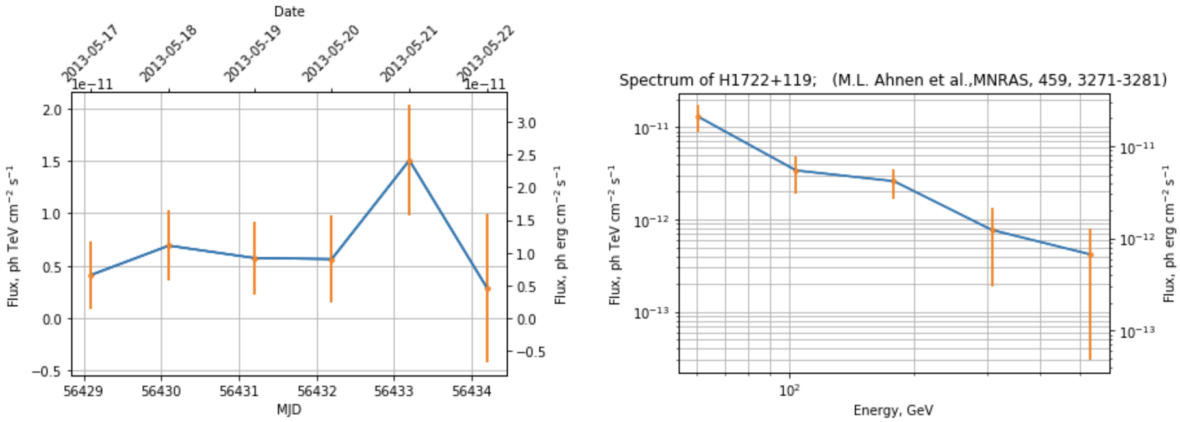

Figure 2.20: Lightcurve and spectrum generated with the `Python` of the source H1722+119.

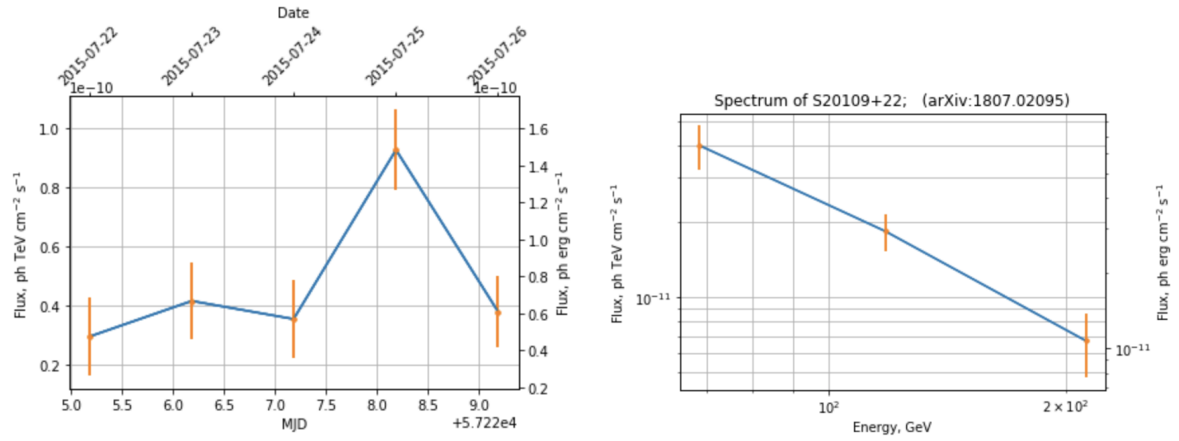

Figure 2.21: Lightcurve and spectrum generated with the `Python` of the source S20109+22.

2.3.15 S40954+65

The observation is taken from the paper 'The detection of the Blazar S4 0954+65 at very-high-energy with the MAGIC telescopes during an exceptionally high optical state', by M. L. Ahnen et al published in 2018 [42]. The source is a LBL type, it has coordinates 149.696667 in RA and 65.565000 in DEC, and has a redshift z=0.368. The file contained 2 lightcurves and 3 spectra. In Figure 2.22 the lightcurve and the spectrum generated with the `Python` code can be seen. The high energy peak of this source is the result of an external Compton process, that will influence our analysis of the later sections in a very consistent way.

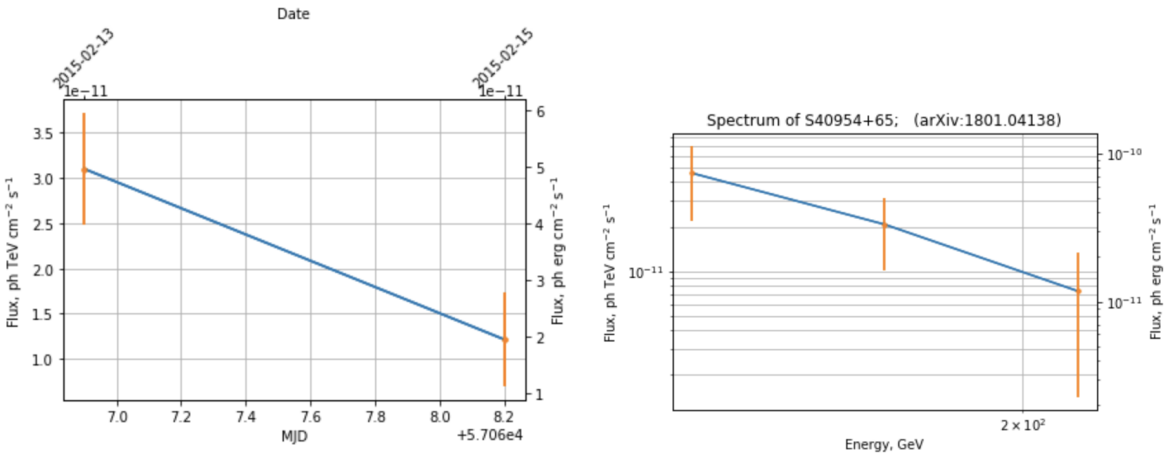

Figure 2.22: Lightcurve and spectrum generated with the `Python` of the source S40954+65.

Chapter 3

BL Lacertae objects

3.1 Overview

BL Lacertae (BL Lac) objects are a subclass of Blazars, which have specific properties and differences with the other Blazar category of Flat Spectrum Radio Quasars (FSRQs). In addition to the general information given in section 1.6.1, in this chapter more specific properties of this class of objects are reported, including their variability and their spectra [11].

BL Lac objects don't show prominent features in the optical spectrum and although their line emission is weak, BL Lacs seem in some cases to possess a narrow-line and a broad-line region as well. The fact that lines are usually not seen in their spectra is due to the dominance of the non-thermal continuum. For what concerns the variability of these objects, it is measured with the so called "Duty Cycle" [23], which is the fraction of time that these objects spend in a flaring state. It strongly depends on their overall spectral type.
A distinction between FSRQ and BL Lac as objects with and without broad lines can be defined more quantitatively focusing on the ratio between the observed luminosity and the Eddington luminosity (called *Eddington Ratio*). The Eddington luminosity is the maximum luminosity that can be emitted in an accretion process, and it is given by:

$$L_{Edd} = \frac{4\pi G M m_p c}{\sigma_t} \simeq 1.3 \times 10^{46} \left(\frac{M}{10^8 M_\odot} \right). \tag{3.1}$$

BL Lac objects show low Eddington ratios, with $L_{Balmer}/L_{Edd} < 5 \times 10^{-4}$, while objects that have a higher value for this ratio are considered to be FSRQ.
Based on modeling of the entire spectral energy distribution, one can derive further insight into the physical parameters of the emission region in Blazars. Ghisellini [24] describes the difference between FSRQ and BL Lac objects which have been detected in γ ray in terms of the following properties: the supermassive black hole mass $M_\odot$, the distance of the dissipation region in units of the Schwarzschild radius, $R_S = 2GM/c^2$, from the black

hole R_{diss}/R_S, the bulk Lorentz factor of the jet Γ, the magnetic field strength B, the accretion disk luminosity as derived from the emission lines L_{disk}, the Eddington ratio λ with respect to L_{disk}, the power injected by the relativistic electrons $P_e = \pi R^2 \Gamma^2 \beta c U_e$, where U_e is the energy density of the population of the injected electrons and R is the size of the emitting blob, and the total jet power, assuming that each electron is accompanied by a proton $P_{jet} = \dot{M}c^2$, where $\dot{M}$ is the mass accretion rate. Tab. 3.1 summarizes the average physical properties of BL Lacs and FSRQs, derived from fitting their overall SED including the γ rays. It can be seen that although the black hole masses, the distance of the emission region from the black hole, and the speed of the jet as expressed in the bulk Lorentz factor are similar for FSRQ and BL Lacs, the applied magnetic field strength and accretion flow are lower in BL Lacs, resulting in the observed lower luminosities.

	$\log(M_{BH})$ $[M_\odot]$	R_{diss}/R_S	Γ	B [G]	$\log(L_{disk})$ [erg s^{-1}]	λ	$\log(P_e)$ [erg s^{-1}]	$\log(P_{jet})$ [erg s^{-1}]
BL Lacs	8-9	300-1000	10-20	0.1-2	42-44	$<$0.01	41-43	43.5-45
FSRQ	8-9.5	300-3000	10-16	1-10	44-46.5	$>$0.01	42.5-44	45-48

Table 3.1: Average physical properties of γ-ray Blazars as presented in the work of Ghisellini et al. (2010). The quantities are: R_{diss}/R_S = distance of dissipation region, where R_S is the Schwarzschild radius; M_{BH} = mass of the black hole in the center of the Blazar; Γ = Lorentz factor of the jet; B = magnetic field strength; L_{disk} = accretion disk luminosity, λ = Eddington ratio; P_e = power of relativistic electrons; P_{jet} = total jet power.

Another important feature of BL Lacs is their redshift determination. As compared to FSRQ with emission lines, the BL Lac objects with generally featureless spectra render redshift determination observationally challenging. In BL Lac objects, at distances where the host galaxy cannot be cleanly separated from the AGN core, it is often impossible to determine the spectrum of the host galaxy. Therefore, only few BL Lacs have measured redshifts beyond z=0.5. Apart from measuring the absorption lines of the host galaxy in order to determine the redshift, one can also use the apparent magnitude of the galaxy itself as an indicator of the distance. This method assumes that the host galaxies of BL Lac objects, which are mainly giant elliptical galaxies, are similar in size and brightness, and the relation is calibrated by using BL Lac objects with known redshifts [11].
In the last years a new method has been used, as suggested in the paper by Prandini et al [46]. This method constrains the distance of Blazars with unknown redshift using combined observations in the GeV and TeV regimes. They assumed that the VHE spectrum corrected for the absorption through the interaction with the Extragalactic Background Light can not be harder than the spectrum in the Fermi/LAT band. Starting from the observed VHE spectral data they derived the EBL-corrected spectra as a function of the redshift z and fit them with power laws to be compared with power law fits to the LAT data. This method has been applied to all TeV Blazars detected by LAT with known

distance and so they derived an empirical law describing the relation between the upper limits and the true redshifts that can be used to estimate the distance of unknown redshift Blazars.

In the next sections we will analyze the BL Lacertae sources taken from the FITS files we have checked. What we wanted to make with them was to start a population study of this class of objects, so we will characterize their SED and their two characteristic peaks, that of synchrotron and that of inverse Compton. Our analysis will be done for the 17 BL Lacs, but also for their subclasses and their redshift, and we will look for common spectral trends. The physical concepts we need now have been introduced and described in the chapter 4.3, while the source selection has been explained in chapter 4.

3.2 Preliminary checks to investigate the BL Lacertae population

The first thing was to look for a kind of common trend in the spectra of the 17 BL Lacs sample. We check if all of them behaves in a similar way, and how the spectral index varies. To do this, we took all the spectra taken from the FITS files and overlapped them in one plot. The result can be seen in Figure 3.1. During this process, we noticed that the spectrum of the source Mkn421 described in section 2.3.1 had an error on the order of magnitude of the flux, and so we decided to exclude it.
It is easy to see how most of the sources group around similar flux values, while two of them show higher fluxes: these latter are a Mkn421 observation and the PKS2155-304. The Mkn421 is the orange one, and it is the observation of this source made during an extremely bright outburst, that justifies the enormous flux reported in the plot. The second spectrum, the red one, is that of PKS2155-304 and it is also taken during a bright outburst, and because of this it has a so high flux.

In order to compute the spectral index, we made a linear fit with a power law function. In this way, depending on the slope of the fit function, the photon index has been calculated. In Figure 3.2 an example of the fit function can be seen.

The results of our analysis of the spectral indices can be seen in Figure 3.3. As we can see, the spectral indices are distributed in a range between -4.25 and -0.25, with a higher concentration at low values. The values agree with the very steep spectra seen in Figure 3.1. It should be underlined that these spectra are not deconvoluted with the effect of the absorption of the intrinsic spectra in the Extragalactic Background Light, which affects the spectra as a function of the energy and the distance of the source. However, the purpose here is only to show a first-glance comparison.

We also investigated the relation between the redshift and energy range (minimum and maximum energy achieved by the MAGIC telescope on that target). The result can be seen in Figure 3.4. It is possible to notice that the largest energy ranges of the sources

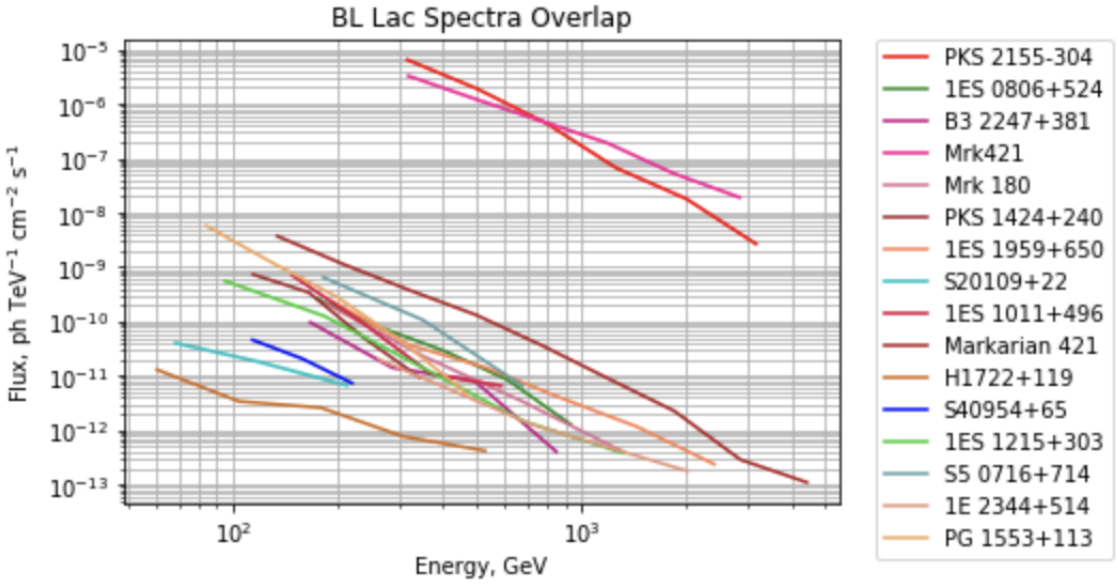

Figure 3.1: Spectra overlap of the 16 BL Lacs sources, taken from the FITS files. The two outliers are clearly visible.

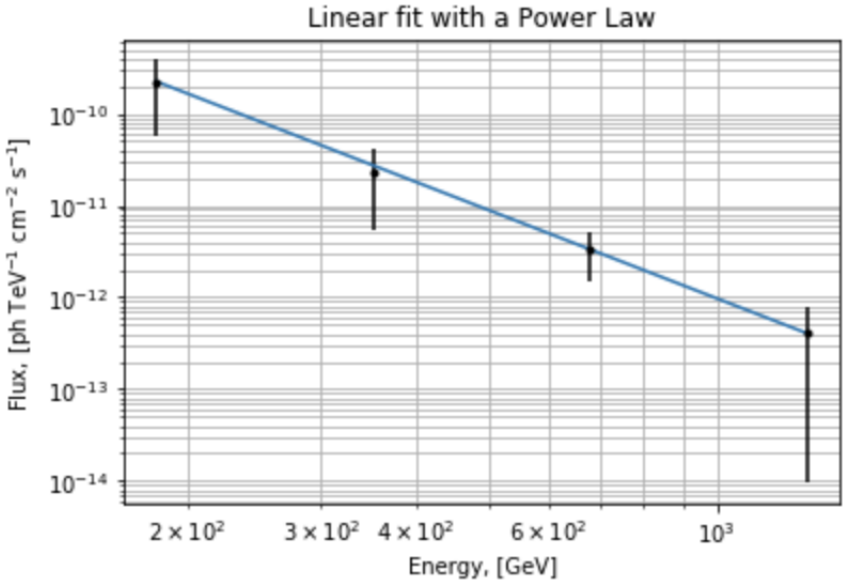

Figure 3.2: Example of the final plot of the linear fit with a power law function for the Spectrum obtained from the data contained in the FITS file.

are located at low redshifts, while if we look towards higher redshifts we can see that the energy ranges tend to be lower. This results in a more or less linear descending trend, meaning that the nearest sources are also the most energetic, but this is due to a bias effect caused by redshift. This is mostly related to the fact that farther sources are harder

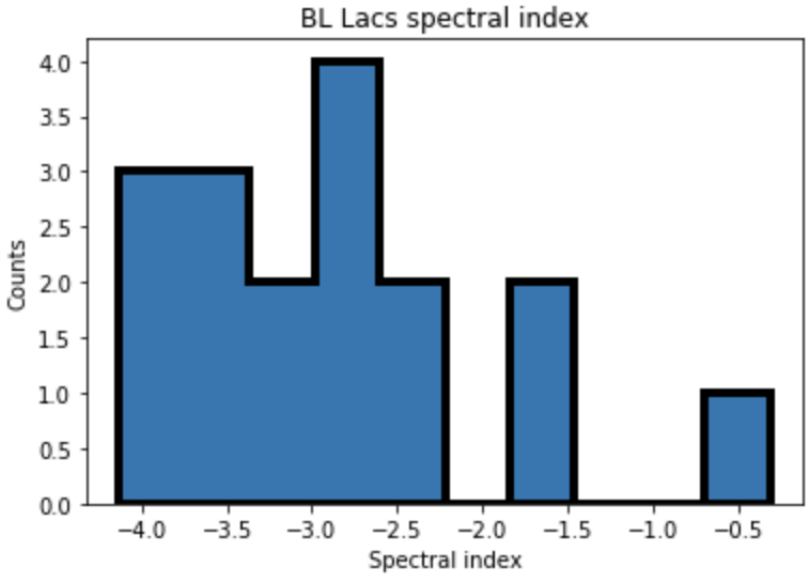

Figure 3.3: Histogram reporting the spectral indexes of our 17 sources.

to detect and therefore the photon statistics decrease, and with this the lower and higher reach of the sensitive region.
This plot will allow to better understand the results we will find in section 3.2.2.

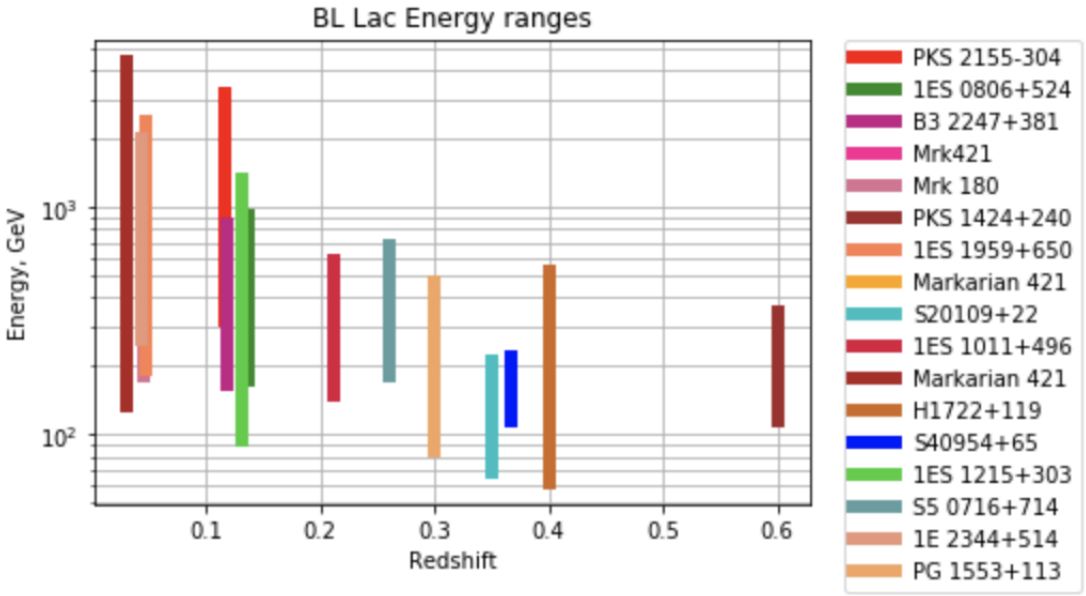

Figure 3.4: Plot showing redshift vs energy range of our 17 BL Lac sources. The linear descending trend is clearly visible.

3.2.1 SED study

We now move to a tentative population study of the BL Lacs sample at hand analyzing its **S**pectral **E**nergy **D**istribution (SED). These plots will be given in standard units used for Blazars' SED, that are [HZ] (Hertz) for the horizontal axis and [ergcm^{-2}s^{-1}] for the vertical axis. For the classification in their sub-classes (LBL, IBL and HBL), we checked the main catalogues like TEVCAT and TEGEV, but also in the last works published. This is due to the fact that the classification of this kind of sources it is not easy and univocal, because of their high variability.

Therefore according to the classification based on the position of the peak of the synchrotron bump, for our 17 sources, 12 of them have been classified as HBLs, 1 as LBL, 2 as intermediate classes between LBL and IBL and 2 as intermediate between IBL and HBL. The intermediate subclasses are actually due to their enormous variability, that can also reach the scale of the days.
The first test performed was to get the SED of the sources from the reference paper and try to overlap them, searching for common trends. To do this we used the commercial `GraphClick` program, in which I manually sampled the SEDs of our sources; I looked for the best fit that the authors made in every publications of our sources choosing those done with the data that was simultaneous with our MAGIC data found in the corresponding FITS file. If two or more choices were possible, I chose the one that fitted in a better way the data, or that with a two zones-model (SSC2, see section 1.6.4), i.e. the model that fitted the synchrotron peak and the Inverse Compton peak together.
The first plot we obtained had all our 17 sources SEDs overlapped together and can be seen in Figure 3.5.

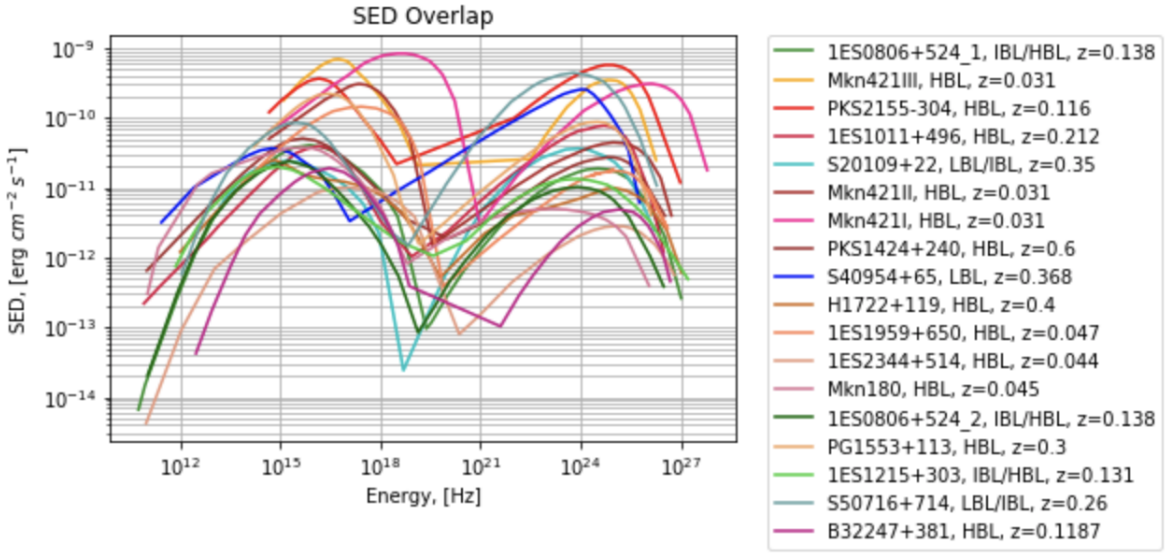

Figure 3.5: Plot showing the SEDs overlap of our 17 sources.

In this plot I have put the colors from the hottest, which means a HBL type source, to the coldest, which means a LBL type source. In this way the different behavior of the classes is presented in a better way. Although the plot is still too much confused because of the 17 sources, the typical trend of these objects starts to be seen: in fact we can see the two peaks, that of the synchrotron and the inverse Compton, and it is clear to see that the greater the energy of the sources, the more the peaks are shifted towards higher energies.

3.2.2 SED study by subclass

To better understand this, we decided to divide the sources into their sub-classes: so in Figure 3.6 the same plot as before but with only the HBLs, in Figure 3.7 the IBLs and in Figure 3.8 the LBLs can be seen.

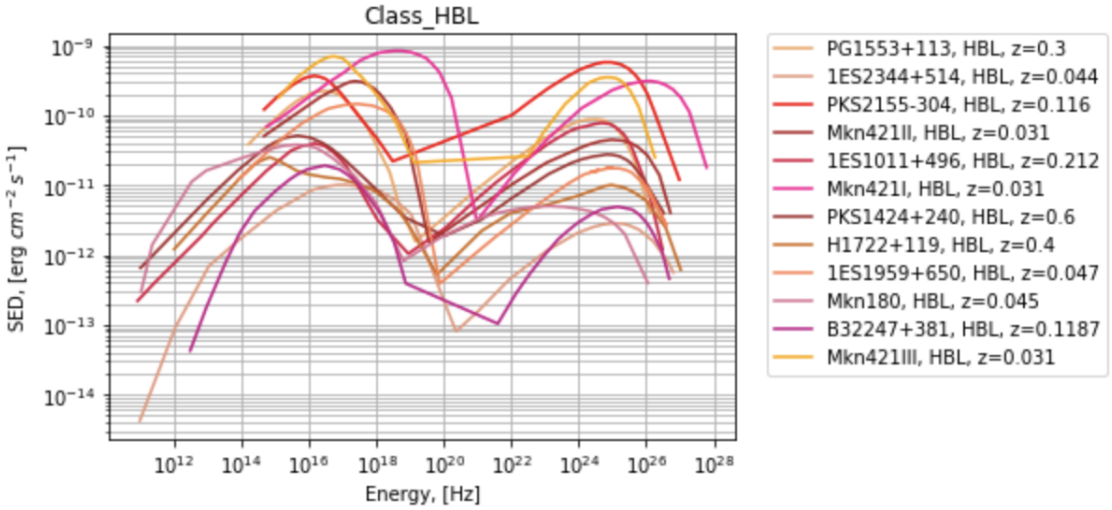

Figure 3.6: Plot showing the SEDs overlap of our 12 HBL sources.

With the help of these new plots, the trend that we wanted to confirm can be seen in a better way. In fact, aside from the exceptions described during the list of the sources in the previous section, we can see that this class of objects follows the double bump synchrotron + inverse Compton SED structure. If we look at Figure 3.7 and Figure 3.8 with more attention, we can see that the two peaks are almost on the same energy range for subclass type; this is because these sources belong to the same subclass, and this confirms the classification we have adopted.
For what concerns the LBL and LBL/IBL type, the synchrotron peak can be found around 10^{15} Hz, while the inverse Compton peak is around 10^{24} Hz. If we look at the IBL/HBL type, we can see that those peaks are shifted towards higher energy, in fact the synchrotron peak can be found around 10^{16} Hz while the inverse Compton one is around 10^{25} Hz. Anyway we always have to remember that these sources are extremely variables, and this

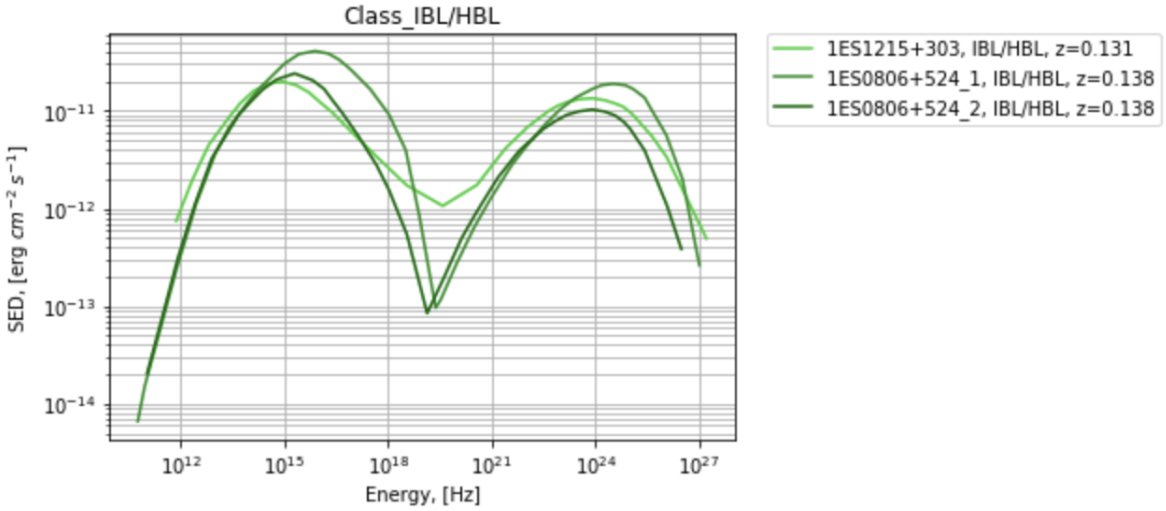

Figure 3.7: Plot showing the SEDs overlap of our 3 IBL/HBL sources.

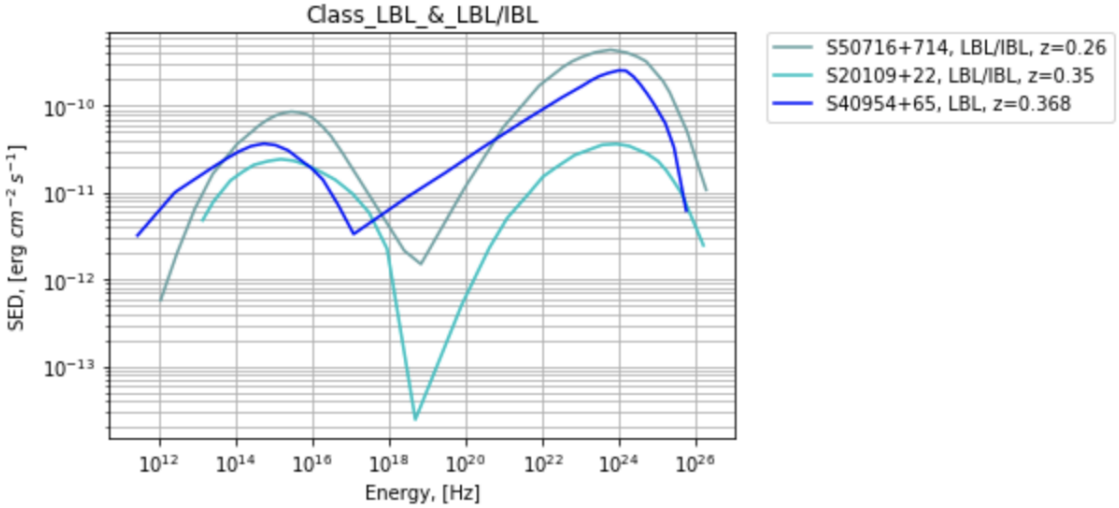

Figure 3.8: Plot showing the SEDs overlap of our 3 LBL and LBL/IBL sources.

affects in a very hard way the evaluation that we are trying to accomplish.
The shifting towards higher energies of the synchrotron and inverse Compton peaks is more accentuated in the case of the HBL type: here we can see a higher shifting, but there is also more confusion. So remembering the characteristics of the sources listed below, we can estimate the synchrotron peak around 10^{16} Hz - 10^{17} Hz, and the inverse Compton one around 10^{25} Hz - 10^{26} Hz.
With these plots is shown in a pretty appropriate way the trend of BL Lacs object, showing that the two peaks shift more to higher energies for more energetic sources. This is a first step into our try to make a population study of these objects.

3.2.3 SED study by redshift

We also wanted to make these plots based on the redshift z of our sources, to see if we could have find some trends depending on the redshift. Our sources had z from 0.031 (Mkn421) to 0.6 (PKS1424+240), so we decided to divide them in three sections:

1. The first section is made by sources with $z < 0.1$: they resulted to be 6, and had $0.031 < z < 0.045$. The resulting overlap plot can be seen in Figure 3.9. We can see that here the peaks are more disorganized than the plots divided per type, but the ranges for the synchrotron peaks are from 10^{17} Hz to 10^{18} Hz and for the inverse Compton peaks are from 10^{25} Hz to 10^{26} Hz. The exception is the Mkn421I (pink line), that seems to have its peaks shifted towards higher energies for one order of magnitude.

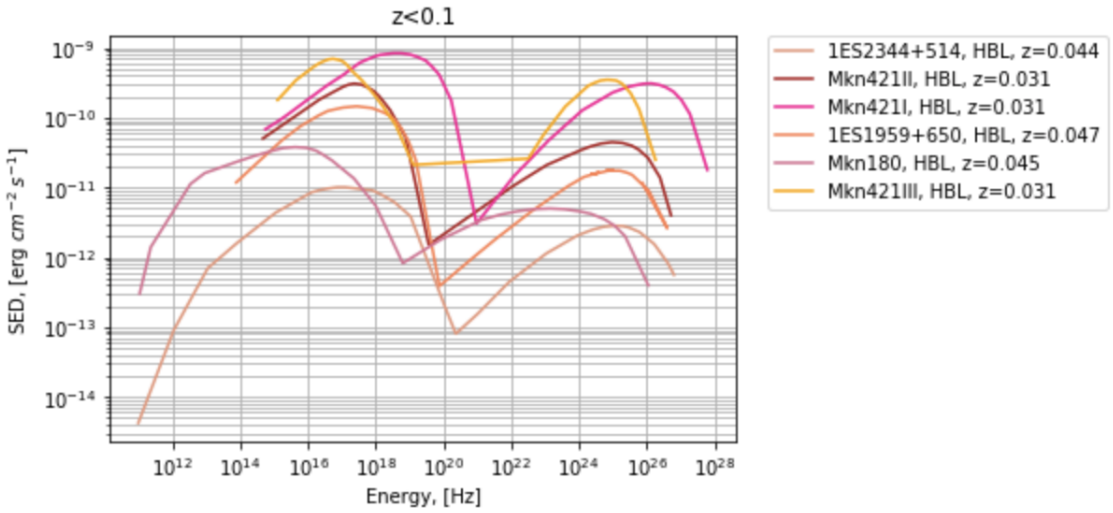

Figure 3.9: Plot showing the SEDs overlap of our 6 sources with z < 0.1.

2. The second section is made by sources with $0.1 < z < 0.25$: they resulted to be 5 , and had $0.116 < z < 0.212$. The resulting overlap plot can be seen in Figure 3.10. We can see that here the peaks are organized in a better way than the ones with lower redshift, and the ranges for the synchrotron peaks are from 10^{16} Hz to 10^{17} Hz, while for the inverse Compton peaks are from 10^{25} Hz to 10^{26} Hz. The red line belongs to the source PKS2155-304, and its greater SED is due to the fact that the data of this source have been taken during an outburst, as said in section 2.3.9.

3. The third section is made by sources with $0.25 < z < 0.6$: they resulted to be 6, and had $0.26 < z < 0.6$. The resulting overlap plot can be seen in Figure 3.11. We can see that also here the peaks are organized in a better way and the ranges for the synchrotron peaks are from 10^{15} Hz to 10^{16} Hz, while for the inverse Compton peaks are from 10^{24} Hz to 10^{25} Hz.

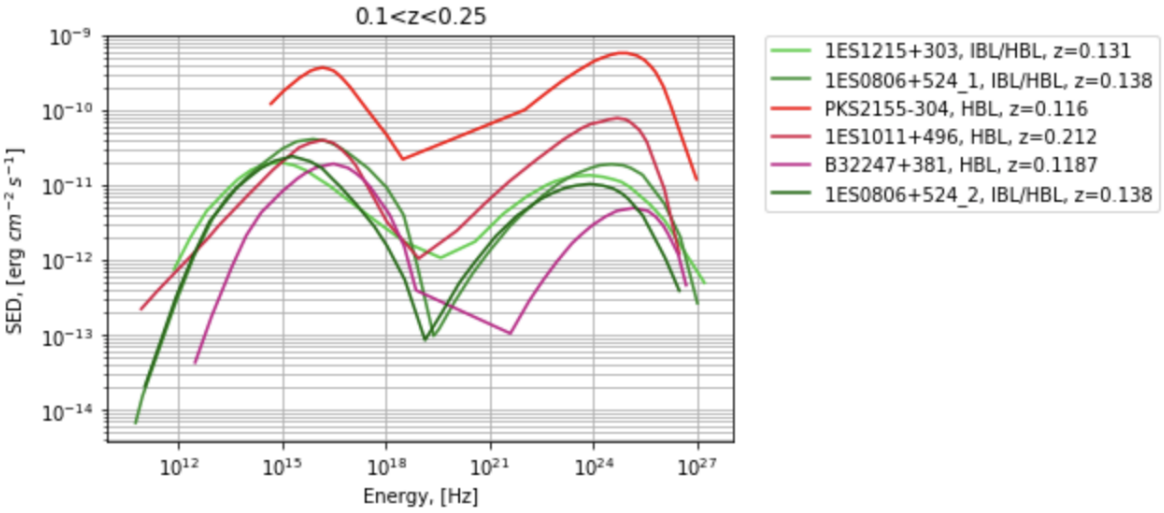

Figure 3.10: Plot showing the SEDs overlap of our 5 sources with 0.1< z <0.25.

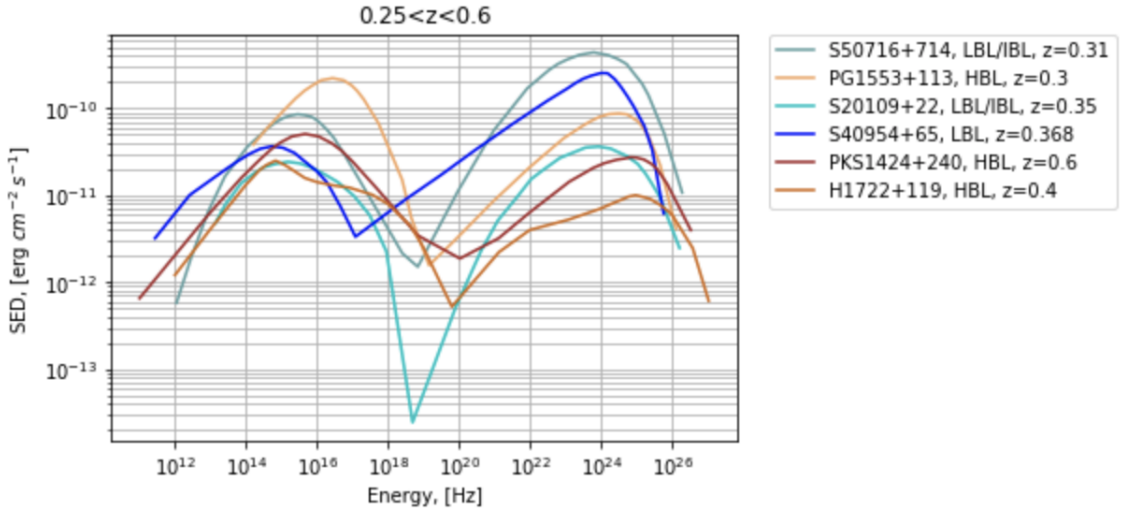

Figure 3.11: Plot showing the SEDs overlap of our 6 sources with 0.25< z <0.6.

In general we can say that a kind of trend can be seen from the results of this analysis, that is the higher the redshift of our sources, the lower the energy of the peaks, as it must be because of the absorption and extinction caused by the redshift.

Chapter 4

SED fitting with JetSet

The last step we wanted to make into our attempt to make a population study of our BL Lacs sources, was to use the JetSet framework developed by Dr. Andrea Tramacere at the University of Geneva, to estimate the peak frequency and flux of the synchrotron and inverse Compton components, from the SEDs of the sources in our sample. To do this we put together the MAGIC data we obtained from the FITS files, and we sampled the SEDs of the sources from their reference paper as explained in section 3.2.1. The method we used is explained in the following sections.

4.1 The JetSet framework

The JetSet framework has been developed by Dr. Andrea Tramacere during the last 15 years, and has been used in several refereed publications. The desktop version will be released soon officially, and a web interface is available at http://isdc.unige.ch/sedtool/PROD/SED.html. The name is an acronym for **J**ets **S**ED modeler and fitting **T**ool [43, 25, 44], and it is basically used to obtain three things:

- accurate numerical modeling of radiative and accelerative process acting in relativistic jets;
- modeling and fitting multiwavelength SEDs;
- handling observed data.

and we mostly used it for its second feature.
The modeling/fitting algorithm is based on the following approach:

1. extraction of the peak frequencies/fluxes, and of the spectral indices in different bands;
2. phenomenological constraining of the physical parameters basing on the parameters extracted at step 1;

3. definition of the starting numerical model basing on the parameters constrained at step 2;

4. determination of the observed data best-fitting model, obtained via the optimization of the numerical model by the minimization of the negative *log-likelihood* or of the *least-squares function*.

An example of a numerical SSC model is shown in Figure 4.1 [45].
Besides phenomenological constraining and fitting, the code can be used to obtain relevant information about the sources under study, as well as plotting results. These functions will be described in the next section.

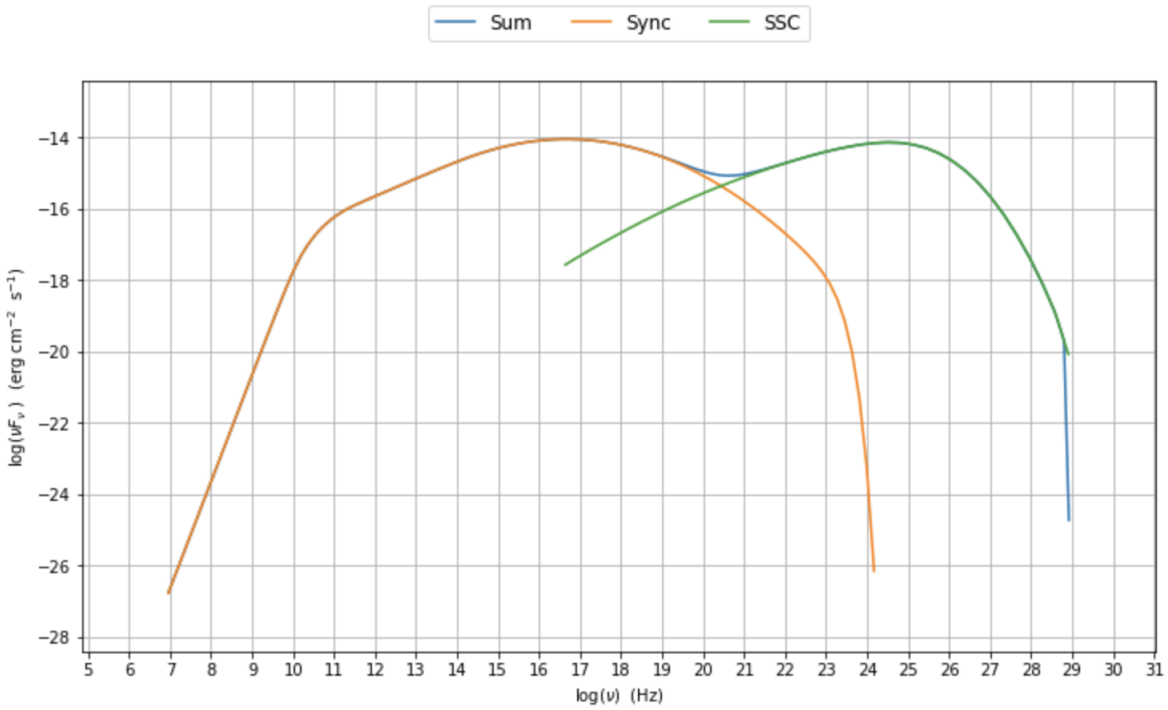

Figure 4.1: An example of a numerical SSC modeling computed by the `JetSet` code, showing the synchrotron component (orange line), the inverse Compton component (green line) and the sum (blue line).

The `JetSet` code is under scrutiny by the Padova group, and several tests were made specially with the purpose of testing and learning the functioning of the code with the ultimate aim of possibly making it one of the official code used by the MAGIC collaboration to characterize SEDs.

4.2 The JetSet data

As first step in our analysis we converted our data in the JetSet specific format; the program needs an ASCII file with the following information:

1. redshift of the source;
2. scale of the dataset, if is linear or logarithm;
3. name of the source;

Data have to be put in columns, following this order:

1. energy;
2. flux;
3. flux error;
4. first date of observation;
5. last date of observation;
6. telescope used to get those data.

In figure 4.2 an example of this input file can be seen.

To get the data of the various telescopes, we used once again the GraphClick program. This time I sampled the full multiwavelength fitting model reported in the SEDs plots, from radio to shorter wavelengths, and not solely the fitting curve. We chose only the simultaneous data with the MAGIC observations, because of the high variability of this kind of sources. The first thing we wanted to obtain was the fit with the data taken from the model of the SEDs of our papers, that we had sampled before, as explained in section 3.2.1.
JetSet is used here to constrain the phenomenological parameters, not to make a fit of a numeric model, and it was set to start testing the synchrotron fit at 10^{11} Hz and to stop it at 10^{19} Hz, while the interval for the inverse Compton fit is set from $10^{21.5}$ Hz to 10^{28} Hz. We have noticed that for some sources the default boundaries of the fitting window given were not compatible with our data, so we decided to change them. For the synchrotron peak we changed the order of magnitudes by -2.5 from the minimum and +3.5 from the maximum, while for the inverse Compton peak we changed the order of magnitudes by -2 from the minimum and +4 from the maximum. In the following figures, Figure 4.3 and Figure 4, we show the difference between the default fit of the program and the one done with the refined ranges of energy.

As we can see from the figures, most of the fits have high goodness both in the default mode and in the refined mode, but there are some exception, for example the source H1722+119 or the source S40954+65 in Figure 4; they are not well fitted by the program

```
# metadata
# md z  0.048000
# md data_scale  lin-lin
# md restframe  obs
# md col_types x,y,dy,T_start,T_stop,data_set
# md obj_name 1ES1959+650
#
# Frequency [Hz]  EnergyFlux [erg/cm2/s]   EnergyFlux [erg/cm2/s] T [MJD]  T [MJD]
# Xval            Yval                     YvalError              T_start  T_stop  data_set-flag
#
#MAGIC START
4.668533e+25 1.398932e-11 5.482709e-12 5.387620e+04 5.388210e+04 MAGIC
7.729369e+25 6.126671e-12 2.058153e-12 5.387620e+04 5.388210e+04 MAGIC
1.279701e+26 6.425835e-12 1.260795e-12 5.387620e+04 5.388210e+04 MAGIC
2.118715e+26 4.784331e-12 1.202989e-12 5.387620e+04 5.388210e+04 MAGIC
3.507825e+26 3.859983e-12 1.029039e-12 5.387620e+04 5.388210e+04 MAGIC
5.807648e+26 2.191105e-12 1.020959e-12 5.387620e+04 5.388210e+04 MAGIC
#MAGIC STOP
4.293e14        2.814e-11       0.00000e+0      5.38762e+04     5.38821e+04     Optical-UV
5.545e14        2.686e-11       2.8400e-12      5.38762e+04     5.38821e+04     SWIFT
6.856e14        2.919e-11       2.9540e-12      5.38762e+04     5.38821e+04     SWIFT
8.437e14        3.688e-11       3.4020e-12      5.38762e+04     5.38821e+04     SWIFT
1.130e15        4.131e-11       3.6210e-12      5.38762e+04     5.38821e+04     SWIFT
1.322e15        5.368e-11       5.1540e-12      5.38762e+04     5.38821e+04     SWIFT
1.410e15        4.614e-11       2.9190e-12      5.38762e+04     5.38821e+04     SWIFT
1.094e17        1.398e-10       0.00000e+0      5.38762e+04     5.38821e+04     UVOT/SWIFT
2.359e17        1.605e-10       0.00000e+0      5.38762e+04     5.38821e+04     UVOT/SWIFT
3.575e17        1.580e-10       0.00000e+0      5.38762e+04     5.38821e+04     UVOT/SWIFT
4.612e17        1.618e-10       0.00000e+0      5.38762e+04     5.38821e+04     UVOT/SWIFT
5.669e17        1.590e-10       0.00000e+0      5.38762e+04     5.38821e+04     UVOT/SWIFT
7.408e17        1.488e-10       0.00000e+0      5.38762e+04     5.38821e+04     UVOT/SWIFT
9.750e17        1.454e-10       0.00000e+0      5.38762e+04     5.38821e+04     UVOT/SWIFT
1.704e18        1.276e-10       0.00000e+0      5.38762e+04     5.38821e+04     UVOT/SWIFT
3.037e18        9.138e-11       0.00000e+0      5.38762e+04     5.38821e+04     Suzaku
3.735e18        8.624e-11       0.00000e+0      5.38762e+04     5.38821e+04     Suzaku
3.830e18        8.439e-11       0.00000e+0      5.38762e+04     5.38821e+04     Suzaku
4.389e18        7.950e-11       0.00000e+0      5.38762e+04     5.38821e+04     Suzaku
5.082e18        7.644e-11       0.00000e+0      5.38762e+04     5.38821e+04     Suzaku
5.206e18        6.990e-11       0.00000e+0      5.38762e+04     5.38821e+04     Suzaku
6.294e18        6.340e-11       0.00000e+0      5.38762e+04     5.38821e+04     Suzaku
7.137e18        5.518e-11       0.00000e+0      5.38762e+04     5.38821e+04     Suzaku
8.381e18        4.101e-11       0.00000e+0      5.38762e+04     5.38821e+04     Suzaku
1.048e19        4.002e-11       0.00000e+0      5.38762e+04     5.38821e+04     Suzaku
```

Figure 4.2: An example of the `JetSet` input file for the source 1ES1959+650 is shown.

in default mode: this is clearly because of the presence of the host galaxy we mentioned before in section 2.3.13 for the first source, and because of the external Compton process as mentioned before in section 2.3.15. After having refined the range of energy we can see that the fit has become better than before.

With this program we could also check if our estimate of the spectral index of the MAGIC spectra of our sources explained in section 3.2 was accurate. To do this, we used a linear fit on the MAGIC data as done by `JetSet`. The program fitted our data with a linear fit, a straight line, with a log-log scale and calculated its coefficient, that is the spectral index we looked for. We show the distribution of spectral indices in Figure 5. This distribution match that computed previously, showing stability of the code.

4.2.1 Diagnostic based on the phenomenological parameters

We start our analysis, investigating the position of the synchrotron and of the inverse Compton peak frequencies. This position is calculated starting from the two fits that the program makes. With these data we checked the distribution to verify the important physical fact that the energy dispersion of the synchrotron peak should be higher than in the inverse Compton one. This fact is linked to the energy of the particles and to their diffusion, and it occurs because the energy of the diffused electron is different from the one of the photon that scatters it. So the lower dispersion of the inverse Compton peaks is due to the fact that, for most of the sources in our sample, the inverse Compton scattering above the peak of the inverse Compton component is not happening in Thomson regime but mostly in that of Klein-Nishina. Indeed, as long as we are in the Thomson regime we expect that the up-scattered frequency (ν^{IC}) is related to the seed synchrotron one (ν^{S}) and to the Lorentz factor of the electron (γ), by the relation $\nu^{IC} \simeq \frac{4}{3}\nu^{S}\gamma^{2}$. In this case one woulds expect to see the same dispersion both in the peak frequency of the synchrotron and inverse Compton emissions. On the contrary, as long as both γ and ν^{S} are increasing, the scattering moves towards the Klein-Nishina regime, and the ν^{IC} starts to grow slower with respect to γ and ν^{S}. This prediction is in agreement with our results, as can be seen in fig 6. On the left the results for the default data are reported, while on the right the results for the refined data are reported.

As we can see, the dispersion of the synchrotron peak is about 3.5 orders of magnitude, while for the inverse Compton we had a dispersion of 2 orders of magnitude for the default data, and almost the same results can be seen in the the refined data. This verifies the physics explained above and enhance our estimates.

Furthermore, we show on in Figure 7 the logarithm of the frequency of the synchrotron peak $\log(\nu_{\rm p}^{\rm S})$ versus the logarithm of the ratio between the frequency of the inverse Compton peak and the one of the synchrotron peak $\log(\nu_{\rm p}^{\rm IC}/\nu_{\rm p}^{\rm S})$: this plot resulted to have a linear descending trend, and it shows the clear information that the more the logarithm of the synchrotron peak $\log(\nu_{\rm p}^{\rm S})$ is higher, the more the logarithm of the ratio between the frequency of the inverse Compton peak and the one of the synchrotron peak $\log(\nu_{\rm p}^{\rm IC}/\nu_{\rm p}^{\rm S})$

decreases.

In the default data plot we can clearly see the presence of the outlier source S40954+65. This is due, as explained in section 2.3.15, to the external Compton instead of an inverse Compton emission that is responsible for the high energy peak. This essentially intensifies the difference between the low energy and high energy peaks, and making it an outlier in our plot.
In the refined data plot, we can instead see two ouliers: the first one is the same source like in the default one, while the second source is H1722+119; here in this source, as explained in section 2.3.13, we have a host galaxy that interferes with our results and although also in the paper this has been taken in consideration the data results anyway affected.

The last parameter we wanted to study was the *Compton Dominance*. It is defined as:

$$\text{Compton Dominance} = \nu\text{F}(\nu_{\text{p}}^{\text{IC}})/\nu\text{F}(\nu_{\text{p}}^{\text{S}}), \tag{4.1}$$

and it is the ratio of the peak of the Compton to the synchrotron peak luminosities or frequencies ($\nu F(\nu)$), and it is strongly related to the inverse Compton regime, it is expected to be higher in the Thomson regime, and lower in that of Klein-Nishina. After having computed the Compton dominance, we decided to plot it versus the logarithm of the ratio between the energy of the synchrotron peak and the energy of the inverse Compton peak. The results for the default and the refined data are shown in Figure 8. Here the trend is linear and ascending, and it is justified by the physical fact that when the regime switch from the Thomson to the Klein-Nishina one, the cross section decreases and so the energy emitted is lower than in a Thomson regime.

Also here in these plots we can see two outliers: the first is the same sources as before, S40954+65, and we already know why it is an outlier. The second one is the source S50716+714 and essentially it has the same emission as the other one: it probably emits with an external Compton process, and it is here explained why it is an outlier, because of the enormous energy of the high energy peak.

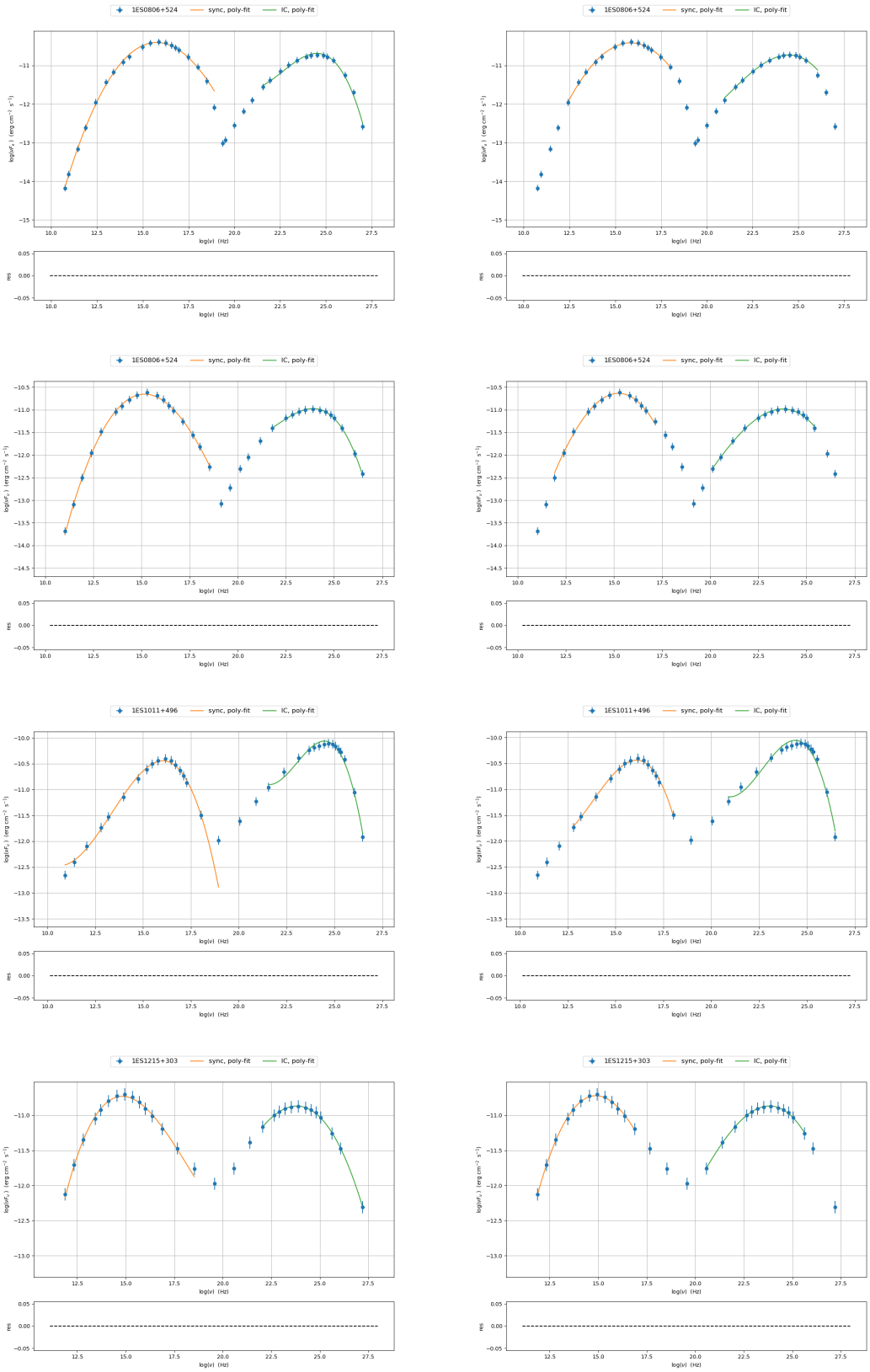

Figure 4.3: Fits made with the `JetSet` program with the SEDs samples taken from the papers for the source 1ES0806+524, 1ES1011+496 and 1ES1215+303. On the left there is the default fit, while on the right there is the refined fit.

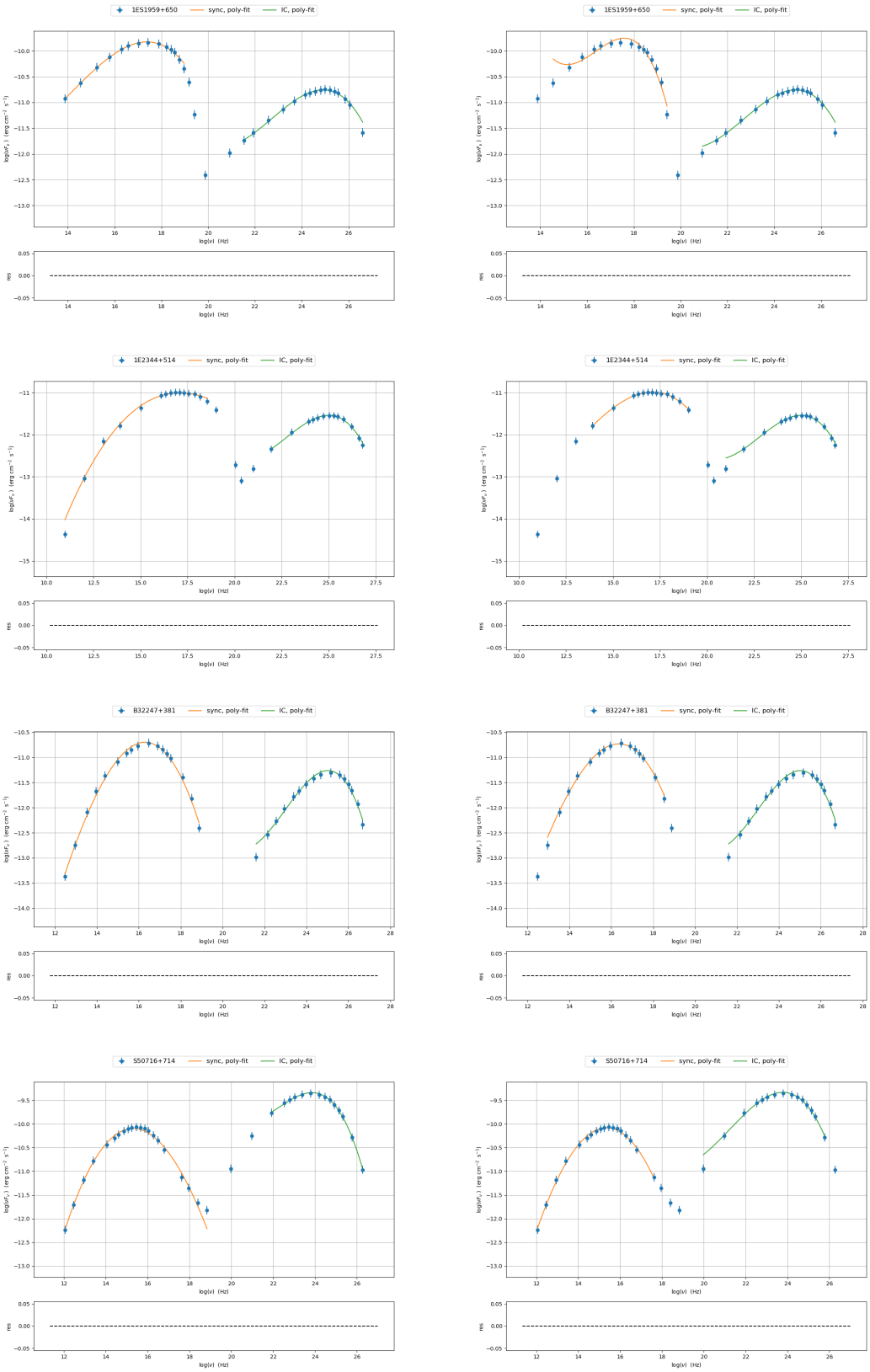

Figure (Cont.): Same as previous figure for 1ES1959+650, 1ES2344+514, B32247+381 and S50716+714

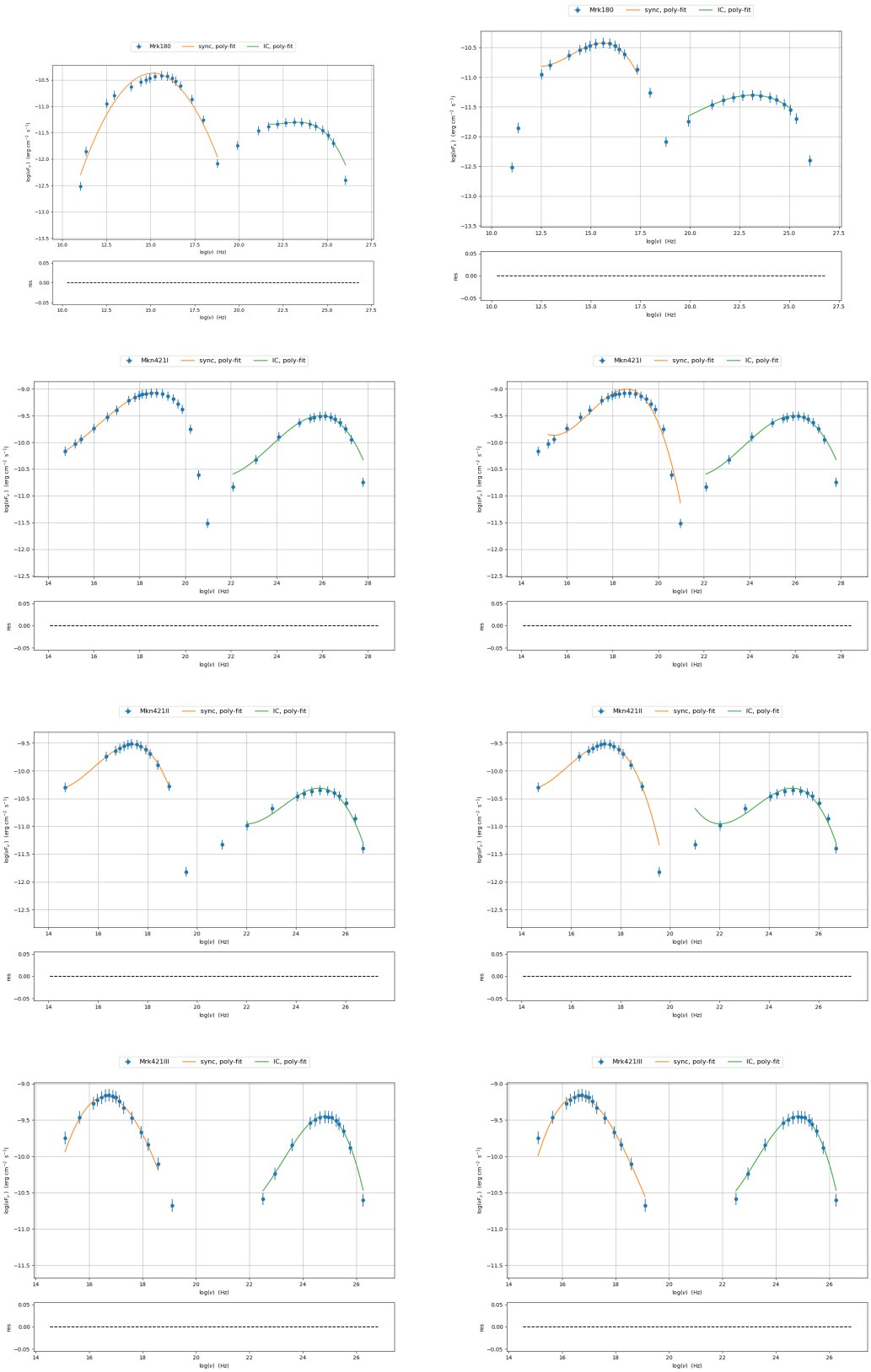

Figure (Cont.): Same as before for the sources Mkn180 and Mkn421

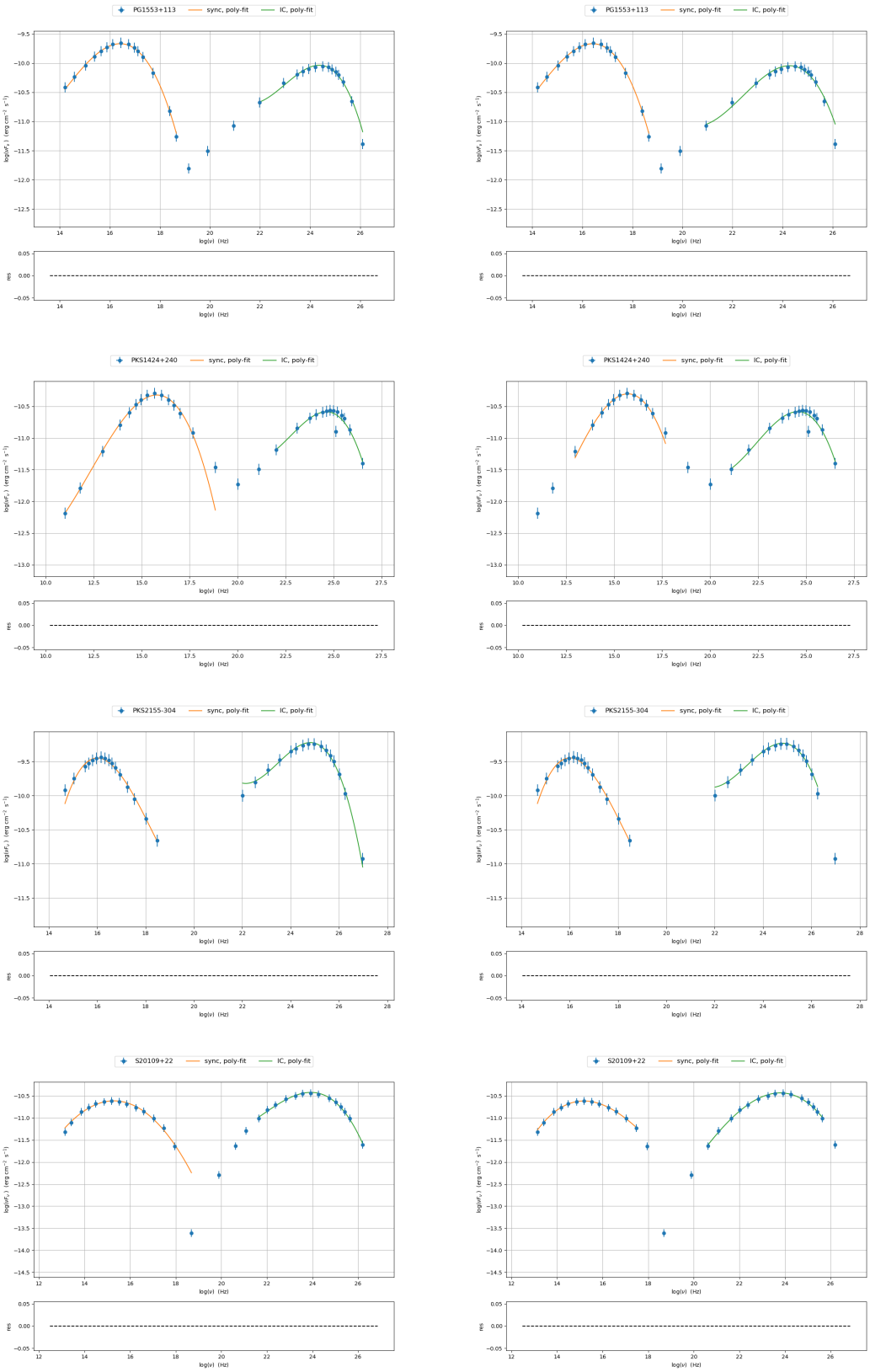

Figure (Cont.): Same as before for the sources PG1553+113, PKS1424+240, PKS2155-304 and S20109+22

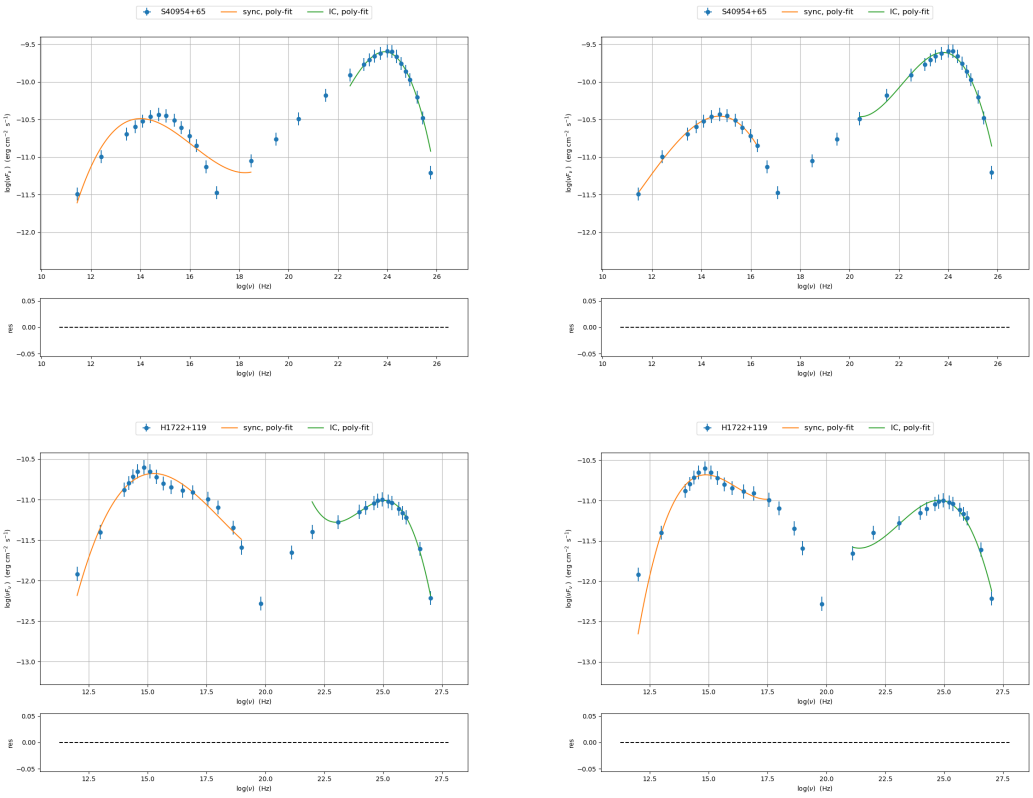

Figure 4: Same as before for S40954+65 and H1722+119

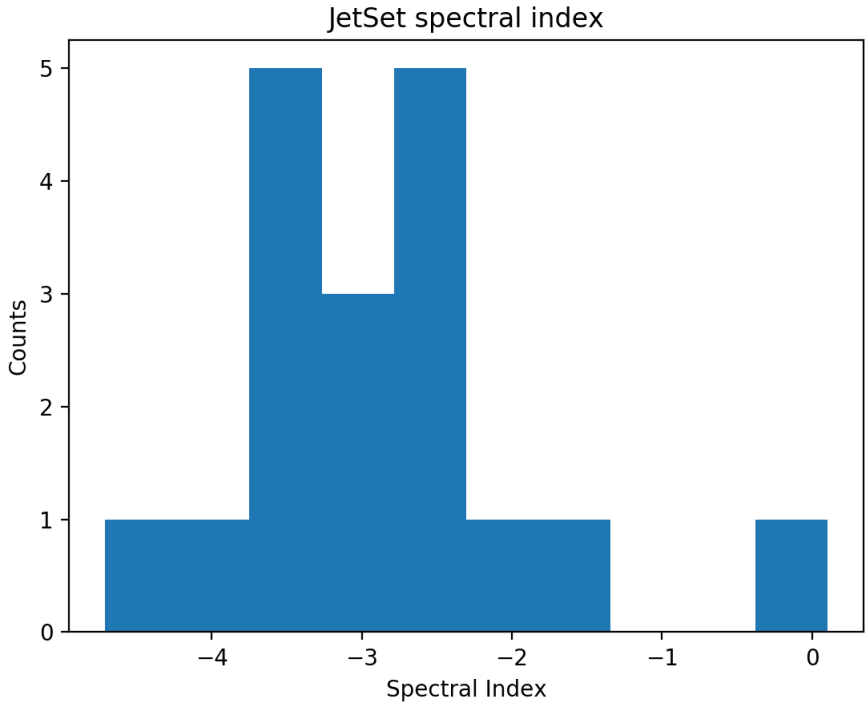

Figure 5: Histogram representing the spectral indices of the sources computed by the program `JetSet`.

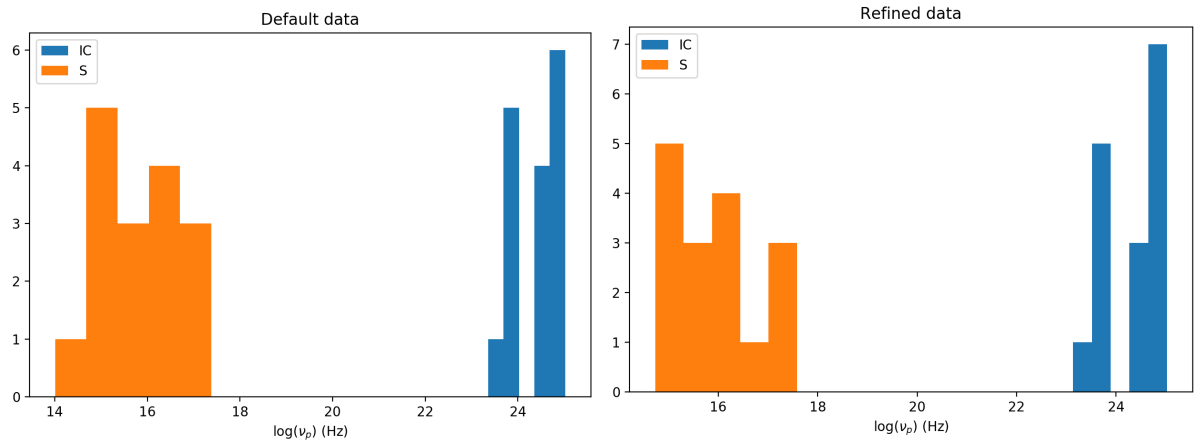

Figure 6: Histograms reporting the energy dispersion of the peaks of synchrotron and inverse Compton. Data obtained for default mode are on the left, for refined mode are on the right.

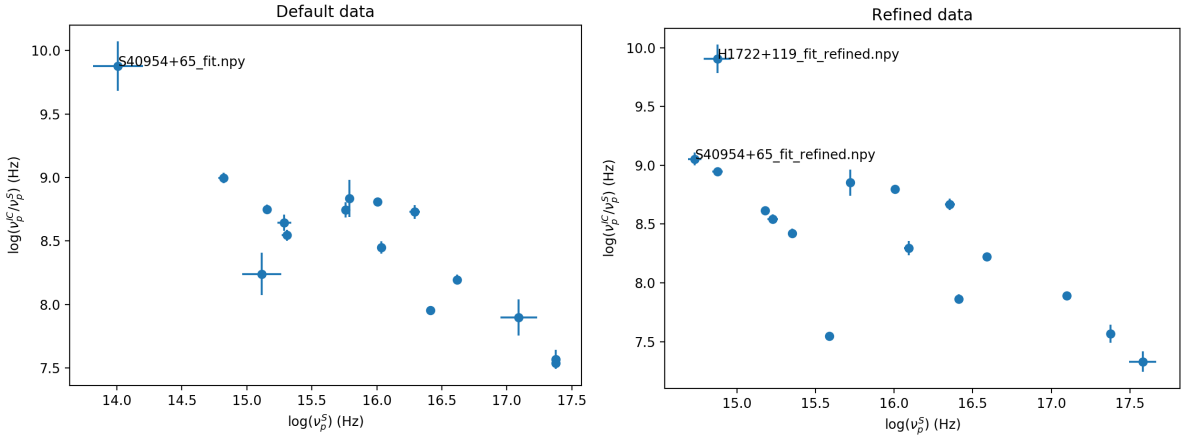

Figure 7: Plot showing $\log(\nu_{\rm p}^{\rm S})$ versus $\log(\nu_{\rm p}^{\rm IC}/\nu_{\rm p}^{\rm S})$. It results in a linear descending trend. On the left the default data are represented, while on the right there are the refined ones. Two outliers are clearly visible, due to the peculiar characteristics of these two sources as explained in the previous sections.

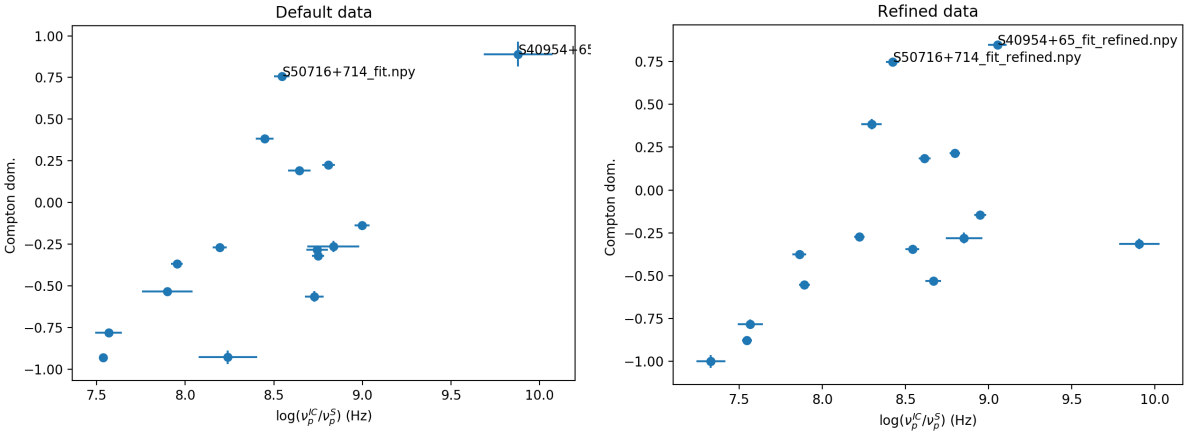

Figure 8: Plot showing $\log(\nu_{\rm p}^{\rm IC}/\nu_{\rm p}^{\rm S})$ versus the Compton dominance. It results in a linear ascending trend. On the left the default data are represented, while on the right there are the refined ones. Two outliers are clearly visible, due to the peculiar characteristics of these two sources.

Chapter 5

Conclusions and outlooks

5.1 Conclusions

This master thesis is a resume of my work in the field of extragalactic VHE γ-ray astronomy, carried out from May to December 2018, as a member of the MAGIC collaboration in the Padova group. This master thesis also gave me the opportunity to work a week at the University of Geneva, hosted by the department of Astronomy and by Dr. Tramacere. This work has been mainly divided in two parts, the first being necessary to deal with the second. In the first part I started by reviewing the source catalog files that the MAGIC collaboration has made accessible in a publicly available online site, all published in FITS format. During this analysis I wrote a script that allows to obtain the general information about the files, the lightcurves, the spectra and the spectral indices of the files. Here I did the check of the data contained in the FITS files and I reported my analysis and the mistakes I found in a document to improve the data that the MAGIC collaboration makes available, studying the type of sources that the MAGIC telescopes studied, and their statistics. What results from my analysis is that the most of the γ-ray sources studied have an extragalactic origin, and they are mainly BL Lacertae objects, in particular of the type HBL i.e. high energy peaked BL Lacertae. I hope that this analysis I made could help the MAGIC collaboration with the production of a proper catalog, which is under discussion within the whole collaboration, of FITS files in a standard astronomic format, where the analysis and the data will be more homogeneous than now.

In the second part of my master thesis, the BL Lacertae objects studied by MAGIC have been analyzed under several aspects and this work has been divided in two step: the first one has been made here in Padova and I have used the data taken from the MAGIC FITS files to obtain and compare the spectra of the BL Lac sources, that resulted to be 17. During my analysis I have overlapped together the spectra and looked for similar trends, getting the spectral indices that resulted to agree with the steep spectra. After having obtained the Spectral Energy Distribution of these sources, I have analyzed them and I have studied the position of the synchrotron and the inverse Compton peak according to

the BL Lac subclass and redshift. The trends I verified are that the two peaks shift more to higher energies for more energetic sources, and that the higher the redshift of our sources, the lower the energy of the peaks, as it must be from the physics described in the first chapter of this work.
The second step has been going for a week at the University of Geneva, and using the `JetSet` program to try to obtain some fits of the synchrotron and inverse Compton peak for the BL Lac sources. There I have learned the basis of the program and with the help of Dr. Tramacere we obtained our fits. With the data collected with the program I have been able to produce some plots to verify the physics of this class of objects, like the greater dispersion of the synchrotron peak energies with respect to the inverse Compton one, and the trend of the Compton Dominance. All the obtained results agree with the theory of the BL Lacertae sources and verify the work. The various outliers found during the analysis have been clarified within the margins of error, by a specific characteristic of the sources taken in consideration, like the presence of a host galaxy or the presence of an external Compton emission instead of that of inverse Compton.

5.2 Outlooks

For what concerns the first part of my work, the production of a homogeneous and standardized catalog in the FITS astronomical format has to keep going on, because there is the need to have a standard format that could be the same for all the scientific data. For the MAGIC collaboration this is an important step to conclude, and in the next years this aim will be finally reached.

Instead, regarding the second part, the script I wrote could be used by the MAGIC collaboration to have a free and fast access to the FITS files, to obtain the data contained and to make all the plots needed for several analysis that can be made, in order to characterize deeply the MAGIC studied sources. These data could also be united with those of other telescopes, like Fermi, HESS, VERITAS, etc, to have a more complete characterization. In addition, the `JetSet` code is under scrutiny by the Padova group, and the aim is to possibly making it one of the official code used by the MAGIC collaboration to characterize SEDs.

Appendix A

Script

```
# Preliminary imports
import matplotlib.pyplot as plt
from astropy.visualization import astropy_mpl_style
plt.style.use('default')
from astropy.io import fits
from astropy.utils.data import download_file
from astropy.io import ascii
import pylab
%matplotlib inline
import numpy as np

# How to get informations about the file
#insert url of the file
image = 'http://vobs.magic.pic.es/fits/mfits/base/MAGIC_2009_S50716.fits'
imagefile = download_file(image)
hdulist = fits.open(imagefile)
hdulist.info()
hdu = hdulist['PRIMARY']
hdu.header

# How to plot the LightCurve
srcname = hdu.header['OBJECT']
hdulist = fits.open(image, memmap=True)
hdu = hdulist['LIGHTCURVE']
print(hdu.header)
label1 = hdu.header['TTYPE1']
label2 = hdu.header['TTYPE2']
#label3 = hdu.header['TTYPE3']
#label4 = hdu.header['TTYPE4']
# uncomment label3 and/or label4 if there are experimental uncertainties
```

```
unit1 = ','+ hdu.header['TUNIT1']
unit2 = ','+ hdu.header['TUNIT2']
tot1 = (label1) + (unit1)
#tot1 and tot2 will be the x and y label of the plot
tot2 = (label2) + (unit2)
label1 = data.field(0)
label2 = data.field(1)
#label3 = data.field(2)
#label4 = data.field(3)
print(label1)
print(label2)
#print(label3)
#print(label4)

# CONVERSION MJD - AMERICAN DATE
from astropy.time import Time
import numpy as np
from datetime import date
t = Time(label1, format='mjd', out_subfmt='date')
date = t.iso
datelist = np.array(date).tolist()
print(datelist)
data = []
data.append(0)
for i in range(0, len(label1)-1):
    r = data[i]+label1[i+1]-label1[i]
    data.append(r)
print(data)

# CONVERSION TEV-ERG
b = (label2)
erg = b*1.60218
#errors in erg
c = (label3)
errerg = c*1.60218
print(erg)
print(errerg)

# FINAL PLOT
fig = plt.figure()
ax1 = fig.add_subplot(111)
ax1.plot(label1, label2)
ax1.set_xticks(data, datelist)
```

```
ax1.autoscale(enable=True, axis='both', tight=None)
ax1.set_xlabel('MJD')
ax1.set_ylabel('Flux, ph TeV cm$^{-2}$ s$^{-1}$')
ax1.grid(True,which='both',axis='both', ls='-')
ax1.errorbar(label1, label2, xerr=None, yerr=label3, fmt='.')
#be careful with xerr and yerr: it depends on and if there are errors
#hdu = hdulist['PRIMARY']
#ax1.set_title(srcname + ',' + hdu.header['REFPAPER'])
#uncomment if you want the title with source and paper

ax2 = ax1.twiny()
ax2.plot(data, label2)
ax2.set_xticks(data)
ax2.set_xticklabels(datelist, rotation='45')
ax2.autoscale(enable=True, axis='both', tight=None)
ax2.set_xlabel('Date')
ax2.set_ylabel('Flux, ph erg cm$^{-2}$ s$^{-1}$', color='black')
ax2.errorbar(data, label2, xerr=None, yerr=label3, fmt='.')

ax3 = ax2.twinx()
ax3.plot(data, erg)
ax3.set_xticks(data, datelist)
ax3.autoscale(enable=True, axis='both', tight=None)
ax3.set_xlabel('Date', color='black')
ax3.set_ylabel('Flux, ph erg cm$^{-2}$ s$^{-1}$')
ax3.errorbar(data, erg, xerr=None, yerr=errerg, fmt='.')

# How to plot the Spectrum
hdu = hdulist['PRIMARY']
hdu.header
srcname = hdu.header['OBJECT']
hdulist = fits.open(image, memmap=True)
hdu = hdulist['SPECTRUM']
hdu.header
label1 = hdu.header['TTYPE1']
label2 = hdu.header['TTYPE2']
#label3 = hdu.header['TTYPE3']
#label4 = hdu.header['TTYPE4']
# uncomment label3 and/or label4 if there are experimental uncertainties
unit1 = ','+ hdu.header['TUNIT1']
unit2 = ','+ hdu.header['TUNIT2']
tot1 = (label1) + (unit1)
tot2 = (label2) + (unit2)
```

```
label1 = data.field(0)
label2 = data.field(1)
#label3 = data.field(2)
#label4 = data.field(3)
print(label1)
print(label2)
#print(label3)
#print(label4)

# CONVERSION TEV-ERG
b = (label2)
erg = b*1.60218
#errors in erg
c = (label3)
errerg = c*1.60218
print(erg)
print(errerg)

# FINAL PLOT
fig = plt.figure()
ax1 = fig.add_subplot(111)
ax1.loglog(label1, label2)
ax1.autoscale(enable=True, axis='both', tight=None)
ax1.set_xlabel('Energy, GeV')
ax1.set_ylabel('Flux, ph TeV cm$^{-2}$ s$^{-1}$')
ax1.grid(True,which="both",axis="both", ls='-')
ax1.errorbar(label1, label2, xerr=None, yerr=label3, fmt='.')
#hdu = hdulist['PRIMARY']
#ax1.set_title(srcname + ';   ' + hdu.header['REFPAPER'])

ax2 = ax1.twinx()
ax2.loglog(label1, erg)
ax2.autoscale(enable=True, axis='both', tight=None)
ax2.set_ylabel('Flux, ph erg cm$^{-2}$ s$^{-1}$', color='black')
ax2.errorbar(label1, erg, xerr=None, yerr=errerg, fmt='.')
```

Bibliography

[1] http://astroparticle.uchicago.edu

[2] Wagner, R. PhD Thesis. Phd thesis, Technische Universitat Munchen, 2006

[3] Longair, M.S. High Energy Astrophysics. Cambridge University Press, Cambridge, 2011

[4] De Angelis, A. & Pimenta, M.J.M.P. Introduction to Particle and Astroparticle Physics. Springer-Verlag Mailand, New York, NY, 2015

[5] Blumenthal, G.R. Gould, R.J. Bremsstrahlung, Synchrotron Radiation, and Compton Scattering of High-Energy Electrons Traversing Dilute Gases. Reviews of Modern Physics, 1970

[6] Heitler, W. The Quantum Theory of Radiation. The International series of monographs on physics. Clarendon Press, 1960

[7] Padmanabhan, T. Theoretical Astrophysics - Volume 3, Galaxies and Cosmology. Cambridge University Press, Cambridge, UK, 2002

[8] Franceschini, A., Rodighiero, G. Vaccari, M. Extragalactic optical-infrared background radiation, its time evolution and the cosmic photon-photon opacity. Astronomy and Astrophysics, 2008

[9] Robson, I. Active galactic nuclei. Wiley-Praxis Series in Astronomy and Astrophysics, Chichester, UK, 1996

[10] Peterson, B.M. An Introduction to Active Galactic Nuclei. Cambridge University Press, Cambridge, UK, 1997

[11] Beckmann, V. and Shrader, C.R. Active Galactic Nuclei. 2012

[12] Bastieri, D. et al., The mirrors for the MAGIC telescopes, international cosmic ray conference, 2005

[13] Borla Tridon, D. et al., Performance of the camera of the MAGICII telescope, 2009

[14] Hillas, A.M.,The origin of the Ultra-high-energy cosmic rays, 1984

[15] G., Rybicky A.,P., Lightman, Radiative Process in Astrophysics, John Wiley Sons, 1979

[16] F., C., Jones, Phys Rev., 1968

[17] ABdo et al., ApJ 736, 2011

[18] Cortina, J., Goebel, F., Schweizer, T. and MAGIC collaboration, technical performance of the MAGIC telescopes, 2009

[19] Cortina, J., et al., technical performance of the MAGIC telescope, international cosmic rays conference, 2005

[20] Aleksic, J., Rico, J., FITS format for MAGIC data, 2009

[21] Hanisch, R. J. et al., 2001

[22] Nigro, C., et al., Towards open and reproducible multi-instrument analysis in gamma-ray astronomy, 2018

[23] Vercellone, S., et al., The Duty-cycle of Gamma-ray Blazars: a New Approach, New Results, 2005

[24] Ghisellini, G., Jetted active galactic nuclei. Int. J. Mod. Phys., in press, arX- iv:1109.0015., 2011

[25] Tramacere, A., et al., Swift observations of the very intense flaring activity of Mrk 421 during 2006. I. Phenomenological picture of electron acceleration and predictions for MeV/GeV emission, 2009

[26] Aleksic, J., et al., MAGIC TeV Gamma-Ray Observations of Markarian 421 during Multi-wavelength Campaigns in 2006, 2010

[27] Albert, J., et al., Observations of Mkn 421 with the MAGIC Telescope, 2007

[28] Acciari, V., A., et al., Simultaneous Multiwavelength Observations of Markarian 421 During Outburst, 2009

[29] Albert, J., et al., Discovery of Very High Energy Gamma-rays from Markarian 180 triggered by an optical outburst, 2006

[30] Albert, J., et al., Discovery of Very high energy gamma-rays from 1ES1011+496 at z=0.212, 2007

[31] Tagliaferri, G., et al., Simultaneous multiwavelength observations of the blazar 1ES1959+650 at a low TeV flux, 2008

[32] Anderhub, H., et al., Discovery of Very High Energy gamma-rays from the blazar S5 0716+714, 2009

[33] Aleksic, J., et al., Simultaneous multi-frequency observation of the unknown redshift blazar PG 1553+113 in March-April 2008, 2010

[34] Aleksic, J., et al., Discovery of VHE -rays from the blazar 1ES 1215+303 with the MAGIC Telescopes and simultaneous multiwavelength observations, 2012

[35] Aleksic, J., et al., Discovery of VHE gamma-ray emission from the BL Lac object B3 2247+381 with the MAGIC telescopes, 2012

[36] Aleksic, J., et al., High zenith angle observations of PKS 2155-304 with the MAGIC-I Telescope, 2012

[37] Aleksic, J., et al., The simultaneous low state spectral energy distribution of 1ES 2344+514 from radio to very high energies, 2013

[38] Aleksic, J., et al., MAGIC long-term study of the distant TeV blazar PKS 1424+240 in a multiwavelength context, 2014

[39] Aleksic, J., et al., MAGIC detection of short-term variability of the high-peaked BL Lac object 1ES 0806+524, 2015

[40] Ahnen, M., L., et al., Investigating the peculiar emission from the new VHE gamma-ray source H1722+119, 2016

[41] Ansoldi, S., et al., The broad-band properties of the intermediate synchrotron peaked BL Lac S2 0109+22 from radio to VHE gamma rays, 2018

[42] Ahnen, M., L., et al., The detection of the blazar S4 0954+65 at very-high-energy with the MAGIC telescopes during an exceptionally high optical state, 2018

[43] Tramacere, A., et al., Stochastic Acceleration and the Evolution of Spectral Distributions in Synchro-Self-Compton Sources: A Self-consistent Modeling of Blazars' Flares, 2011

[44] Massaro, E., et al., Log-parabolic spectra and particle acceleration in blazars. III. SSC emission in the TeV band from Mkn501, 2006

[45] Tramacere, A., jet model user guide

[46] Prandini, E., et al., Constraining blazar distances with combined Fermi and TeV data: an empirical approach, 2010